Thesis for Ph.D. in
Theory and Numerical Simulations of the Condensed Matter

Channel Mixing and Spin Transport in the Integer Quantum Hall Effect

Candidate: Davide Venturelli

Thesis supervised by
Denis Feinberg, Rosario Fazio, Vittorio Giovannetti, Fabio Taddei

Contents

Summary / Résumé

Edge states are 1-dimensional transport channels, emerging in quantum wells in the integer Quantum Hall regime, with remarkable properties of chirality and quantum coherence. In this thesis we present the idea of manipulating electronic currents mixed over two co-propagating edge channels, and discuss its potential impact for quantum interferometry and transport of spin-qubit states.

We introduce the characteristics of edge states and evaluate the effect of local, non adiabatic potentials and their efficiency to transfer charge between two channels. We show that sharp potential variations whose energies are smaller than the Landau gap provide weak mixing, and we identify some experimental strategies that can achieve good mixing percentages.

We develop numerical techniques of simulation to model existing experiments that employ mixed edge channels, and analytical methods in order to treat the effect of Coulomb interactions between edge states in a future spin-interferometry experiment.

Les états de bord sont des canaux de transport unidimensionnels qui se développent dans des puits quantiques en régime d'Effet Hall entier, avec de remarquables propriétés de chiralité et de cohérence quantique. Dans cette thèse nous présentons l'idée d'une manipulation de courants électroniques mettant en jeu le mélange de deux canaux de bord co-propageants, et nous discutons son impact potentiel pour l'interférométrie quantique et le transport de qubits de spin.

Nous présentons les caractéristiques des états de bord et évaluons l'effet de potentiels locaux et non-adiabatiques, et de leur efficacité pour transférer la charge entre les deux canaux. Il est montré que des variations rapides du potentiel, d'amplitude plus petite que le gap de Landau, donnent lieu à un faible mélange, et nous identifions des stratégies expérimentales permettant d'atteindre un bon pourcentage de mélange.

Nous développons des techniques de simulation numérique afin de modéliser de expériences qui mettent en jeu des canaux avec mélange, ainsi que des méthodes analytiques permettant de traiter les interactions coulombiennes entre états de bord, en vue de futures expériences d'interférométrie de spin.

1 Edge States in the Integer Quantum Hall Effect

This chapter provides a general introduction to the physical system which is the main object of discussion of the following chapters: the edge states in 2-dimensional electron gases in the integer Quantum Hall regime. We will also briefly present the transport properties of these states by means of the Landauer-Buttiker scattering formalism which will be used as an underlying paradigm of reference for calculation of currents throughout this thesis.

1.1 Quantum Playground: Semiconductor Nanostructures

With the standardization of the nanofabrication procedures of semiconductor heterostructures, 2-dimensional electron gases (2DEGs) became the most common and practical framework of choice for research on quantum transport: current nanotechnology is able to provide arbitrarily large disorder-clean samples where electrons are completely confined on a plane, in a geometry that can be controlled with high precision at the local level, and where the many effective theories for the electron dynamics are now very close to the realistic description of the nanodevices.

In this thesis we will be concerned with one particular setting among the many possible transport configurations with 2DEGs[1], where the 2D-metal is maintained at very low temperature in the presence of an applied High magnetic fields perpendicular to the plane. In this situation the so called *Integer Quantum Hall* (IQH) regime is achieved, and we refer to the nanostructure as to a (quantum) *Hall bar*.

1.1.1 Phenomenology of 2DEGs at High Magnetic Fields

The IQH regime manifests itself as a spectacular transport anomaly in the conductance and resistance of the 2DEG: in a four-terminal geometry, while varying the magnetic field the longitudinal resistance is zero except for some sharp spikes, in correspondence of which the transverse resistivity (or Hall resistivity, measured with voltage probes through Ohm relation) jumps between constant values.

This originally puzzling behavior becomes clear when the quantum theory of the independent electrons on a plane is considered. Indeed, as it will be precisely formalized in Section 1.2, the quantization of transport observables and their mutual relation is a direct consequence of two facts

1. The energy spectrum of an unconfined 2DEG at High magnetic fields becomes quantized with energy levels (*Landau Levels*) equispaced and highly degenerate.

2. At any energy, current-carrying extended states states exists at the edge of the 2DEG, while in the bulk the individual electron states are quantized.

The first point is a straightforward result of the Quantum Mechanical solution of the single-electron problem: the eigenspectrum of the 2DEG Hamiltonian results in energies

[1] For a review on transport in Nanostructures, see Refs. [1, 2]

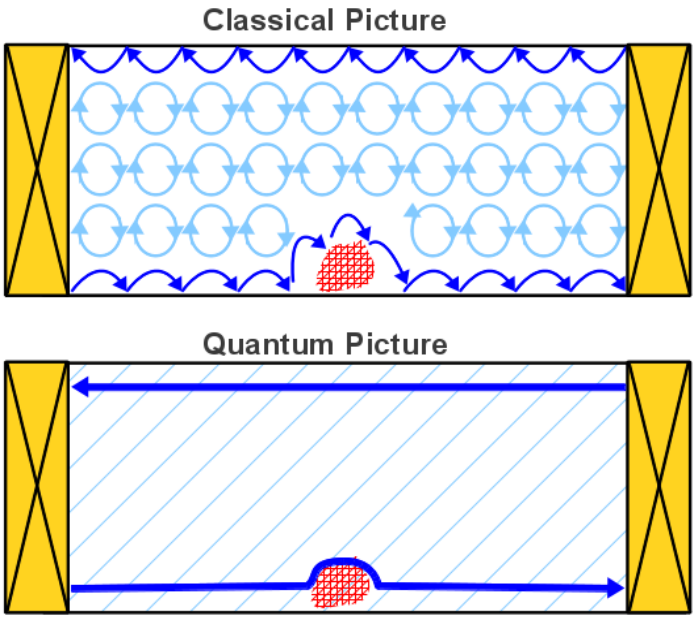

Figure 1.1: **Top panel**: pictorial view of the classical 2DEG when a strong perpendicular magnetic field is applied. Cyclotron orbits are closed in the bulk while they are "skipping" along the edge. The red hatching represents some localized smooth potential fluctuation. **Bottom panel**: quantum view of the IQH effect, chiral (unidirectional) channels connects the terminal, irrespective of the localized smooth perturbations.

of the form

$$E_n = \hbar\omega_c(n + \frac{1}{2}) \ , \tag{1.1}$$

for $n = 0,\ 1,\ \ldots$, where $\hbar\omega_c = \hbar\,|e|\,B/m$ is the *cyclotron energy*. The second point is intuitive, as the classical picture of charged particles (of charge e) with velocity $\vec{v}$ in a magnetic field $\vec{B}$, predicts that the electron would follow a circular orbit due to the Lorentz force $F = e(\vec{v} \times \vec{B})$. In this sense the electrons in the bulk are "localized" within a region of the cyclotron orbit diameter,[2] which in the quantum regime is of the order of the so called *magnetic length* $l_B = \sqrt{\hbar/\,|e|\,B}$. At the edge, classically the electrons follow *skipping orbits*, i.e. they bounce on the confinement barrier and continue to move along the edge in a given direction without possibility of changing the sign of their drift velocity (See Fig.1.1). In the quantum world, the quantizations of this motion leads to the existence of *edge states* (ES) [4, 5]: 1-dimensional gapless energy states which represents *chiral*[3] electronic currents.

This thesis is about investigating and exploiting the extraordinary features of these states, used as transport channels for electronic currents. As we will discuss in the following, the ES are dispersionless channels which are topologically protected from backscattering, and energetically decoupled by the incompressible bulk states. In the following sections we will also discuss how these 1D channels are also stable against smooth variation on the electrical potential, how they can be split coherently and how their trajectory and chemical potential can be controlled by means of metallic gates.

[2] These states might contribute to the current in the system depending on the amount of disorder present in the Hall bar. We will disregard completely this opportunity by considering sufficiently clean samples in regimes where *percolation* through impurities is not relevant [3].

[3] The word "chiral" used for ES refers to the fact that the current carried by these states flow only with a given sign in the direction parallel to the edge of the sample.

1.1.2 Relevant Mesoscopic Scales

In order to set a common ground for the understanding of the rest of this work, it is important to familiarize with the values and the meaning of the physical parameters which characterize the IQH regime and the edge channels. In this thesis we are concerned with 2DEGs in a condition where the number of Landau Level which are occupied at ground state (the so called *Filling Factor*[4], indicated as ν) *is* either 2 or 4, and the exact value of the Fermi energy of the 2DEG is usually such that it is half-way in between two quantized energies[5].

Table 1.1 list some important quantities which are used extensively in this thesis and in the literature dealing with mesoscopic physics and IQH transport in Gallium Arsenide heterostructure (GaAs).

Physical Quantity	**Symbol**	**Expression**	**Typical Value**
magnetic length	l_B	$(\frac{\hbar}{\lvert eB\rvert})^{\frac{1}{2}}=\frac{25.6}{\sqrt{B}}\ nm$	$12\ nm$
cyclotron energy	$\hbar\omega_c$	$\hbar\frac{\lvert e\rvert B}{m}=1.728\times B\ meV$	$5\ meV$
Zeeman energy	ϵ_Z	$\mu g B_z$	$0.1\ meV$
thermal energy	k_BT	k_BT	$10^{-3}\ meV$
Fermi energy	ϵ_F	$\frac{\nu}{2}\hbar\omega_c$ (middle of plateau)	$5-10\ meV$
electronic density	n	$\frac{\nu}{2\pi l_B^2}$	$10^{11}\ cm^{-2}$
Fermi velocity	v_F	See Eq.(1.10)	$10^5 ms^{-1}$

Table 1.1: Typical Scales in IQH mesoscopic experiments, such as the ones discussed in this thesis. Typical magnetic field for achieving the IQH regime in GaAs-based 2DEG is about 5T.

Useful physical insights can be gained by comparing typical energy and length scales. In the following sections we will discuss the conditions of adiabaticity with respect to sharp variations of potentials in space, but it is also a good idea to keep in mind that the unit of energy $\epsilon = \hbar\omega$ of 1 meV in terms of k_BT corresponds to a temperature of 11.6 K, and to a frequency ω of 1.52 THz. These rates and temperatures have to be compared with energies and times of the considered effects in the models, in order to be able to understand whether approximate regimes such as "steady state transport" or "zero temperature" are indeed justified.

1.2 Wavefunctions of Edge Channels

In order to get acquainted with the phenomenology of IQH edge channels, in this section we will neglect the spin degree of freedom of the electrons and consider spin-degenerate edge channels. The latter are determined through the solutions of the time-independent Schrödinger equation (SEQ) $H\Psi(x,y) = E\Psi(x,y)$ with the single-electron Hamiltonian (in Landau gauge[6]) given by

[4]For the reader which is already familiar with the IQH effect, we note at this point that we are considering *spin-resolved* edge states, as detailed in the Sections 1.2.

[5]Experimentalist use to refer to this condition as "setting the working point at the middle of the ν-th IQH plateau"

[6]The Landau Gauge where the vector potential $\vec{A} = (0, x|e|B_z\hbar^{-1}, 0)$ is the most convenient choice for the system that we study, which is a rectangular Hall bar where edge states propagate in the y direction and the system is confined in the x direction.

$$H = \frac{\hbar^2}{2m}[-\frac{\partial^2}{\partial x^2} + (-i\frac{\partial}{\partial y} + \frac{|e|B_z}{\hbar}x)^2] + V(x) \ , \tag{1.2}$$

where e and m are, respectively, the electron charge and the effective electron mass, B_z is the perpendicular magnetic field. A confinement potential $V(x)$ assures the existence of chiral channels. This will be taken to be an infinite "hard wall" (hard-wall) as a first approximation

$$V(x=0) = V(x=L) = \infty \ . \tag{1.3}$$

1.2.1 Solutions of the Schrödinger Equation

Being the Hamiltonian translational invariant in the y direction, the eigenfunctions of Eq.(1.2) can be expressed as scattering states $\Psi(x,y) = \psi(x)e^{iky}$, so that the time-independent Schrödinger equation reduces to

$$[-\frac{\partial^2}{\partial x^2} + (k+\beta x)^2 - \epsilon]\psi(x) = 0 \ , \tag{1.4}$$

where $\beta = l_B^{-2} = |e|B_z/\hbar$ is the inverse magnetic length squared, $\epsilon = 2mE/\hbar^2 = 2\beta(E/\hbar\omega_c)$ is the rescaled effective energy. Note that edge states are transport channels defined at a precise energy ϵ_F, so what we need to solve is the SEQ at fixed energy ϵ. The energy of the first LL corresponds to $E = \hbar\omega_c/2$, which translates in $\epsilon = \beta$. The solutions for the transverse eigenfunction ψ subject to a potential described in Eq.(1.3) can be expressed in analytic form in terms of parabolic cylinder functions $\mathcal{D}_a(x)$ [6, 7]:

$$\psi(x) = \mathcal{N}_1 \mathcal{D}_{\frac{\epsilon}{2\beta}-\frac{1}{2}}(k\sqrt{2/\beta} + x\sqrt{2\beta}) + \mathcal{N}_2 \mathcal{D}_{-\frac{\epsilon}{2\beta}-\frac{1}{2}}(ik\sqrt{2/\beta} + ix\sqrt{2\beta}) \equiv \psi_k(x) \ , \tag{1.5}$$

where $\mathcal{N}_1$ and $\mathcal{N}_2$ should be chosen to satisfy the hard-wall boundary conditions $\psi(x=0) = \psi(x=L) = 0$, and the probability normalization $\int dx\,|\psi_k(x)|^2 = 1$.

At a given energy only few real wave-numbers k satisfy Eq.(1.5). This is clearly illustrated by the calculation of the *energy bands* $\epsilon_n(k)$ of the system, obtained by solving numerically the equation Eq.(1.4) spanning a given range of real wave-numbers k. The intersection of the dispersion bands with the energy lines $\epsilon_n(k) = \epsilon_F$ defines the wave-number of the edge states (see Fig.1.2).

We note that for $L = \infty$, Eq.(1.5) has still a normalizable solution, since the presence of the magnetic field is sufficient to provide an effective confinement potential unbounded from above. The *cyclotron-resolved* edge state modes for a semi-infinite 2DEGs are then [8]

$$\psi_k(x) = \mathcal{N}_k \mathcal{D}_{\frac{\epsilon}{2\beta}-\frac{1}{2}}(k\sqrt{2/\beta} + x\sqrt{2\beta}) \ . \tag{1.6}$$

A complete forward-moving solution of the SEQ at a given energy can be represented as an expansion over all the modes

$$\Psi(x,y) = \sum_k a_k \ [\mathcal{N}_k e^{-iky}\psi_k(x)] \ . \tag{1.7}$$

These modes satisfy the orthogonality relation for $k \neq k'$ [9]

$$\int \psi_k(x)\psi_{k'}(x)^*(k + k'^* + 2\beta) = 0 \ . \tag{1.8}$$

The current density of a complete solution of the SEQ (defined through the continuity equation $\frac{\partial}{\partial t}|\Psi(x,y,t)|^2 = -\vec{\nabla}\cdot\vec{J}(x,y,t)$ in the direction of propagation y is

$$J_y(x) \equiv \frac{\hbar}{m}\mathrm{Im}\int \Psi(x,y)^*(\partial_y + \beta x)\Psi(x,y) = \sum_k a_k v_F(k) \ , \tag{1.9}$$

while in the transverse direction the current is zero. The introduced *Fermi velocity* $v_F(k)$ can be calculated[7] as

$$v_F \equiv \frac{1}{\hbar}\frac{\partial E}{\partial k} = \frac{eB_z}{m}\int \psi_k(x)^2(k+\beta x)dx \ . \tag{1.10}$$

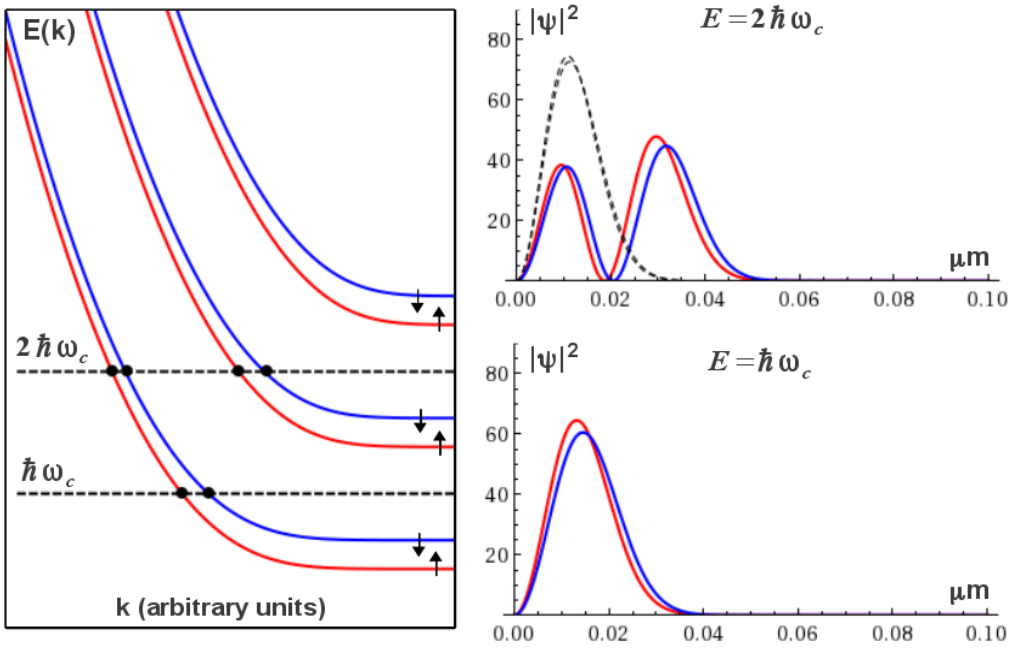

Figure 1.2: Edge States dispersion bands and transverse wavefunctions profiles for $\nu = 2$ and $\nu = 4$. **Left panel**: energy dispersion for a semi-infinite hard-wall confinement potential model. Spin-resolved (spin ↑ in red, spin ↓ in blue) dispersion relations are plotted, and their intersections with the energy levels $E = \hbar\omega_c$ and $E = \hbar\omega_c/2$ are highlighted. Zeeman energy has been taken to be 8.5 times smaller than the cyclotron gap, for clarity of the figure. **Right panel**: profiles of $\psi_k(x)$ corresponding to the states highlighted in the left panel. Normalization of the wavefunction in arbitrary units. The dashed lines in the top-right panel correspond to the outer edge channel ($n = 0$) for $\nu = 4$. In these examples the magnetic length is 0.12 nm. All plots shown in the figures has been computed by numerically solving the SEQ. Note that bands and wavefunctions for cyclotron resolved edge channels (not shown) lie in between the red and blue curves of the panels.

Numerical Solution of the Schrödinger Equation In this thesis we will opt for a numerical solution of the SEQ following the technical strategy detailed in the appendix of Ref. [10]. In practice we discretize Eq. (1.4) in the x variable ($x \equiv x_n$, with $n = 1, 2 \ldots N$). By exploiting the very definition of derivative $\partial_x\psi(x) = \lim_{\epsilon\to 0}\eta^{-1}(\psi(x+\frac{\epsilon}{2}) - \psi(x-\frac{\epsilon}{2}))$ and fixing η to a given discretization step a (so that $x_n = na$) small with respect to the scales of variation of the wavefunction, we can replace in Eq.(1.4)

$$\frac{\partial^2\psi}{\partial x^2} \longrightarrow \frac{\psi(x_{n+1}) + \psi(x_{n-1}) - 2\psi(x_n)}{a^2} \ , \tag{1.11}$$

[7] We note that in this hard-wall model v_F is different for each mode ($v_F \equiv v_F(k)$).

so that the SEQ in terms of wavefunction vector components $\psi(x_n)$ is cast in terms of a linear system which can be solved with standard methods[47]

$$a^{-2}\begin{bmatrix} f(x_1) & -1 & 0 & \dots & \\ -1 & f(x_2) & -1 & \dots & \\ 0 & & \ddots & & \\ & \dots & -1 & f(x_{N-1}) & -1 \\ & & & -1 & f(x_N) \end{bmatrix}\begin{bmatrix} \psi(x_1) \\ \psi(x_2) \\ \vdots \\ \psi(x_{N-1}) \\ \psi(x_N) \end{bmatrix} = \begin{bmatrix} 0 \\ 0 \\ \vdots \\ 0 \\ 0 \end{bmatrix} , \qquad (1.12)$$

where $f(x_n) = a^2(x_n + k)^2 - \epsilon + 2$.

1.2.2 Spin-Resolved Edge Channels

The introduction of the Spin degree of freedom in the Hamiltonian is realized by adding a term (the *Zeeman Hamiltonian*) to Eq.(1.2)

$$\Delta H = g\mu_B \left(\vec{\sigma} \cdot \vec{B}\right) , \qquad (1.13)$$

where g is the *gyromagnetic factor*, or *g-factor* (and $\mu_B = e\hbar/2m$ is the Bohr magneton). This dimensionless constant physically represents the proportionality factor between the electronic angular momentum and its magnetic moment. g for free electrons can be computed exactly with high precision by means of Quantum Electrodynamics, but in a solid state environment it heavily depends on the material which hosts electrons, and on the effects of external fields. In Gallium Arsenide heterostructures under standard conditions its value is measured as -0.44,[8] but in the IQH regime its value depends as well on the bulk-filling factor due to interactions effects, and its effective value (usually denoted as $g^\star$) can become as big as 20 [12, 13, 14].

The definition of g is somewhat more complicated when considering electrons at the edge of 2DEGs, where the spin-resolved ES are degenerate in energy. The same effects that renormalize the g-factor in the bulk are influenced by the shape of the confinement potential, and contribute to determine crucial parameters such as the spatial separation of the edge channels and their Fermi velocity.

In order to discuss ES-transport in the non-interacting limit, it is a useful prescription to map the effect of the interactions by considering the effect of ΔH independently from the confinement, bearing in mind that the effective g-factor used in ΔH is a phenomenological parameter which is in general much larger than the bare one, and its value is chosen so to reproduce the physics at the edge.

Once these considerations are made, the model is only mildly complicated by the electronic spin. The perpendicular magnetic field B_z which is at the origin of the IQH determines the *Zeeman Energy Gap* of the system $\epsilon_Z = 2\mu g B_z$, which will influence the band spectrum. The new analytic eigenfunctions for the ES are indeed:

$$\Psi_\sigma(x, y) = e^{ik_\sigma y}\psi_k(x, \epsilon + \sigma\epsilon_Z) , \qquad (1.14)$$

where we explicitly wrote the energy dependence of the wavefunction $\psi_k(x, \epsilon)$ which defined through Eq. (1.6). At fixed energy, for a given spin-projection σ, there will be a set of wave-numbers k_σ. Note that the states described by Eq. (1.14) are orthogonal in the spin-sector of the Hilbert space, so transitions from one ES to another are not allowed unless a spin-flipping Hamiltonian is involved.

The spin-resolved bands $\epsilon_\sigma(k_\sigma)$ can be computed and the difference between spin-resolved wavevector,$\Delta k = k_\uparrow - k_\downarrow$, can be determined by solving $\epsilon_\uparrow(k_\uparrow) = \epsilon_\downarrow(k_\downarrow) = \epsilon_F$

[8] g is operatively defined as the energy gap necessary to flip a spin from one Landau level in the bulk, and can be measured in a number of way, exploiting optics or temperature effects.

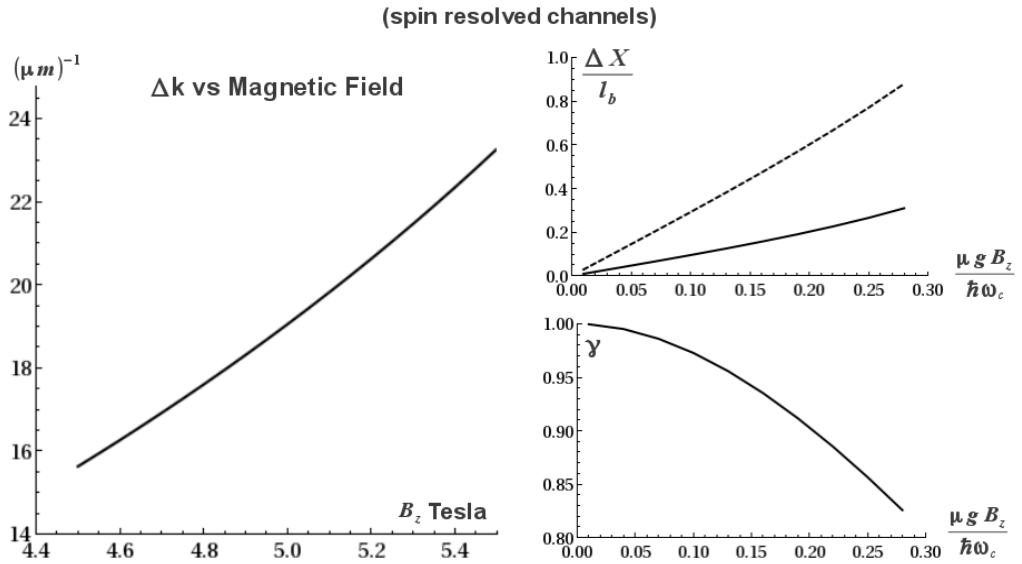

Figure 1.3: **Left panel**: fixing a given g, in the hard-wall-model the wave-number separation increases with increasing perpendicular magnetic field. The corresponding linear increase in the edge state separation ΔX and decrease in the overlap γ is very small. **Top right panel**: physical separation of edge channels computed with Eq.1.26, for different g (at $B_z = 4.75$). The dashed line is the $\alpha = 0$ approximation (soft potential, see Section 1.3.3). **Bottom right panel**: transverse function overlap decreases with increasing g (at $B_z = 4.75$), as the channels are further away (see also Fig.1.2). All plots shown in the figures has been computed by using Eq.(1.6). In all these calculations we are considering $E = \hbar\omega_c$.

(we did this in Fig.1.2 and 1.3). Quantities such as Δk and the wavefunction overlap $\gamma = \int dx \psi_{k\uparrow}(x)\psi^*_{k\downarrow}(x)$ are related with the spatial separation of edge channels (see Section 1.3.3) and will be important for the *periodic poling* effect, discussed in Section 2.2.3 and tested in Section 3.3.

1.3 Edge State Transport Properties and Interferometry

The scattering approach [15] describes quantum electronic transport in a mesoscopic system in terms of its *transmission coefficient* $T(\epsilon)$. It physically represents the probability of the transfer of individual electrons (or electronic wavemodes), which are considered to be independent and non-interacting, through the device.

1.3.1 Landauer-Buttiker Formalism and the Scattering Matrix Approach

In its simpler formulation the approach is founded on a calculation for the *steady state* current, based on the existence of *reservoirs* where local equilibrium is attained, and which are conceptually considered the *sources* and *drains* of forward-moving/backward-moving modes (see Fig.1.4). The result is the Landauer-Buttiker (LB) formula for the current between reservoirs L (left) and R (right)

$$I = \frac{e}{\pi\hbar}\int_{-\infty}^{+\infty} d\epsilon [f_L(\epsilon) - f_R(\epsilon)] T(\epsilon) \ . \tag{1.15}$$

The *distribution functions* $f_i(\epsilon)$ describing the local equilibrium of the reservoir are

$$f_i(\epsilon) = \frac{1}{1+\exp\left(\frac{\epsilon-\mu_i}{k_B T}\right)} . \tag{1.16}$$

For typical sources/drains this is the Fermi distribution function which includes the effect of the temperature T and the chemical potentials μ_i whose relative differences define the non-equilibrium current.

In the LB-approach the measured current is interpreted as the flow of the excess carriers, determined by the imbalances (*voltage bias*) of chemical potentials of source/drain reservoirs.

For small bias $\mu_L - \mu_R = eV$ and temperature $T \simeq 0$ (compared to the equilibrium Fermi energy ϵ_F) we can approximate the LB formula to

$$I = \frac{2e^2}{h} T(\epsilon_F) V \tag{1.17}$$

Where the transmission coefficient $T(\epsilon_F)$ is now proportional to the total *conductance* of the system.

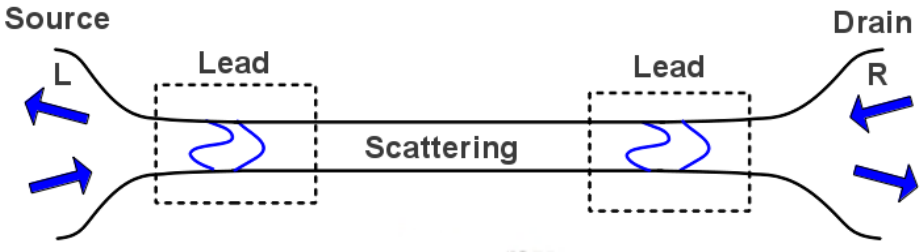

Figure 1.4: Conceptual view of the scattering approach: scattering amplitudes are defined by modes of the leads, which are connected to the reservoirs. The modes in the leads are divided in forward-moving (e.g. arrow pointing to the right in the L reservoir) and backward-moving (e.g. arrow pointing left in L).

1.3.2 Current from the Scattering Amplitudes

Once we modeled the electric contacts as reservoirs, the quantity $T(\epsilon)$ phenomenologically encodes all the microscopic details of the probed transmission channel. In non-interacting models the transmission coefficient is directly linked to the solution of the SEQ in the region between the source and the drain. As clear from the Eq.(1.17), we are interested in the solutions at fixed energy ϵ_F.

In the scattering approach this zone is considered to be connected to the reservoirs through perfect, semi-infinite conducting waveguides (*leads*). In these "asymptotic" regions, the propagating electronic modes are perfectly defined because of the translational invariance in the y direction. For lead i, the electronic mode characterized by quantum number k has the form[9]

$$\Psi_k^i(x, y; \epsilon_F) = \psi_k(x) e^{iky} . \tag{1.18}$$

[9] In this section we are using the symbol $\psi_k(x)$ for generic transverse wavefunctions of the leads, while in previous sections this symbol was reserved to ES defined in Eq.(1.6). This is because edge states are indeed the transverse wavefunctions defining lead modes in the scattering approach applied to IQH system, as detailed in Section 1.3.3.

For $k \in \mathbb{R}$, the mode will be *propagating*, and can be either forward-mover or backward-mover with respect to the scattering region (see Fig.1.4, top panel).

A complete solution of the SEQ in the one lead region can be written as

$$\Psi^i(x, y; \epsilon_F) = \sum_k M_k \psi_k(x)\, e^{iky} \ . \tag{1.19}$$

This general form of the solution in all regions will be considered as the output of the evolution of an *incoming* (forward-mover in region L) electronic mode in the source lead:

$$\psi_q^L \longrightarrow \sum_\kappa t_{q\kappa}\psi_\kappa^R + \sum_k r_{qk}\psi_k^L \ . \tag{1.20}$$

An analogous relation can be written for an incoming mode in region R.

The amplitudes of superposition of the resulting wavefunctions expanded over the modes of the leads define the *transmitted* ($t_{q\kappa}$) and *backscattered* (r_{qk}) modes. Unitarity of the evolution implies the unitarity of the *Scattering Matrix* $\mathbf{S}$, which encodes the linear relation between incoming modes and transmitted/backscattered modes. By collecting right (left) movers modes in vectors denoted as $[\vec{\psi}^i_\rightarrow]$ ($[\vec{\psi}^i_\leftarrow]$)

$$\begin{pmatrix} \begin{bmatrix} \vec{\psi}^L_\rightarrow \end{bmatrix} \\ \begin{bmatrix} \vec{\psi}^R_\leftarrow \end{bmatrix} \end{pmatrix} = \mathbf{S} \begin{pmatrix} \begin{bmatrix} \vec{\psi}^R_\rightarrow \end{bmatrix} \\ \begin{bmatrix} \vec{\psi}^L_\leftarrow \end{bmatrix} \end{pmatrix} = \begin{pmatrix} \mathbf{t} & \tilde{\mathbf{r}} \\ \mathbf{r} & \tilde{\mathbf{t}} \end{pmatrix} \begin{pmatrix} \begin{bmatrix} \vec{\psi}^R_\rightarrow \end{bmatrix} \\ \begin{bmatrix} \vec{\psi}^L_\leftarrow \end{bmatrix} \end{pmatrix} \tag{1.21}$$

$$\mathbf{S}\mathbf{S}^\dagger = \mathbb{I} \tag{1.22}$$

Where $\mathbf{t}$, $\tilde{\mathbf{t}}$ are transmission (sub-)matrices and $\mathbf{r}$, $\tilde{\mathbf{r}}$ are reflection matrices.

An explicit example of the construction of the Scattering Matrix from a microscopic Hamiltonian will be given in Section 2.1.

The Scattering Solution For non-zero magnetic field, the total current in the direction of propagation at equilibrium is defined as in Eq.(1.9) for the y direction. In one lead it would be

$$I^i_{tot} = \int dx J_y(x) = \frac{\hbar}{m}\int_0^L dx \mathrm{Im}[\Psi^i(x, y; \epsilon_F)^*(\frac{\partial}{\partial y} + \beta x)\Psi^i(x, y; \epsilon_F)] \ . \tag{1.23}$$

Computing this current in the right lead with the input *ansatz* of one mode characterized by wave-number q (1.20) leads to

$$I^R_q(y) = \sum_\kappa |t_{q\kappa}|^2 \frac{v_F(\kappa)}{L} \ , \tag{1.24}$$

where v_F is defined as in Eq.(1.10).

The Landauer Formula (1.15) is obtained by statistically weighting the contributions of each incoming mode a, q with a factor that consists of the product of the occupation probability (1.16) and the density of states.[10]

While the physical interpretation of this scattering approach is transparent, the magic of turning a complicated physical problem of dynamics of an open quantum system into a calculation of simple observables does not come for free. In order to connect Eq.(1.20) to time-dependent quantum mechanics we need to make many assumptions (independent channels, ideal stationary transport...) and approximations (mean field Hamiltonian, closed infinite system and pure state...) [16].

[10] the density of states in 1D, for a linear dispersion is just $L[2\pi\hbar v_F^\alpha(k)]^{-1}$.

In Chapters (2),(3) we will apply the LB formula (and equivalent forms) for computation of *steady-state* (i.e. time-independent) currents in the limit of *zero-bias*, so that the non-equilibrium aspect of the problem is reduced to the minimum. A more general framework for calculating transport observables without making all the assumptions of the scattering approach will be reviewed in Chapter 4.

1.3.3 Non-interacting Transport Model for Edge Channels

The scattering formalism described in the previous section applies to general quantum conductors in the presence of magnetic fields, and it is therefore adaptable for the scattering states defined by edge channels as studied in the previous chapter. Some comments are nevertheless necessary to understand how the special characteristics of the ES reflect on the LB approach.

First, the localization of the scattering states on the edges of the conductor, whose width L is considered to be much larger than l_B, makes it hard for local, point-like scattering centers to introduce any backscattering, as discussed in Section 1.1. This formally means that, unless we have extended scattering regions in the scattering zone, the elements of the reflection submatrices $\mathbf{r}$ and $\tilde{\mathbf{r}}$ in Eq.(1.21) are likely to be exponentially vanishing as L increases, up to becoming completely negligible for large L. This will allow us, in scattering effective models, to discuss only transmission properties and exploit the fact that the sequential application of several transmission matrices is just the product of the matrices (see for example Section 2.2.1).

A second technical point that we would like to stress is that in the presence of magnetic field the k-wave-numbers are not proportional to the proper momentum observables, and indeed their value is dependent on the boundary conditions Eq.(1.3).[11] By fixing the hard-wall in the reference system where it is located at $x = \pm\frac{L}{2}$, the ES solutions of the Schrödinger equation are symmetric (see Fig.2.1 picturing scattering in a IQH system) so that incoming and outcoming scattering states are identified by the same absolute value of the real wave-number k, with opposite sign.

Selective Population of Edge Channels As discussed in the previous sections, ES are current-carrying proper solutions of a closed quantum mechanical problem, so the existence of a steady-state current is not necessarily a non-equilibrium phenomenon. Accordingly to the scattering approach, when the IQH system is contacted to electrodes, the edge channels have now to equilibrate their state with the chemical potentials of these contacts. The interpretation of the LB formula (1.15) is that the ES which leave a given contact gets filled up to the energy defined by the bias of the contact, while the ES entering in a given contact get lost and equilibrate[12] [68].

The extraordinary feature that is peculiar to the transport with ES comes from the fact that, differently to the "standard" non-interacting system at $B = 0$, the wavefunctions of the states traveling in opposite directions are macroscopically separated, so any local perturbation on the channel can in principle act only on states with a definite sign of the velocity. This leads also to the property of absence of backscattering which has been introduced in Section 1.1.1: the edge channels are forced to bypass in some way whatever local perturbation, as in the local vicinity there is no density of states for reflected, propagating states.

[11] On the contrary, the wave-number difference Δk between two ES has a direct physical meaning, as it will be enlightened in Section 2.2.3.

[12] In reality the proper understanding of how and where the voltage drop occurs in the Hall bar is still an open problem. However, for the sake of computation of current signals from terminal to terminal, at low voltage biases, the non-interacting picture described here and used in the following sections is simple and accurate.

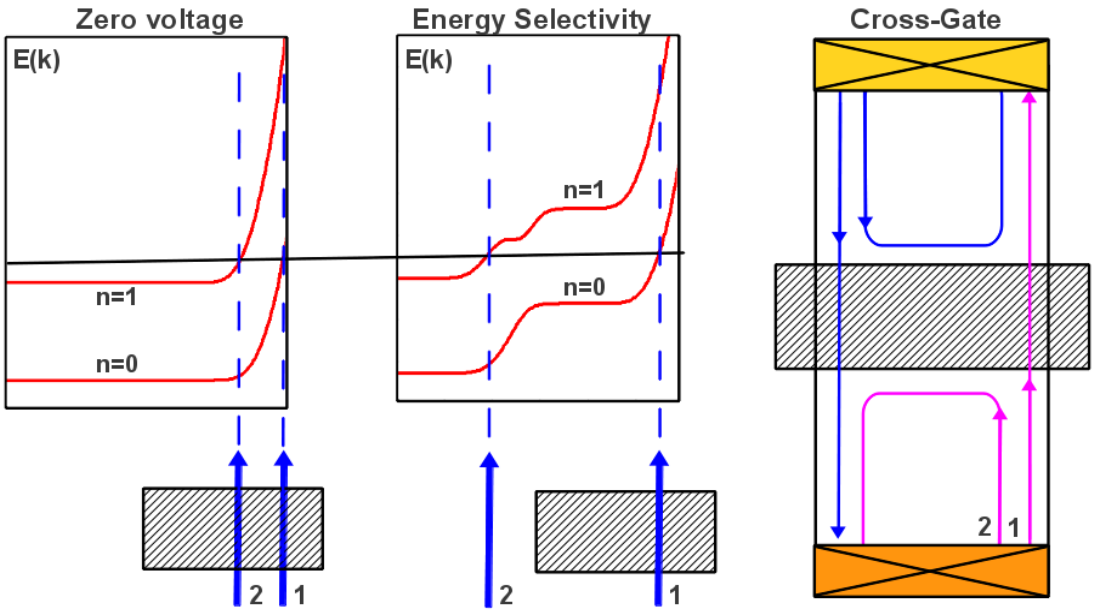

Figure 1.5: **Central panel**: when a high voltage is applied, one Landau band is warped so that its intersection at the Fermi level localizes the ES outside the gate region. The black horizontal line represents the Fermi level. **Left panel**: the gate region is unbiased and the ES are maximally close in k-space (and in real space). **Right panel**: pictorial view of the cross-gate technique: under the gate only one channel (1) is allowed to propagate: the outer (2) ES is necessarily reflected. Purple channels are biased with the chemical potential of the bottom contact, wile blue channels are at equilibrium with the top contact. Band curves in the left/right panels have been obtained by numerically solving the SEQ.

These two effects are exploited in the *cross-gate* [19, 20] technique: during nanofabrication of the device, vast regions of the 2DEG can be covered by a metallic gate which will be electrically polarized so to energetically interdict the passage of electrons belonging to a given sub-band. Effectively, the regions below the gate are maintained to a bulk filling factor lower than the one determined by the Fermi energy and the magnetic field (see Table 1.1). From a technological point of view, this results in the opportunity to separate adjacent co-propagating ES by an arbitrarily large distance, and to address each channel separately with local elements of the nanocircuit. One of the most useful applications of this technique is the so-called *selective population* of edge channels: each ohmic contact that injects or detects carriers can access independently each channel. This is pictured in Fig.1.5 for a two-terminal device [13]. By computing the energy bands under the effect of a lateral potential step (which mimics the effect of the gate) we show that the edge channels do separate in k-space at the Fermi energy. As it will be clarified in the next section, the difference in wave-numbers results in a separation in space, so the outer edge 1 is allowed to cross the gate maintaining the chemical potential defined by the bottom contact. After passing the middle-region the two co-propagating ES will be associated to different voltage bias.

While the real electrostatic effect which allows to filter out and energetically de-

[13] The dip in the N=1 Landau level edge band which is observed in the central panel of Fig.1.5 is related to a feature of the eigenenergies of the non-interacting electron problem in a infinite system at $B \neq 0$ in the presence of a high potential step [17], called "Landau Gap Reduction". If the gate region is very close to the confinement potential, this effect is not observed.

flect some channels is likely to be more complicated at high bias due to capacitance effects [21], this technique works very well at low bias and will be explicitly used in the following sections, or its use will be implied wherever the channels must be addressed individually for the transport measurement/calculation.

Adiabatic Transport and Confinement Potential Since we are dealing with 1-dimensional channels whose wavefunctions are localized close to the edges of the 2DEG, it seems physically important to understand whether these states are overlapping in space or are physically separated (adjacent). We already observed that the typical variation scales of the lobes between the zeros of the transverse wavefunctions are of the order of l_B. The *guiding center* of the wavepackets on the ES can be defined as

$$\langle x \rangle \equiv \int x \left|\psi_k(x)\right|^2 dx = \frac{v_F}{\omega_c} - k l_B^2 \ , \tag{1.25}$$

(we used Eq.(1.8)) so that the average separation between edge channels is

$$\Delta X = \langle x_1 \rangle - \langle x_2 \rangle \simeq l_B^2 (1+\alpha) \Delta k \ , \tag{1.26}$$

where α is a small correction factor which depends on the local slope of the potential bands. For states in the bulk (infinitely flat bands) $\alpha = 0$, and Δk determines completely the separation between the localized states. For the hard-wall potential we observe a linear dispersion relation which results in a small change in the Fermi velocity between the modes and thus a non-zero α. For smooth confinement potentials, however, a semi-classical treatment [5], and a general local flat-band approximation leads to the *adiabatic* following of the equipotential lines

$$E_{nk\sigma} \simeq \hbar\omega_c (n + \frac{1}{2}) + \sigma \mu g B + V(\langle x \rangle = k l_B^2) \ , \tag{1.27}$$

which leads to a Fermi velocity expression which is independent of on n and σ, but depends on the local slope of the confinement potential

$$v_F \simeq \frac{1}{eB} \frac{\partial V}{\partial \langle x \rangle} \ . \tag{1.28}$$

A consequence of these estimates, which has been used several times to estimate the physical separation between the channels in experimental works, is that (for a smooth linear potential) the spatial separation of the ES can be rapidly evaluated by an energy-balance argument: the external confinement field must work against the energy gap in order to make the channels degenerate in energy:

$$e \left.\frac{\partial V}{\partial x}\right|_{x=\bar{k} l_B^2} \Delta X = \Delta\epsilon \ . \tag{1.29}$$

While it is experimentally very tricky to measure the edge state separation for spin-resolved ES, several solid hints can be extrapolated for cyclotron-resolved ES [22]. If we consider $V(x)$ to be linear all over the region, we could use the experimental value of ES separation δX_c for $\Delta\epsilon = \hbar\omega_c$ to deduce by proportionality the ΔX for spin-resolved channels: $\Delta X \simeq \frac{\epsilon_z}{\hbar\omega_c} \delta X_c$. For spin-resolved channel these estimates leads to typical separation between the ES of some hundreds of nanometers.

1.3.4 Edge State Interferometry

While the interference effects of coherent electrons in mesoscopic devices have always been one of the main sources of research interest since the fabrication of the first 2DEG, the field of edge-state coherent interferometers is relatively recent, and emerged manifestly with the groundbreaking experiment of M. Heiblum et al. in 2003 [23]. While several more complicated interferometric setups have already been fabricated and tested [24, 25], the simple *Mach-Zehnder Interferometer* (MZI) is a still actively explored scheme, both experimentally and theoretically, and several surprising details concerning the coherence and the non-equilibrium dynamics of the interfering electrons are still puzzling the scientific community (see [134, 27] and Chapter 4 of this thesis).

In Fig.1.6-a we show the basic idea of a MZI: a "beam" of electrons traveling in a IQH edge channel is coherently divided by a *beamsplitter*, which effectively delocalizes each electronic wavepacket on two different paths of the interferometer. The two trajectories are joined after some distance (which is different for each of the two possible paths), and the splitted wavepacket is recombined by a second beamsplitter.

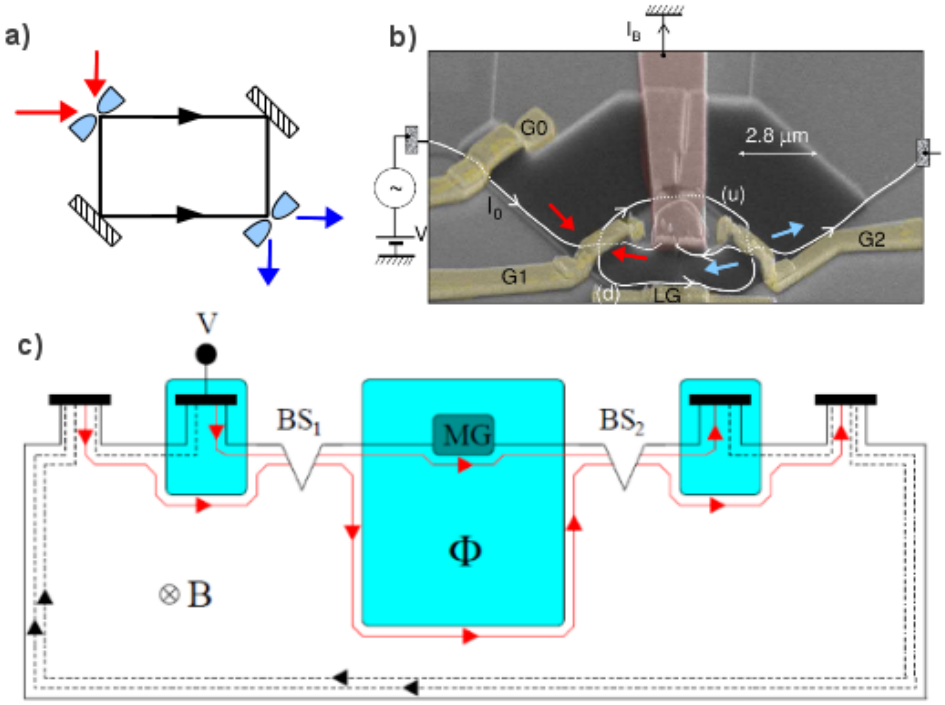

Figure 1.6: **a)** Schematics of a MZI: two input channels (red) and two output channels (blue) are highlighted. **b)** Recent experimental realization of a MZI (Figure taken from Ref. [25]) where it is clear that the output channels are counter-propagating and necessarily separated in space **c)** figure adapted from Ref.[26] of a scalable MZI that exploits interference and mixing of co-propagating ES (BS_1 and BS_2 are the channel couplers, MG is a lateral gate meant to tune $\Phi = \Delta\phi$).

The relative phase difference $\Delta\phi$ between the edge states controls the transmission amplitude for each of the two possible output channels after the second beamsplitter. If we do not consider Coulomb interactions, this phase mainly depends on the relative lengths of the channels (kinetic phase difference), on their different characteristics (difference in Fermi velocities), and on the total external magnetic field flux enclosed by

the two trajectories (Aharonov-Bohm phase).

The resulting coherent delocalization of the electronic current over two separate channels, tunable through $\Delta\phi$, suggests that MZI-schemes could be exploited as an interesting unitary "quantum gate" acting on *dual-rail* flying-qubit quantum information procedures [28].

Mixing between Co-propagating Channels and Spin-interferometry The "standard" implementation of the Quantum-Hall MZIs makes use of different physical edges of the 2DEG in order to define the two interfering paths, and employs metallic constrictions known as *quantum point contacts* (QPC) as beamsplitters (See Fig.1.6-b); these choices usually result in a 2DEG device with an inherent topological impossibility to make use of the quantum information carried out by the two output channels for further single-qubit manipulation.

Ref. [26] discusses a conceptual extension of the typical architecture of MZIs that uses adjacent *co-propagating* edge channels as quantum states (i.e. rails), and generic inter-channel elastic scatterers as beamsplitters. Control on the relative phase $\Delta\phi$ of these channels is possible by physically separating the channels through adiabatic cross-gate separation in specific regions discussed in Section 1.3.3 (Fig. 1.6-c). This interferometry scheme has the great benefit to be straightforwardly *scalable*, so that the outcoming state can be processed in sequence by an arbitrary number of MZI.

The question of how to implement the inter-channel coupling of these device is one of the central motivations of this thesis, and we will discuss in chapters 2-3 several strategies of *quantum-engineering* for the implementation of these beamsplitters either for cyclotron-resolved or spin-resolved ES. For the former, we will study the influence of abrupt variation of the local electric potential landscape which will break the adiabatic transport regime discussed in Section 1.3.3. For the latter we will study spin-coupling mechanisms, such as external in-plane magnetic fields.

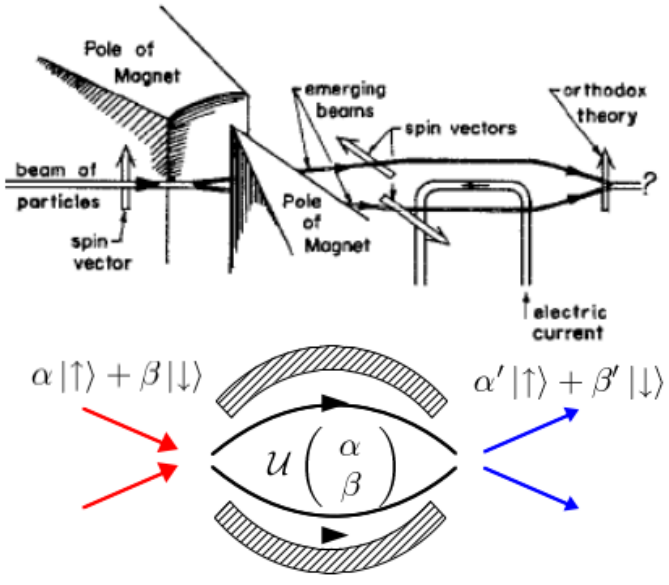

Figure 1.7: **Top panel**: figure adapted from Ref.[29]: the "classic" Stern-Gerlach experiment. By means of an inhomogeneous magnetic field a given spin projection is decomposed in components in a rotated basis whose relative phase is controlled. **Bottom panel**: Quantum Gate equivalent of a SGI: the transverse magnetic field acts as a unitary operation on the spinor (α, β) resulting in a qubit rotation.

We would like to note that for spin-resolved channels the realization of a scalable MZI would be particularly interesting, since the resulting spin-interferometer would be a mesoscopic analogous of the *Stern-Gerlach Interferometer* (SGI, see Fig. 1.7) which is often evoked as a the fundamental Gedanken device for discussion of interparticle entanglement (spin and orbital state) and for considerations about the measurement problem [29] of quantum-mechanics.[14]

SGI have been realized and tested with neutrons [31], but their realization in mesoscopic physics proves very challenging, despite the many different proposals [32, 30].

In addition to the fundamental study of quantum interference, the coherent control of the electronic spin degree of freedom provides a qubit which can be physically transferred *in space*. This is an attractive opportunity for the field of spin-based quantum computing [33], as the ES have been recognized as ideal channels for the routing of electronic "flying qubits" [34], and several schemes of quantum information processing have been proposed in the literature [35].

[14] We note that the acquisition of a phase difference $\Delta\phi$ between the channels by means of a top-gate or by an asymmetry between the band dispersion of the ES is a purely orbital effect. In spin-resolved ES this phase difference can nevertheless act as a spin-phase on the Bloch-Sphere when the channels are recombined. This occurs because the spin and orbital states are entangled. In Chapter 4 we discuss a model where this effect is triggered by the Fermi velocity asimmetry of the spin-resolved channels.

2 Channel Mixing Induced by Electric and Magnetic Potentials

In this chapter we employ the Mode-Matching method for the determination of the scattering matrix associated to a simple non-homogeneous potential. We study the charge transfer between two cyclotron-resolved edge channels by means of a sharp potential variation in the propagation region of the edge states. We also discuss the effect of several of such potential inhomogeneities and the importance of the phase differences acquired by the electrons between scattering events for determining the amount of channel mixing. We also present different strategies for obtaining a significative coupling of the channels.

2.1 The Mode-Matching Method and Evanescent States

Given a solution Ψ of the translationally invariant Hamiltonian (1.18), the normalizability of this form of wavefunction implies that k must be real, otherwise the wavefunction will explode exponentially in one direction, and will be exponentially damped in the other. However, in the scattering approach these states are solutions of the SEQ (1.4) only in some region of space (right or left lead): so the exponentially damped solutions, called *evanescent* states, must be considered for properly finding the stationary wavefunction.

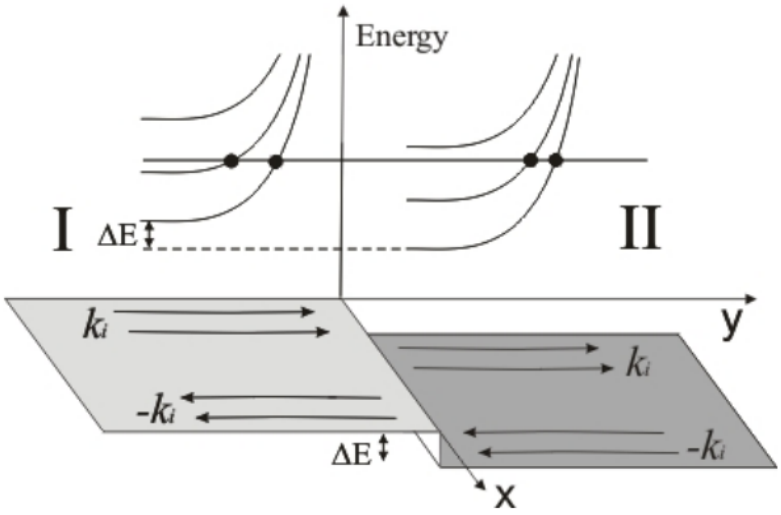

Figure 2.1: The scattering regions for a single non-adiabatic potential step ($x \in [-L/2, L/2]$). Along the longitudinal direction y a step potential $U(y)$ is introduced to induce coherent mixing among the propagating modes. Its effect is accounted as a global energy shift between the solutions of the Schrödinger equation in the two regions, as pictured on the dispersion band curves of the edges drawn on the background of the figure (the horizontal line that intersects the bands indicates the Fermi energy).

To be more precise, given the energy E^i of one region, the solutions whose k has zero imaginary part are associated to propagating longitudinal wave-functions which correspond to the $2P_i$ edge-state channels ($P_i = \nu$).[1] If we consider the reference frame setting the hard-wall at $x = \pm\frac{L}{2}$, we can identify P_i real positive wave-numbers $\{k_n^i;\ n = 1, \cdots, P_i\}$ that describe propagating right-going channels $\{\psi_n^{Ri}(x);\ n = 1, \cdots, P_i\}$, and P_i real negative solutions $\{-\kappa_n^i;\ n = 1, \cdots, P_i\}$ that describe propagating left-going channels $\{\psi_n^{Li}(x);\ n = 1, \cdots, P_i\}$. Such modes are responsible for the electronic transport in the sample in the asymptotic limit, but all modes contribute to the definition of the **S** matrix.

One way to construct explicitly the Scattering matrix, is to use the *Mode Matching* (MM) method [10], which relies on the basic quantum mechanical fact that each wave-function of a given Hamiltonian must be continuous and differentiable in every point of the space. To make things more explicit, if we consider $y = 0$ as the boundary between two regions (I and II, also pictured in Fig.2.1) of the scattering zone:

$$\begin{aligned} \Psi^{\mathrm{I}}(x, y = 0) &= \Psi^{\mathrm{II}}(x, y = 0)\ , \\ \partial_y \Psi^{\mathrm{I}}(x, y = 0) &= \partial_y \Psi^{\mathrm{II}}(x, y = 0)\ . \end{aligned} \tag{2.1}$$

These equations are readily translated on matching conditions for the eigenmodes of the regions I and II, as we are detailing now. In a given scattering region i, a generic solution of the SEQ can be written as

$$\Psi^i(x, y) = \sum_{n=1}^{P_i} a_n^i \psi_n^{Ri}(x)\, e^{ik_n^i y} + \sum_{n=1}^{P_i} b_n^i \psi_n^{Li}(x)\, e^{-ik_n^i y} + \sum_{n=1}^{Q_i} c_n^i \bar{\psi}_n^i(x) e^{i\bar{k}_n^i y} \tag{2.2}$$

where the last summation is performed over the set of the evanescent modes $\bar{\psi}_n^i$ which solve the Schrödinger equation (1.2) with complex wave-numbers $\bar{k}_n^i$. We stress that in principle this last contribution should include infinitely many terms since infinite are the evanescent solutions of Eq.(1.4) associated with a given selected energy eigenvalue E^i. However, to make the problem treatable numerically we limit the number Q_i to only include those evanescent modes $\bar{\psi}_n^i$ whose $\bar{k}_n$ lies within a finite radius from the origin of the complex plane (see Fig.2.2).[2]

Let us consider first the case where there is the same filling factor in the two regions (i.e. $P_{\mathrm{I}} = P_{\mathrm{II}} = P$), and focus on the scattering process associated with right-moving electrons coming from the left lead with given mode number $j \in \{1, 2, \cdots, P\}$. The scattering amplitudes t_{nj} (r_{nj}) that couple such incoming mode with the transmitted (reflected) modes in the channel n can then be directly identified with the coefficients a_n^{II} (b_n^I) obtained from Eq.(2.2) while imposing the matching conditions of Eq.(2.1) as long as we multiply these coefficients by the inverse square root of the Fermi velocity (see Eq.(1.24)) in order to ensure the unitarity of the final **S** matrix.

The number of unknowns is given by $2(P + Q)$, since, although not entering in the scattering matrix, the coefficients relative to evanescent waves (c_n^I and c_n^{II}) must be found. The $2(P + Q)$ equations needed to determine them can be obtained by expanding the functions $\psi_n^{Ri}(x)$, $\psi_n^{Li}(x)$ and $\bar{\psi}_n^i(x)$ in the first $N/2 = (P + Q)$ Fourier

[1] Notice that since E^i differs in the two regions, P_{I} and P_{II} need not to coincide (see Section 2.2.2).

[2] the exact number being determined under the condition that the final result of any computation does not vary significantly if extra evanescent modes are added in the expansion – for our simulations described in Section 2.1.1 this corresponds to $Q_i \simeq 20$.

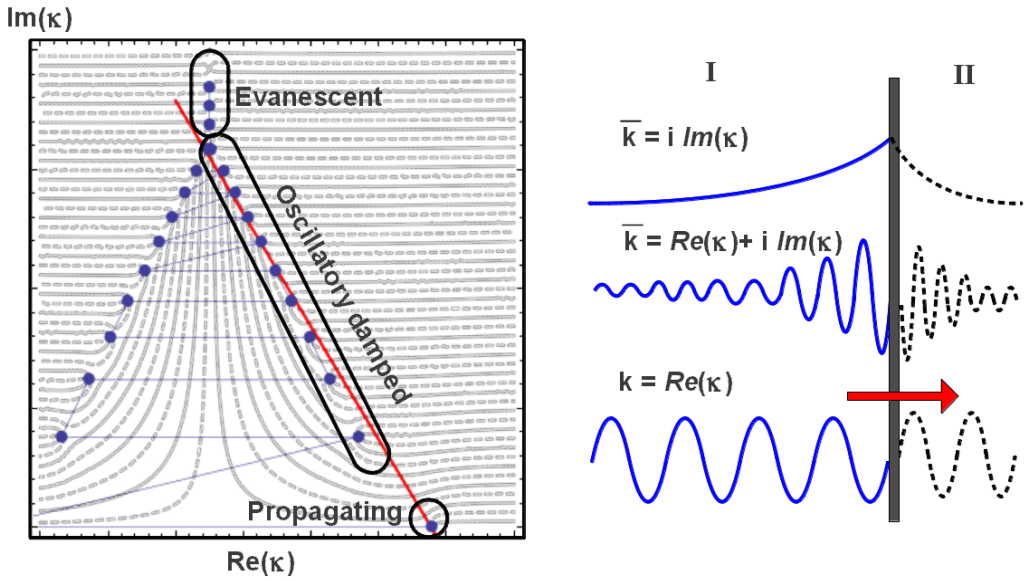

Figure 2.2: **Left panel**: Illustration of the numerical procedure for determination and development of propagating and evanescent solutions of the SEQ . The code solves the transcendental equation (1.5) which results from imposing the boundary conditions $\psi(x=0) = \psi(x=L) = 0$. This find the solutions of the SEQ in the complex k-plane (continuous and dashed lines represent respectively the real and imaginary part of the parabolic cylinder functions in Eq.(1.5)). The ordering of complex wave-numbers on the scattering matrices is highlighted by blue lines and the red line represent the ansatz point as initial condition for the numerical search of solution of the equation. **Right panel**: pictorial view of the evanescent (imaginary and oscillatory damped), and propagating scattering states which have to be matched in order to find the proper steady state solution.

modes $\varphi_n = \sqrt{\frac{1}{L}} \sin\left(\frac{2n\pi x}{L}\right)$ as follows:

$$\psi_n^{Ri}(x) = \sum_{j=1}^{N/2} \alpha_{nj}^i \sin\left(\frac{2j\pi x}{L}\right) \quad \text{for } 1 \le n \le P\,, \tag{2.3}$$

$$\psi_n^{Li}(x) = \sum_{j=1}^{N/2} \beta_{nj}^i \sin\left(\frac{2j\pi x}{L}\right) \quad \text{for } 1 \le n \le P\,, \tag{2.4}$$

$$\bar{\psi}_n^i(x) = \sum_{j=1}^{N/2} \gamma_{nj}^i \sin\left(\frac{2j\pi x}{L}\right) \quad \text{for } 1 \le n \le Q\,, \tag{2.5}$$

the coefficients α_{nj}^i corresponding to right-going modes, β_{nj}^i to left-going modes, and γ_{nj}^i to evanescent modes. At the end of the simulation we check that the number of Fourier Modes used in the expansion is sufficient to properly describe all propagating, oscillatory damped and evanescent modes that contribute appreciably to the scattering matrix. In Figure 2.3 we show some Fourier expansions of edge modes at $\nu = 4$. The figure shows that for the simulated Hall bar (whose width is about $10 l_B$) having more than 10 modes in the expansion is already sufficient for properly characterize all evanescent states with a non-zero real part of k. Purely imaginary[3] evanescent states

[3]To be more precise, the states which do not show any oscillatory behavior are 'purely imaginary'

are not supposed to be important, since they do not exist in the limit of a large Hall bar. Our results for a finite-width Hall bar are relevant for the semi-infinite case, since the contribution of the purely imaginary evanescent modes which are considered (which are only partially well described as shown in Fig.2.3), is neglectable for the calculation of the resulting scattering matrix.

By multiplying by φ_l and integrating over x, Equations (2.3)-(2.5) can be recasted in the following $N \times N$ matrix equation

$$\begin{pmatrix} \sum_n^P \left(a_n^I \vec{\alpha}_{nl}^I - a_n^{II} \vec{\alpha}_{nl}^{II}\right) \\ \sum_n^P \left(k_n^I a_n^I \vec{\alpha^I}_{nl} - k_n^{II} a_n^{II} \vec{\alpha}_{nl}^{II}\right) \end{pmatrix} = \begin{pmatrix} \mathcal{B}^{II} & -\mathcal{B}^I & \mathcal{C}^{II} & -\mathcal{C}^I \\ \tilde{\mathcal{B}}^{II} & -\tilde{\mathcal{B}}^I & \tilde{\mathcal{C}}^{II} & -\tilde{\mathcal{C}}^I \end{pmatrix} \begin{pmatrix} \vec{b}_n^{II} \\ \vec{b}_n^I \\ \vec{c}_m^I \\ \vec{c}_m^{II} \end{pmatrix} \tag{2.6}$$

where for $i = I, II$, $\vec{\alpha}_{nl}^i \equiv (\alpha_{n1}^i, \alpha_{n2}^i, \ldots, \alpha_{nN}^i)^T$, $\vec{b}_n^i \equiv (b_1^i, b_2^i, \ldots, b_P^i)$, $\vec{c}_n^i \equiv (c_1^i, c_2^i, \ldots, c_Q^i)$, and $\mathcal{B}^i$, $\mathcal{G}^i$ denote the matrices containing the Fourier coefficients, namely $(\mathcal{B}^i)_{nl} \equiv \beta_{nl}^i$ and $(\mathcal{C}^i)_{nl} \equiv \gamma_{nl}^i$ respectively, while $\tilde{\mathcal{B}}^i$ and $\tilde{\mathcal{C}}^i$ denote the matrices of elements $(\tilde{\mathcal{B}}^i)_{nl} \equiv k_n^i \beta_{nl}^i$ and $(\tilde{\mathcal{C}}^i)_{nl} \equiv k_n^i \gamma_{nl}^i$.

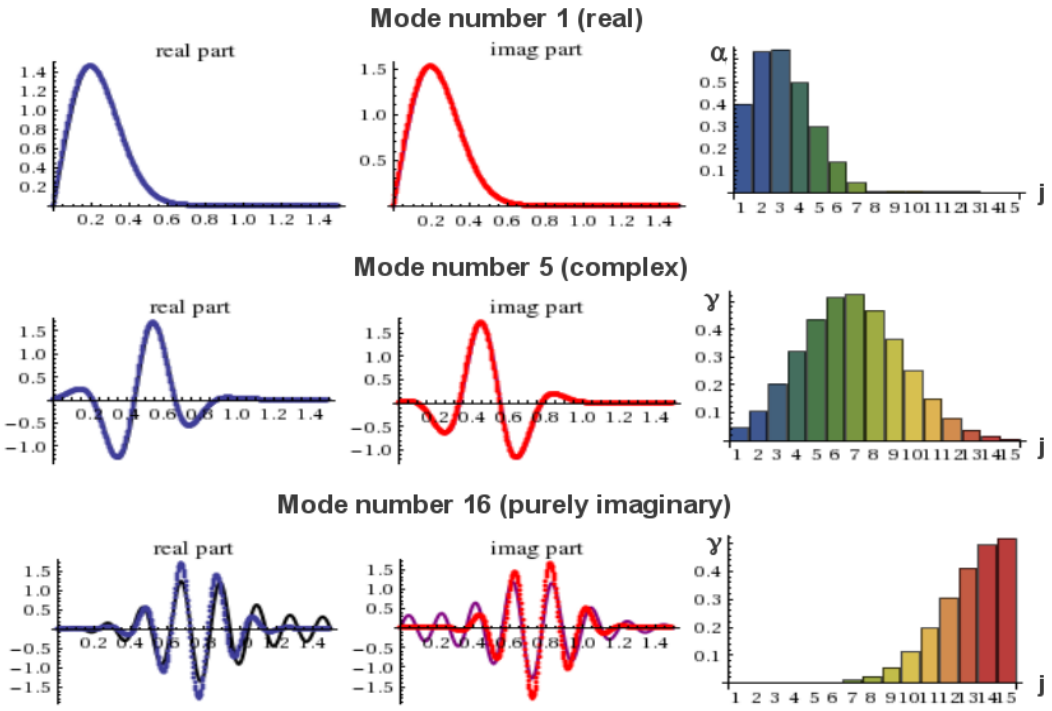

Figure 2.3: Illustration of the Fourier-modes expansion of the propagating (upper set of panels) and evanescent modes (middle and bottom panels). The Fourier coefficients for the representation of the localized modes are represented in the Histogram at the right side of each panel (See Eqs.2.3-2.5). For the purely imaginary mode (numbered 16th in the example, with reference to the ordering pictured in Fig.2.2) the number of considered Fourier modes is not sufficient to properly represent the real and imaginary part of the wavefunction (see text).

This linear problem can be solved numerically so that the resulting coefficients allow

only in the reference frame where the hard-wall is located at $x = \pm L/2$. In Figure 2.2, these states are shifted along one line parallel to the imaginary axis.

a full reconstruction of the wave-function in all regions through Eq. (2.2). The same analysis holds when $P_{\rm I} \neq P_{\rm II}$ with the only important requirement that the linear system in Eq.(2.6) is determined, i.e. that $P_{\rm I} + Q_{\rm I} \equiv P_{\rm II} + Q_{\rm II}$. An example of such a configuration is presented in section 2.2.2 where we will assume $P_{\rm I} = 1$ and $P_{\rm II} = 2$.

2.1.1 The single non-adiabatic potential step

In this section we shall discuss the results obtained for the scattering amplitudes in the case of a Hall bar with either one or two open edge channels (cyclotron resolved). The simple version of the MM method as discussed in the previous section implies that there exist two regions in the scattering zones where we can solve the SEQ for the propagating and evanescent states. This is the case for a scatterer that consists of a sharp potential step, so that the transported electrons experience a sudden jump between regions where the SEQ looks the same, but with two different effective energies: $E^{\rm I} = E$ and $E^{\rm II} = E + \Delta E$ (See Fig.(1.4), bottom panel). This non-adiabatic potential variation is the simplest prototype of a "mixer", as it breaks the translational invariance of the SEQ with minimal impact on the nature and the shape of the propagating state (as long as ΔE is sufficiently small), so its analysis is important for fundamental reasons. However, the implementation of such local, short-scale potential variations is, in principle, within the experimental reach of cutting-edge technology, for example, through: i) precise impurity implantation by means of focused ion beam [36, 37, 39], AFM induced oxidation [38], cleaved-edge overgrown technique[40, 41].

Two regions with equal filling factor Let us now consider the case of two edge channels ($P_I = P_{II} = 2$) on each side of the step potential, aiming at evaluating the channel mixing probabilities $|t_{12}|^2$ and $|t_{21}|^2$ representing the probability for transmission from inner (2) to outer (1) ES and vice-versa, respectively. By setting $L = 6.7 l_B$, we make sure that the reflection probabilities are negligible. More precisely, fixing the energy of the incoming electrons at $1.7\hbar\omega_c$ above the first LL, we found that the only non-vanishing, though very small, reflection coefficient is $|r_{22}|^2 \sim 10^{-3}$. In Fig.2.4 the channel mixing probability $|t_{12}|^2$ is plotted as a function of the potential barrier height ΔE in units of $\hbar\omega_c$: $|t_{12}|^2$ increases monotonically with increasing ΔE, taking a value of the order of few percent only for a step potential as high as $0.7\hbar\omega_c$. If there is non-zero reflection probability, $|t_{21}|^2$ slightly differs from $|t_{12}|^2$ but for a sufficiently large channel the effect is not appreciable.

In the limit of small step height $\Delta E \ll \hbar\omega_c$, an analytical estimation of t_{12} is possible by means of perturbation theory. For instance assuming a potential which represents a sharp jump followed by an exponential smooth tail, $U(y) = -\Delta E \Theta(y)\, e^{-y/\mathcal{L}}$, by taking the limit $\mathcal{L} \longrightarrow \infty$ one can verify that, up to a phase factor, the channel mixing amplitude t_{12} can be approximated (Born approximation, valid at first order in ΔE [16]) to:

$$t_{12} = L \frac{\langle \Psi^I_{k_1}(E^I) \,|U(y)|\, \Psi^{II}_{k_2}(E^I)\rangle}{i\hbar\sqrt{v_F(k_1) v_F(k_2)}} = \frac{1}{\sqrt{\mathcal{N}_{12}}} \frac{\Delta E}{k_1^I - k_2^{II}} \int dx\; \psi^I_{k_1}(x)\, \psi^{*II}_{k_2}(x)\;, \qquad (2.7)$$

where $\mathcal{N}_{12} = \left| \int_{-L/2}^{L/2} dx |\psi^I_{k_1}(x)|^2 (\beta x + k_1^I) \times \int_{-L/2}^{L/2} dx' |\psi^{II}_{k_2}(x')|^2 (\beta x' + k_2^{II}) \right|$ is the normalization factor that ensures the unitarity of the scattering matrix. We checked that the curve reported in Fig.(2.4) is fitted by the Eq.2.7 very close to the origin, but a full numerical calculation is necessary to capture the nonlinear behavior. We also note that the mixing does also weakly depend on the reference energy E as well, but this

dependence is negligible as long as it lies in-between the Landau level energies, so that the edge dispersion remains linear.

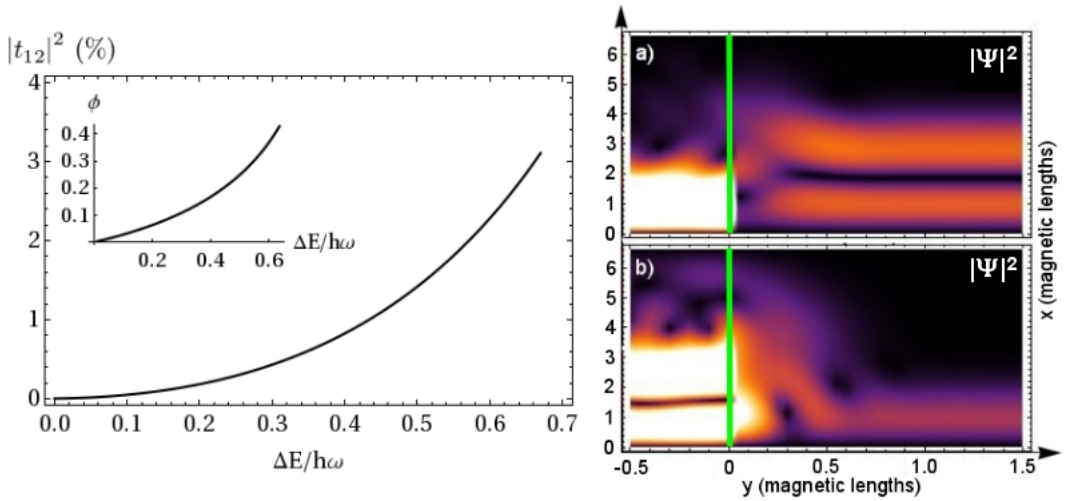

Figure 2.4: **Left panel**: $|t_{12}|^2$ percentage, for the case $P_I = P_{II} = 2$, as a function of the height of the potential step ΔE. In the inset: scattering phase shift as a function of the potential step height for a single edge channel. **Right panel**: Charge density $|\Psi(x, y)|^2$ of the scattering solution to the step problem is plotted in the case of a sharp step potential with $P_I = 2$ where electrons are injected from region I in channel 1 (**a**) and channel 2 (**b**). Vertical lines represent the position of the potential step ($y = 0$), so that region I is on the left hand side and region II is on the right hand side. Bright areas in region I correspond to the high probability density of incoming electrons exhibiting, in the transverse x-direction, one lobe, for injection from channel 1, and two lobes, for injection from channel 2. In region II the probability density relative only to the transmitted electronic wave functions with channel mixing is plotted, i.e. the contribution to the wave functions due to the amplitudes t_{11} (for panel (**a**)) and t_{22} (for panel (**b**)) has been subtracted for clarity.

As a check we also consider the case of a single edge channel ($P_I = P_{II} = 1$). Here we have verified that the reflection probability $|r_{11}|^2$ is completely negligible, within the numerical accuracy, as long as L is greater than 6.5 l_B. Current conservation therefore implies that one can write $t_{11} = e^{-i\phi}$: the incoming electron acquires a phase due to the non-adiabatic step.

In Fig.(2.4) we show the phase ϕ in radians as a function of the potential step height ΔE in units of $\hbar\omega_c$. The energy of the impinging electrons E is set to $0.8\hbar\omega_c$ (i.e. $0.3\hbar\omega_c$ above the first LL). The phase shift ϕ increases monotonically nearly reaching the value $\pi/8$ for the highest step considered. In the same figure we plot the electron probability density $|\Psi(x, y)|^2$ in the case of two edge channels in region II ($P_{II} = 2$), where we highlight the density relative to the crossed transmissions t_{12} and t_{21} (the contribution of the evanescent modes allows the non-trivial matching which is apparent right after the potential step).

2.2 Strategies of Coherent-Mixing of Edge Channels at Equilibrium

The conclusion of the previous numerical calculation is that a single very sharp potential variation does not mix appreciably the channel nor it introduces a substantial phase shift on a single channel, as long as it is localized and of weak intensity compared to the Landau gap. As a natural extension to the previous study we consider what happens when we increase the number of mixers and/or we increase the intensity of the mixing potential.

2.2.1 Several Potential Steps

A possible strategy to achieve a channel mixing of the order of 50% is to place several potential steps in series. This is in principle possible by using nanopatterning techniques to realize a sequence of top gates following the non-adiabatic steps. Assuming a typical magnetic lengths of about 10 nm, a few tens of potential steps could be obtained over a length of some microns.

A simple evaluation of the channel-mixing transmission probability can be done by assuming that, after the sharp step, the potential smoothly goes to zero (see Fig.2.5). In doing so, after the mixing occurring at a potential step, the electrons in the two channels freely propagate along the potential tail to the next potential step accumulating a relative phase. Once all reflections due to the large separations between steps are suppressed, the total transmission matrix $t(M)$ of a series of M steps is (up to a global phase) the product of the transmission matrices of the individual steps (of height ΔE_i) plus tails, which include the phase ϕ_i accumulated while propagating past the step i:

$$t(M) = \prod_{i=1}^{M} \begin{pmatrix} t_{11}(\Delta E_i)\, e^{i\phi_i} & t_{12}(\Delta E_i)\, e^{-i\phi_i} \\ t_{21}(\Delta E_i)\, e^{i\phi_i} & t_{22}(\Delta E_i)\, e^{-i\phi_i} \end{pmatrix} . \tag{2.8}$$

The phase ϕ_i depends both on the details of the adiabatic tail of the step and on the distance x_i between the steps. It turns out that even a few steps can increase dramatically the channel mixing probability $|t_{12}(M)|^2$ and that the latter, due to interference effects, very much depends on the set of phases $\{\phi_i\}_{i=1,M}$. For example, 50% mixing can be achieved with four potential steps of height $\Delta E \simeq 0.72\hbar\omega_c$, or with 10 potential steps of height $\Delta E \simeq 0.4\hbar\omega_c$. The control of the phases ϕ_i, in order to tune the channel mixing, can be obtained by placing lateral finger gates in the region of the tail of the potentials. The role of these additional gates is to modify the lateral confinement potential in such a way to alter the distance x_i traveled by the electrons propagating between two steps. Indeed, due to the large difference $(k_1^i - k_2^i)$, even a small variation of x_i (of the order of 1/10 of the magnetic length) results in a very significant variation of the phase difference between the modes $\phi_i = (k_1^i - k_2^i)x_i \simeq 1$. In Fig.2.5 the maximum (over ϕ_i) channel mixing probability $|t_{12}(M)|^2$ (obtained numerically by maximizing in sequence each phase, due to the independent character of the series of steps) is plotted as a function of the number of potential steps for three different values of step height, namely $0.2\hbar\omega_c$, $0.4\hbar\omega_c$ and $0.72\hbar\omega_c$.

It is interesting to consider the situation where the phase differences ϕ_i are not controlled and take random values. In this case for every M one can average the channel mixing probability over a given number of configurations of the set $\{\phi_i\}_{i=1,M}$, with $\phi_i \in [0, 2\pi]$. We plotted $|t_{12}(M)|^2$ averaged over 2000 configurations[4] for different

[4]Each configuration consists of a random set of phases. While the convergence towards the average mixing (shown in Fig. 2.5) is achieved reliably for a few hundreds of averages, the error bars (not shown in the figure) depend on the number of averages.

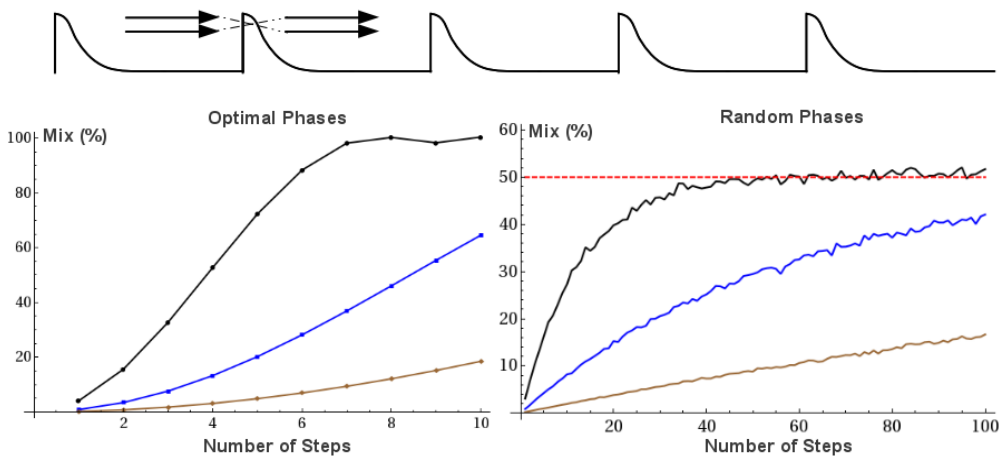

Figure 2.5: **Top panel**: schematic view of the sequential placement of several non-adiabatic steps, which acts independently. **Bottom panel**: $|t_{12}|^2$ as a function of the number of scatterers M for different potential heights (blue: $0.72\hbar\omega_c$, purple: $0.4\hbar\omega_c$, brown: $0.2\hbar\omega_c$). **Bottom left**: assuming that each individual phase-adjusting gate is tuned to maximize the mixing. **Bottom right**: assuming random phases ϕ_i accumulated between the steps. Numerical error on unitarity of the S-matrix might induce variations of the order of 1%. The curves represent the average over 2000 random configurations (phases uniformly distributed from 0 to 2π).

values of step height. We notice that equilibration (50% mixing) is reached for a large enough M.

2.2.2 High-Potential Steps

An alternative possible strategy for obtaining a significant channel mixing consists in fixing $P_I = 1$ and setting ΔE large enough so that in region II two edge channels are open ($P_{II} = 2$). In this case the incoming electrons will be split between the two edge channels available in region II, according to the values of the transmission amplitudes t_{21} and t_{11} (see Fig.2.6).

In order to qualitatively characterize the effect, Fig.2.6 shows the probability $|t_{21}|^2$ for some indicative values of incident energy E spread all over the energy gap, and as a function of the energy step ΔE. For all the curves channel mixing exceeds 15 %, reaching about 30 % for $E = 1.6\hbar\omega_c$ and $E = 1.7\hbar\omega_c$.
We emphasize that this setup might be used to create the initial coherent superposition of wave-packet on the two edge channels which are needed for the interferometer of Ref. [26], but it is not scalable in the sense that we cannot apply two of these device in sequence as for the strategy described in the previous Subsection.

In Section 3.1.1 we will use this simple device as a model to test a numerical technique and we will compute the charge density relative to the produced mixing by a strong non-adiabatic potential step.

2.2.3 Electronic Periodic Poling

In Section 2.2.1 we observed how dramatic the effect of being able of individually control the phase differences that acquire the electrons while moving along the edge channels can be. However, it would be technologically challenging to introduce several phase adjusters in-between the potential steps. If each scatterer in the strategy discussed

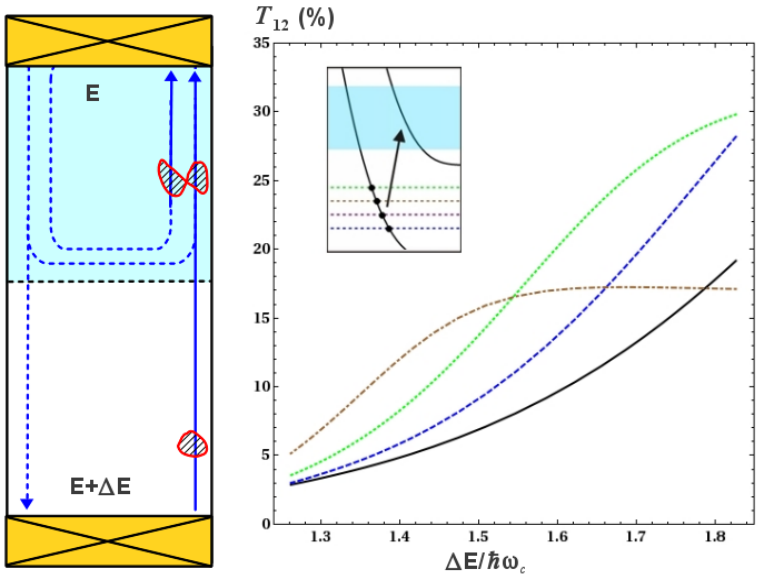

Figure 2.6: **Left panel**: pictorial view of the edge channels for a device whose scattering regions lie at different filling factors. From the transport point of view, flying electrons from the bottom contact see the opening of a new channel after the mixing step. **Right panel**: $|t_{12}|^2$ in the case where $P_I = 1$ and $P_{II} = 2$ for four different values of energy of the incoming electrons (pictured as dashed lines in the inset) as a function of the potential step height ΔE, which spans the energies indicated on the shaded area on the inset.

in Section 2.2.1 is independent, this would result in a quite long and complex device, whose very presence would introduce several external noise sources that can spoil the coherence of the charge transfer.

In this section we go beyond the requirement of the independent potential step by examining the effect of a series of "closely-spaced" potential steps. Numerically we would need to concatenate *scattering matrices* including also counter-propagating and evanescent states, so the amplification effect due to the increase in number of scatterers would not be straightforward to analyze, let alone the impossibility to individually address independently the phase of the states living in the channels, when the potential jumps are closely-packed.

While in the next chapter we will develop numerical methods to deal with the problem in its full generality, it is however tempting to exploit the regularity of the evolution of the eigenmodes of the system when the non-adiabatic potential variations are equally-spaced, as a method of "phase control". In other words, we can formally analyze the effect of a *periodic, non-adiabatic* potential variation along the propagation direction of two edge channels. The question we address is the following: is there an optimal spatial periodicity for which a set of N scattering centers guarantee a large mixing (as it is the case for the effect described in Fig.2.5)?

Following the Born approximation as in Eq.(2.7), we can evaluate the perturbative effect of $U(y) = \Delta E \cos(2\pi y/\lambda)\Theta(y)\Theta(y - 2\Delta Y)$ for small ΔE, as a function of the

periodicity λ and of the total length of the periodic modulation L

$$t_{12}(\lambda) \simeq \frac{\mathcal{M}_{12}}{i\hbar\sqrt{v_F(k_1)v_F(k_2)}}[e^{i\Delta k\Delta Y}\frac{\sin[(\Delta k+\frac{2\pi}{\lambda})\Delta Y]}{(\Delta k+\frac{2\pi}{\lambda})} + e^{-i\Delta k\Delta Y}\frac{\sin[(\Delta k-\frac{2\pi}{\lambda})\Delta Y]}{(\Delta k-\frac{2\pi}{\lambda})}] , \tag{2.9}$$

where $\mathcal{M}_{12}$ represents the "overlap integral" $\mathcal{M}_{12} = \Delta E \int dx \psi_{k_1}(x)\psi^*_{k_1}(x)$.

The function $t_{12}(\lambda)$ presents a pronounced peak for[5]:

$$\lambda^\star = \frac{2\pi}{\Delta k} \tag{2.10}$$

The intensity of the peaks is proportional to ΔE, and depend linearly on the length of the modulation L, however it must be recalled that Eq.(2.9) is valid as long as the final result is $\ll 1$. The *resonant condition* defined by the periodicity of the modulation as in Eq.(2.10) is achievable with current nanotechnology only for $\Delta k \lesssim 10\ nm^{-1}$, since a modulation whose period in smaller than some tens of nanometers would not be possible in practice. Bearing in mind the considerations in sections 1.2.2-1.3, we can then conclude that coupling cyclotron resolved edge channels would not be possible, while $\lambda^\star$ for spin-resolved ES is of the order of some hundreds of nanometers, well within the fabrication capabilities of the laboratories.

In order to induce charge transfer between spin-resolved ES, electric modulation would not be sufficient, as $U(y)$ does not mix orthogonal spin-states. We are naturally lead to exploit local modulation implemented by in-plane magnetic fields, whose formal action of the spin Hilbert space is defined by Eq.(1.13). By noting $\vec{B}_\parallel(x,y) = B_x(x,y)\hat{x} + B_y(x,y)\hat{y} = \Theta(y)\Theta(y-L)[B_x(x)\hat{x} + B_y(x)\hat{y}]\cos(2\pi y/\lambda)$, and neglecting the anti-resonant term proportional to $e^{i\Delta k\Delta Y}$, first-order perturbation theory gives now:

$$|t_{\uparrow\downarrow}(\lambda)|^2 \simeq \frac{e^2}{4m^2}\frac{(\mathcal{M}^{B_x}_{\uparrow\downarrow} + i\mathcal{M}^{B_y}_{\uparrow\downarrow})^2}{v_F(k_1)v_F(k_2)} \times \frac{\sin^2[(\Delta k-\frac{2\pi}{\lambda})\Delta Y]}{(\Delta k-\frac{2\pi}{\lambda})^2} , \tag{2.11}$$

where $\mathcal{M}^{B_i}_{\uparrow\downarrow} = \int dx \psi_{k\uparrow}(x)\psi^*_{k\downarrow}(x)B_i(x)$. The striking observation is that the value of $t_{\uparrow\downarrow}(\lambda)$ at resonance is proportional to ΔY, so it can become very large if the modulation is extended over a long region. Of course if $t_{\uparrow\downarrow}$ is not a small number, first order perturbation theory is no longer justified, but this divergence of the approximate result hints at the existence of a coherent amplification effect.

In section 3.3 we will indeed confirm with numerical techniques that this approximate result is indeed the foundation of a solid physical effect[6] which survives in the full non-perturbative solution, and that can practically used to achieve mixing among co-propagating edge channels.

[5] in principle, there is a resonance also for $\lambda^\star = -\frac{2\pi}{\Delta k}$, but in the we assume $k_1 > k_2$ and λ of course positive!

[6] We note that our approach is based on the same physical mechanism that drives the periodic poling technique adopted in optics to enforce quasi-phase-matching conditions between optical beams of orthogonal polarization which are co-propagating in a nonlinear crystal [42]. This scheme is also related to the superlattice-modulation technique [43, 44, 45] used to couple counter-propagating spin-degenerate modes via modulation of the electric potential in narrow channels and to the modification of electron transport in the presence of magnetic superlattices.

3 Numerical Simulations and Modeling of Coherent Transport Experiments

In this chapter we introduce the numerical technique of Recursive Green's Functions and we present our simulations of two experiments which test coherent mixing among co-propagating edge states. One study concerns a Scanning Gate Microscopy experiment aiming to characterize the channel equilibration due to disorder between cyclotron-resolved edge states. The second numerical work features the simulation of an measurement of mixing through the periodic poling technique implemented by in-plane magnetic fields acting on spin-resolved edge channels.

3.1 Numerical Methods on Tight-Binding Models

Following the finite-element discretization prescriptions of Sec. 1.2.1, the approximate version of the SEQ for a 2DEG at zero magnetic field can be written as [1]

$$\begin{aligned} \epsilon_F \psi_m^n &= -a^{-2}t(\psi_{n+1}^m + \psi_{n-1}^m) + \\ &\quad -a^{-2}t\left(\psi_n^{m+1} + \psi_n^{m-1}\right) + \\ &\quad +(V_{mn} + 4a^{-2}t)\psi_m^n \,, \end{aligned} \tag{3.1}$$

where $a = x_{n+1} - x_n = y_{m+1} - y_m$ is the discretization step, $\psi_n^m = \Psi(x_n, y_m)$ are the local values of the wavefunction on the introduced square lattice, V_{mn} is the local value of the external potential at (x_n, y_m) and $t = \hbar^2/2m$. Equation (3.1) is the an eigenvalue equation for a Tight-Binding Hamiltonian

$$H = \sum_{<ij>} \mathcal{A}_{ij} \left|\psi(r_i)\right\rangle \left\langle\psi(r_j)\right| \,, \tag{3.2}$$

where $r_{i,j}$ are coordinate vectors, and the sum runs over first-neighbors of a 2D-lattice and $|\psi(r_i)\rangle$ are "localized orbital" states. This correspondence is valid assuming that the *on-site matrix elements* $\mathcal{A}_{ii}$ are taken to be $4t+V_{ii}$ and the *hopping matrix elements* are $\mathcal{A}_{<ij>} = t$.

Magnetic Field and Spin-dependent Hamiltonian Adding the effect of a magnetic field on a tight-binding system is possible simply by modifying the parameters of the Hamiltonian (3.2). The appropriate way to discretize the minimal coupling substitution prescription ($\vec{p} \to \vec{p} - e\vec{A}$, where $\vec{A}$ is the magnetic vector potential, and $\vec{p}$ the momentum operator) goes under the name of *Peierls Substitution*, and consists of the transformation of the hopping elements

$$t \longrightarrow t e^{-i\frac{e}{\hbar}\int_{r_1}^{r_2}\vec{A}\cdot dl} \,. \tag{3.3}$$

The integral is meant to be made along a line connecting two lattice sites $r_1 = (x, y, z)$ and $r_2 = (x', y', z')$. [1] We note that if the lattice is strictly 2-dimensional, only the

[1] In the limit $r_1 - r_2 = a \ll l_B$, adding these phase factors to the hopping elements is equivalent to stating that the amplitudes for propagation along two different trajectories between two points in space differ by the Aharonov-Bohm phase [46].

magnetic field component B_z will enter in the kinetic Hamiltonian. For homogeneous B_z in Landau gauge the Peierls substitution takes the convenient form

$$t^B_{nm} = t_{nm} e^{-i\frac{e}{\hbar}Ba^2 m} \ . \tag{3.4}$$

The spin-degree of freedom is easily included in the discretized Hamiltonian by doubling the number of states, which in the position basis means to duplicate the whole device by creating two sublattices[2]. Introducing a local magnetic field in an arbitrary direction is now possible through the coupling of the Zeeman Hamiltonian ΔH defined in Eq.(1.13), which in discretized notation is translated into the terms

$$\begin{aligned} \Delta H_{nm} &= g\mu(B_x)_{nm}(\left|\psi^m_{\uparrow n}\right\rangle\left\langle\psi^m_{\downarrow n}\right| + \left|\psi^m_{\downarrow n}\right\rangle\left\langle\psi^m_{\uparrow n}\right|) \\ &+ ig\mu(B_y)_{nm}(\left|\psi^m_{\uparrow n}\right\rangle\left\langle\psi^m_{\downarrow n}\right| - \left|\psi^m_{\downarrow n}\right\rangle\left\langle\psi^m_{\uparrow n}\right|) \\ &+ g\mu(B_z)_{nm}(\left|\psi^m_{\uparrow n}\right\rangle\left\langle\psi^m_{\uparrow n}\right| - \left|\psi^m_{\downarrow n}\right\rangle\left\langle\psi^m_{\downarrow n}\right|) \ . \end{aligned} \tag{3.5}$$

The B_z-part is easily accounted by a Zeeman-energy shift in each on-site element, and does not couple the two sublattices. The in-plane fields B_x and B_y are instead hopping elements between sublattices (see Fig.3.1) *at the same spatial site* (n,m).

To summarize, a finite-size quantum Hall bar can be numerically modeled setting up a lattice on which a tight-binding Hamiltonian is defined appropriately. In the following sections we will formalize the procedures for computing transport observables.

3.1.1 Recursive Green's Functions Technique

The fact that a tight-binding Hamiltonian can be written in block-tridiagonal form can be exploited by using a numerical technique, the *recursive Green's functions* (RGF) method,[3] for calculations of local and non-local observables.

The most common way to implement the efficient calculation starts with the definition of the numerical retarded Green's function of the system (at energy ϵ, and expressed on a basis of ordered lattice sites i, j)

$$G_{ij}(\epsilon) \equiv [(\epsilon - H)^{-1}]_{ij} \ . \tag{3.6}$$

Depending on the specific algorithm, from the Hamiltonian matrix H of the system we extract one "basic" H_0 , which is the Hamiltonian of a simple subsystem whose Green's function can be computed easily

$$g^0_{ij} = (\epsilon - H_0)^{-1}_{ij} \ , \tag{3.7}$$

plus the hopping Hamiltonian that couples this subsystem with the rest of the discretized system. This way we can show that Eqs.(3.6)-(3.7) obey the *Dyson equation[68]*

$$G_{ij} = g^0_{ij} + \sum_{mn} g^0_{im} t_{mn} G_{nj} \ , \tag{3.8}$$

which makes clear that if the hopping elements t connects only first neighbors in the discretized lattice, we can implement this extension of the system one step per time (recursively)[4]. This means that we can consider at each cycle only two sub-systems:

[2] With the correct re-ordering, the complete matrix has now a block-diagonal form

[3] This computational scheme sometimes have different name in the literature (the *decimation/renormalization* procedure, the *transfer matrix* approach...).

[4] We will denote the hopping coefficients with low indices as in t_{mn} when we want to refer to single matrix elements, coupling two lattice sites. We use superscripts as in t^{n_1,n_2} when we want to indicate the hopping matrix that connects two subsystems.

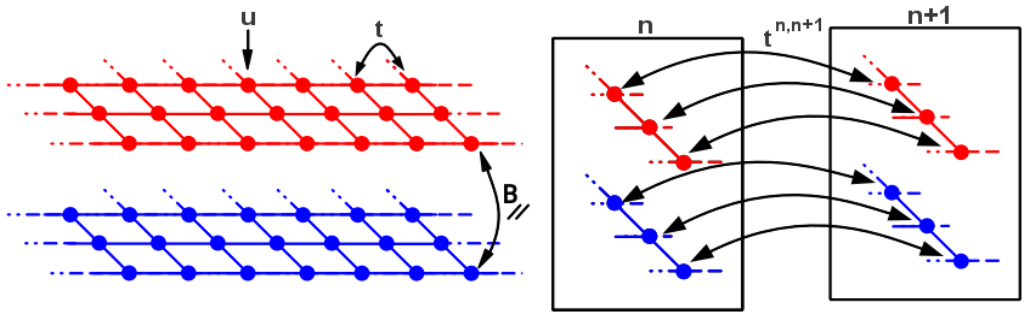

Figure 3.1: Pictorial representation of a tight-binding Hamiltonian. **Left panel**: spin sublattice (red,blue) where on-site energies (u), hopping energies (t) and in-plane Zeeman coupling $B_{\parallel}$ are highlighted **Right panel**: symbolic structure of the coupling between Hamiltonian "slices" through the hopping matrices $t^{n,n+1}$

the compound system from step 1 up to step $n-1$, and the subsystem n which has to be coupled by means of Eq.(3.8).

For clarity in this Section we will consider the standard implementation of the RGF, where subsystems are "slices" of a rectangular two-terminal (L/R) device (see Fig.3.1)[5].

By denoting as $G^{S(n)}_{m,l}$ the Green's function from slice m to slice l, computed considering the system from the first slice up to slice $n > m, l$, the general recursion relations are

$$\begin{aligned} G^{S(n)}_{n,n} &= [\epsilon - H_n - t^{n,n-1} G^{(n-1)}_{n-1,n-1} t^{n,n-1}]^{-1} \ , \\ G^{S(n)}_{m,l} &= G^{S(n-1)}_{m,l} + G^{S(n-1)}_{m,l} t^{n-1,n} G^{S(n)}_{n,n} t^{n,n-1} G^{S(n-1)}_{n-1,l} \ , \\ G^{S(n)}_{m,n} &= G^{S(n-1)}_{m,n-1} t^{n-1,n} G^{S(n)}_{n,n} \ . \end{aligned} \tag{3.9}$$

This procedure can be done in a number of ways, all equivalents [57, 1], depending on which symmetries of the system we want to exploit to make the code more efficient. As pictured in Fig.3.1, the standard approach for two-terminal systems is to consider the Hamiltonian divided in slices of the same number of sites, and connect the slices by some hopping matrices (which also contains the Peierls phases Eq.(3.4) and transverse magnetic couplings Eq.(3.5)).

These cycle (3.9), which can be computed forward ($n \to n+1$) or backward ($n \to n-1$) allow the computation of the Green's function matrices between two arbitrary points in the lattice, $r_1 = (n_1, m_1)$ and $r_2 = (n_2, m_2)$: $G_{r_1 r_2} = [G^{S(N)}_{m_1 m_2}]_{n_1 n_2}$ where $N > n_1, n_2$ represents the last slice of the system.

The experiments that we simulate measure currents in Hall bars which will be flowing between electrodes, so the finite-size simulated region can be interpreted as a scattering zone for well defined source and drains, as in the Scattering approach for transport (Section 1.3.1). This means that the simulated Hall bar needs to be attached to *lead regions* which are defined as semi-infinite translation invariant systems, maintained in a non-equilibrium condition so that steady-state transport is well defined. The value of the Green's function matrix of these homogeneous semi-infinite regions (denoted as $\mathbb{G}^{lead}$) on the boundary sites that are connected to the scattering inhomogeneous region can be computed exactly by analytical or numerical methods [50].

[5] We note that generalization of the procedure to multi-terminal systems in arbitrary planar geometry is possible while maintaining the Landau Gauge everywhere.

Current and Charge Density Observables As it will be further detailed in section 4.2.3, the scattering formalism can be linked to the Green's functions derived from a microscopic Hamiltonian.

For non-interacting systems, there exist indeed *Fisher-Lee* relations [48] that link the total transmission coefficient[6] between two leads L and R (T_{RL}) to the retarded Green's functions defined in Eq.(3.6):

$$T_{LR}(\epsilon) = \sum_{r_L, r'_L} \sum_{r_R, r'_R} \Gamma^L_{r_L, r'_L} \cdot G_{r_L r_R}(\epsilon) \cdot \Gamma^R_{r_R, r'_R} \cdot G^{\dagger}_{r'_R r'_L}(\epsilon) \ , \tag{3.10}$$

where r_L and r_R (as r'_L and r'_R) are lattice sites connected respectively to the leads L,R by means of the lead-system matrices $\Gamma^L_{r_L, r'_L}$ and $\Gamma^R_{r_R, r'_R}$ (see Fig.3.2). These matrices Γ can be computed by considering the iteration cycles as in Eqs.(3.9) where now the system Green's functions G are connected to the surface of the semi-infinite lead. Indeed it can be shown that the following relation for the lead-system matrices (see Fig.3.2) holds [16]

$$\Gamma^j_{r_j r'_j} = -2\mathrm{Im}[\sum_{x_j} \sum_{x'_j} t^{x_j, r_j} \cdot \mathbb{G}^{lead}_j(x_j, x'_j) \cdot t^{x'_l, r'_j *}] \ . \tag{3.11}$$

If instead of computing the total transmission from lead to lead (3.10) we wanted to compute the individual transmission amplitudes between the modes of the leads, this is possible by a change of basis of the lead Green's function matrices from the "lattice site-representation" to the "wavemode representation" [1]. In the IQH regime, we can however individually measure single edge modes by means of the cross-gate technique (section 1.3) which is easy to implement numerically by raising the onsite energies of some regions up to locally forbid the transmission of the outer ES, so this change of basis is not in principle necessary as long as we are interested in the square modulus of transmission amplitudes for each edge channel.

The computation of the total Green's function from L to R, through Eq.(3.10), is sufficient in order to compute the current from lead to lead, which is a *global* property of the system. We might however be interested in *local* properties, such as the charge density.

If the system is at equilibrium, and is characterized by a distribution function (1.16) we can write the local charge density as

$$\rho(r_n) = -\frac{1}{\pi} \int_{-\infty}^{+\infty} \mathrm{Im} G^{ret}(r_n, r_n; \epsilon) f(\epsilon) d\epsilon \ , \tag{3.12}$$

where G^{ret} is the Green's function of the total system attached to the leads, evaluated in a single site r_n. In computational terms, we find the discretized version of G^{ret} by means of Eq.3.8 (see Fig.3.2): we need to evaluate $G^{S(L,i-1)}$ and $G^{S(i+1,R)}$ and couple these partial Green's functions with two cycles of iteration (3.9) to g_{ii} defined as in Eq.(3.7).

Smooth potential steps With reference to Section 2.1, the RGF technique allows to simulate the scattering from an abrupt electric potential barrier in a very simple way, but differently from the MM-method in its standard formulation (for the calculations of the currents) it does not give a straightforward access to the complex scattering matrix of the barriers. More precisely, the charge-densities obtained through

[6] Strictly speaking, as shown in Ref. [49] and briefly discussed later in this section, the Fisher-Lee relation is more complicated in system with magnetic fields in the leads. The standard relations we derive here are however valid as long as we compute *total* currents from one lead to another (i.e. we sum over the matrix elements in real space).

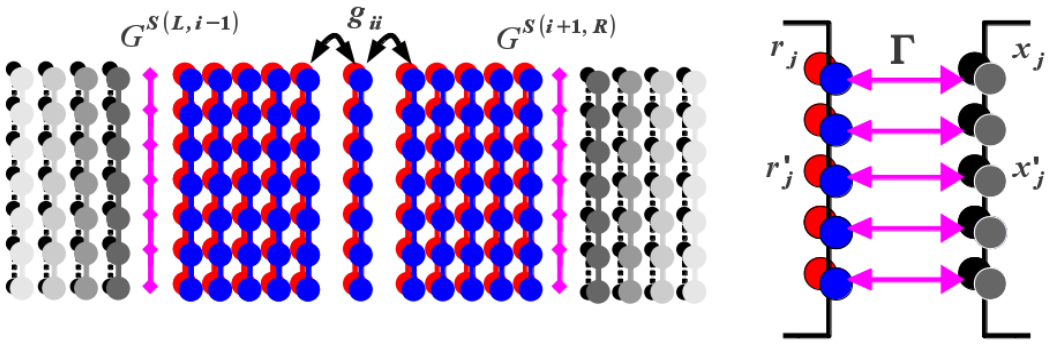

Figure 3.2: Schematics of a two-terminal system on a lattice. **Left panel**: pictorial view of the calculation procedure for the numerical local charge density (3.12) **Right panel:** pictorial view of the coupling due to system-lead matrices $\Gamma^{j}_{r_j r'_j}$ (3.11)

$\rho(x,y) = |\Psi(x,y)|^2$ from the steady-state solution of the MM procedure (such as the one calculated with the MM-method in Fig.2.4), should be equal to the RGF simulation of an equivalent finite-size system.

In Figure 3.3, we show an example of a two-terminal Hall bar where the source and drain are separated by a *high* potential step, as those considered in Section 2.2.2, i.e. we allow the potential variation to be as large as to change the local filling factor of the underlying 2DEG. The abrupt opening of a new channel, and the consequent change of the number of propagating eigenmodes after crossing the step, allow the incoming wavepacket to delocalize itself over the two channels in region II, as shown in Fig.2.6.

The RGF technique allows us to easily address the effect of the smoothening of the step and to describe the cross-over to the adiabatic regime occurring when the potential varies over a length which is larger than the magnetic length. Numerical simulations are performed by replacing the sharp step with a potential of the form $U(y) = -\Delta E/(e^{y/d}+1)$, where d is the characteristic length (width) of the potential. In Fig. 3.3 density plots of the probability density are shown when electrons are injected from the left in channel 1 for three different values of d, namely $d = 0.5l_B$ (a), $d = 1.3l_B$ (b) and $d = 3.5l_B$ (c). Vertical lines represent the center position of the step potential. For $d = 0.5l_B$, there are beatings on the right hand side of the barrier which correspond to the coherent superposition of electronic waves over the two edge channels[7] (the period of the oscillations corresponds to 2π divided by the difference of the wave-numbers of the two outgoing modes, as expected). Such beatings are progressively suppressed as the barrier becomes smoother, eventually disappearing for $d = 3.5l_B$ (see Fig. 3.3c), when the edge channel injected from region I is totally transmitted to region II without mixing. All simulations that we have performed confirm the picture of a crossover from the channel mixing situation to the adiabatic regime, reached when the potential step varies over a scale of a few magnetic lengths.

Numerical Details and Computation Time In order to perform the calculations of this thesis work with the RGF method, distinct approaches and numerical packages have been used.[8]

[7] It is worthwhile noting that the plot relative to $d = 0.5l_B$ is indistinguishable from the plot relative to a sharp edge, which has been computed by means of the MM method.

[8] While each of the numerical packages used could in principle be adapted to simulate *all* cases under study, we opted for using different codes, which were already developed by the scientific community or by the QTI group in Pisa, as a programming base. This allowed us to benefit of useful advanced

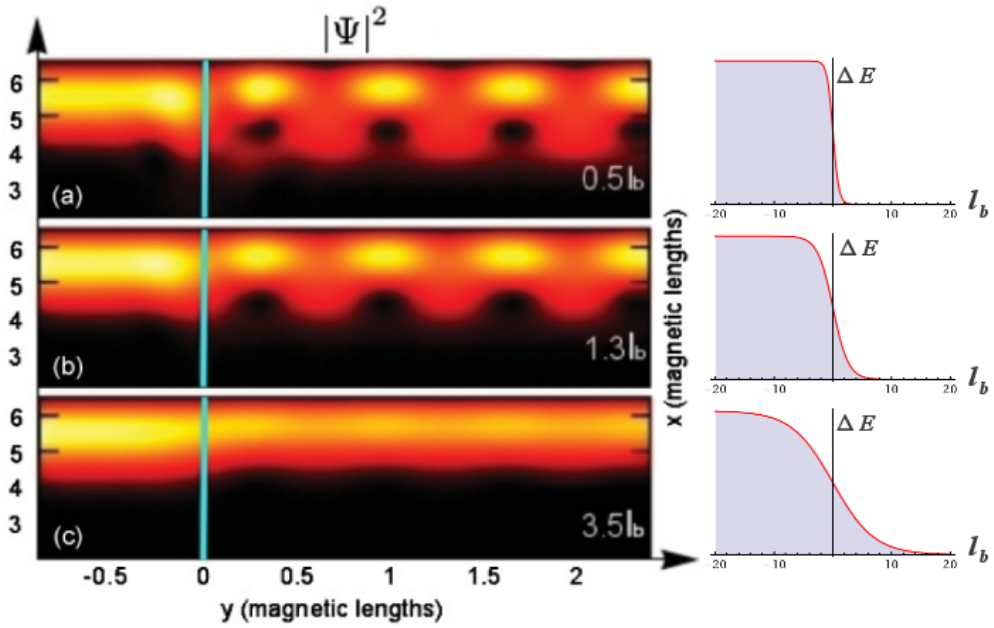

Figure 3.3: **Left panel**: Charge density plot for the case where $P_I = 1$ and $P_{II} = 2$ with a smooth step potential characterized by a width d. Vertical lines correspond to the center position of the step potential. Panel (a), (b) and (c) are relative to, respectively, d=0.5, 1.3 and 3.5 magnetic lengths (see corresponding profile of $U(y)$ in the images on the right panels).

The results obtained with the MM technique have been verified and extended to smooth steps making use of an adaptation of a code (written in Fortran-95) used also in Refs.[52]. It exploits the RGF iteration by implementing the Dyson Equation slice-by-slice as detailed in the text above, leads Green's functions are computed numerically and only the total transmission from lead to lead is computed. For the simulations of the experiment that will be described in the next Section 3.2, we worked on an adaptation of a Fortran-77 RGF code which was originally used in Refs.[54]. It implements the decimation/renormalization procedure by working directly on the Hamiltonians instead of the Green's functions, and allows one to optimize the system-lead matching by individually resolving the modes in the leads[50].

For the modeling of the experiment presented in Sections 3.3, we modified instead the open-source package KNIT for tight-binding simulations[57], adapting it for a spinful four-terminal IQH system. This program, written in C++ and in Python, implements a recursion cycle which acts on single lattice sites, instead of decimating chains of sites per iteration step. This allows great flexibility concerning the geometry of the device. The modes in the leads are not resolved by means of a change-of-basis/projection procedure, but they are individually addressed by simulating the cross-gate technique (see as an example the simulation pictured in Fig.3.12).[9]

All the codes which have been used for the computation are adapted to work on a single processor, and are optimized by standard compiler options, so that a single run (which can include either a disorder configuration or a complex potential/magnetic

numerical techniques tested in other contexts, and gain significantly in development time.

[9] We note that all these three codes suffer from a numerical instability that occurs if the leads are too wide. The nature of this technical problem that arises in RGF methods when high magnetic fields are considered is well known, and some (quite involved) workarounds exists in the literature [50]. However, for the work described in this thesis the codes have been used for reasonably narrow leads and we checked that these problems do not occur for our calculations.

field landscape) tipically lasts few minutes on ordinary personal computer at time of writing, for the computation of the global transmission matrix.

3.2 Scanning Gate Microscopy and Edge States Equilibration

The quest to fabricate a coherent beamsplitter for co-propagating edge channels, which is the building block of the interferometry proposal of Fig.1.6, has begun at NEST laboratory of Scuola Normale Superiore di Pisa, with some experiments aiming to characterize the coherent transfer of charge between adjacent cyclotron-resolved edge states. In one of them [58], the experimentalists were able to locally influence the transport occurring in a four-terminal 2DEG in the Quantum Hall regime at $\nu = 4$ by means of the *Scanning Gate* (SG) technique [59], and thus to obtain for the first time spatially-resolved maps of the equilibration process occurring between co-propagating edge states corresponding to different LLs.

Fig.3.4 shows the top view of the experimental device and the conceptual scheme of the transport measurement. The 2DEG is maintained in the cyclotron-resolved IQH regime by a perpendicular magnetic field of 3.2T ($l_B = 14.3nm$). The experiment is conducted at a temperature of $0.4K$, so the thermal energy is negligible with respect to the Landau gap ($5.7meV$, see Tab.1.1). The idea is to selectively bias one channel which is then coupled for a certain length with an adjacent co-propagating unbiased ES (the "probe" channel). This length can be continuously varied by means of a suspended tungsten gate (SG-tip), which provides a potential barrier for the biased channel, which is adiabatically reflected and measured in one ohmic contact. The probe channel is finally measured, and any excess current that is present on the channel must necessarily be a result of charge transfer which occurred in the region where the two co-propagating channels were adjacent.

Differently from other edge channel equilibration experiments performed at similar experimental conditions [55, 56], the transport characteristics of the device are highly tunable, since the charge transfer occurs in a narrow region defined inside a QPC defined by two side gates separated by $1\mu m$ (see Fig.3.4). We also note that the charge equilibration signal produced by this measurement setup doesn't give direct access to information regarding the *energy equilibration* process, which is mediated mainly by Coulomb interactions and can occur also in absence of charge-transfer mechanisms [106].

The biased channel is excited by a small constant voltage superimposed with a sinusoidal low-frequency AC signal (*lock-in technique*). $V = V_{DC} + \delta V \sin(\omega t)$. If V_{AC} is small enough that the transmission coefficients $T(\epsilon + eV_{DC}) \simeq T(\epsilon + eV_{DC} + eV_{AC})$ and the thermal energy are irrelevant, the measured conductance $G = \delta I / V_{AC}$ is (see Eq.(1.15))

$$G = \frac{2e^2}{h}[T_{12}(eV_{DC}) + T_{22}(eV_{DC})] \; . \tag{3.13}$$

We simulated the Hall bar with a discretized numerical model which is much smaller in width than the experimental bar (41 sites, resulting in a total width of about 98 nm, or $\simeq 7\ l_B$), but captures the essential physics of the transport in the narrow channel of the QPC. The channels are defined by hard wall confinement potentials, and the spin-degree of freedom is not resolved in the experiment, so that there is no need to introduce a sublattice as explained in Section 3.1.

The SG tip effect on the 2DEG is modeled as a Gaussian potential [63], with a characteristic width σ sufficiently large to make sure that it is not coupling the channel by

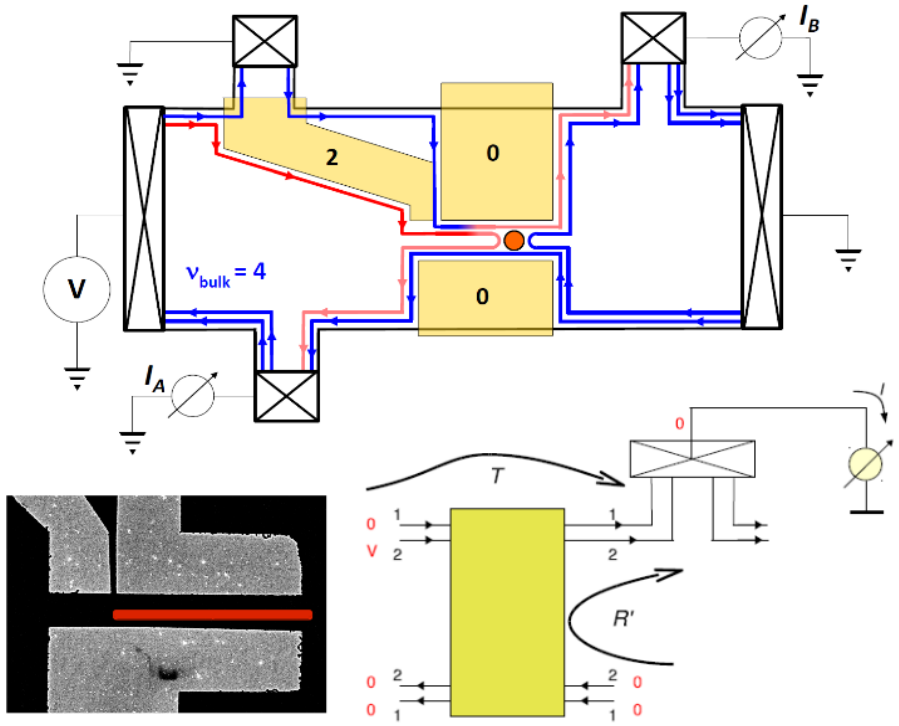

Figure 3.4: **Top panel**: schematics of the experimental device considered. The biased channel (red) is forced to co-propagate next to another edge channel (first blue, then pink) by exploiting the cross-gate technique. The numbers under the gates (yellow regions) represent local filling factors. The position of the SG-tip (orange circle) determines the length of interaction of the two ES. **Bottom left panel**: SEM picture of the QPC over which the SG-tip is scanned (gray zones correspond to the metallic gates). The red rectangle is the confined transport zone which will be simulated and where the equilibration effect will take place. **Bottom right panel**: Landauer-Buttiker scattering modelization of the transport experiment: the yellow zone represents the scattering matrix (see Eq.(1.21)). t_{12} is the transmission amplitude from biased channel 2 (at the left of the scattering zone) to the unbiased channel 1 (at the right of the scattering zone) which is then measured.

itself (i.e. it is considered adiabatic on the scale of l_B). The intensity of the field generated by the tip is taken to be of the order of $2\hbar\omega_c$, such to block completely deplete the electron gas underneath and thus block the transport among the two terminals if the SG-tip is in the middle of the channel. The Gaussian shape of the SG-tip potential has a width of $\sigma = 45nm$. In Fig.3.5 we show the "conductance maps" of the constriction: both incoming channels are biased by V_{DC}, and the total conductance (3.13) is measured as a function of the position of the SG-tip potential on the 2DEG. Despite the small transverse extension of the channel, and the effective rescaled potentials of the tip and the impurities, simulations are able to reproduce the effect of selectivity of the channels which are transmitted/reflected. Depending on the intensity and the position of the Gaussian bump, the tip can locally induce a filling factor smaller than 4, effectively reflecting some channels back to the source.

The main objective of the experiment consisted in a current measurement which is performed with only one (channel 2 in Fig.3.4) of the two incoming ES biased with

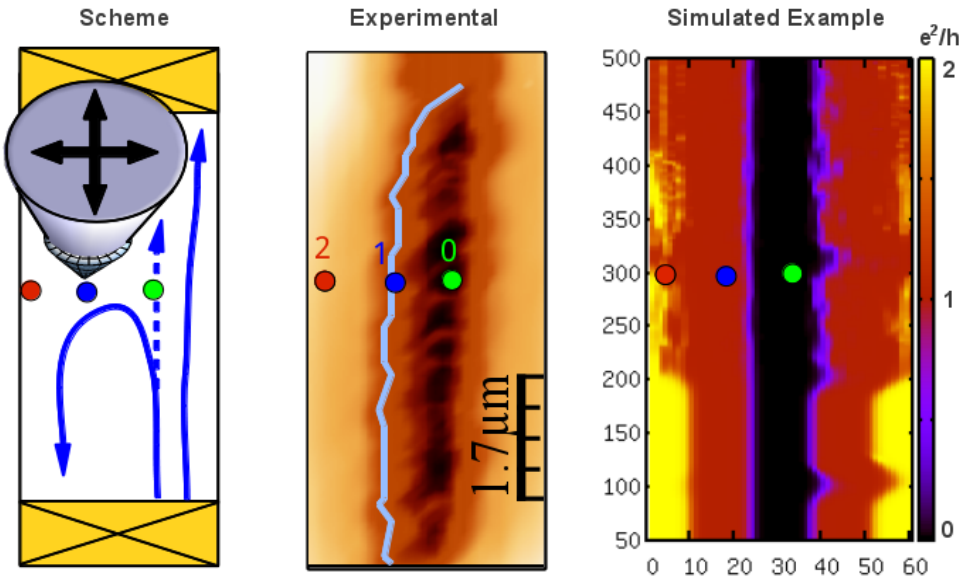

Figure 3.5: **Left panel**: schematics of the conductance map scanning, the total current carried from the two incoming edge channels is measured, and depends on the position of the tip. **Center panel**: experimental conductance map, dark regions represent low current signal. When the tip is in points such as the red spot, two ES contribute to the conductance, when it is in the blue spot only one channel is measured, while when the tip is in the green spot both channels are reflected. The blue trajectory indicates a possible path of scanning in which a single channel is transmitted and one is reflected. **Right panel**: example of a simulated conductance map with a tight-binding approach (numbers in the axes represent lattice sites. The lattice spacing is $a = 2.4nm$). The inhomogeneities which are visible at the center of the maps are due to the presence of fixed strong impurities as detailed in the text.

$V_{DC} = 100\mu V$ and $V_{AC} = 50\mu V$, so that in terms of the LB formalism the measured conductance is the crossed transmission coefficient evaluated at the Fermi energy

$$G \simeq \frac{2e^2}{h} T_{12}(\epsilon_F) \ . \tag{3.14}$$

Previous theoretical expectations for IQH edge channels [21] indicate that at low temperature and low bias, static unscreened potential fluctuations (which are expected to be originated by the donor layer [62] or lattice imperfections) are the main source of charge transfer among the channels. This idea is consistent with the visible inhomogeneities in the experimental conductance maps presented in Fig.3.5, and with previous similar experimental results in the literature [146], so we introduce in the model Hall bar localized "impurities" that are meant to couple the co-propagating channels. Relying on the results discussed in Chapter 2 and Section 3.1.1 for estimating the effect of narrow high potential steps, these *strong fixed impurities* are modeled as "sharp" Gaussian potentials, whose intensity is of the order of the cyclotron gap $\hbar\omega_c$ and whose characteristic width is $\sigma \simeq l_B \simeq 15nm$.[10]

[10] It is important that this width is not too small with respect to the ES separation in order to induce some coupling, since the impurity scattering rate is exponentially suppressed with the distance between the channels [61].

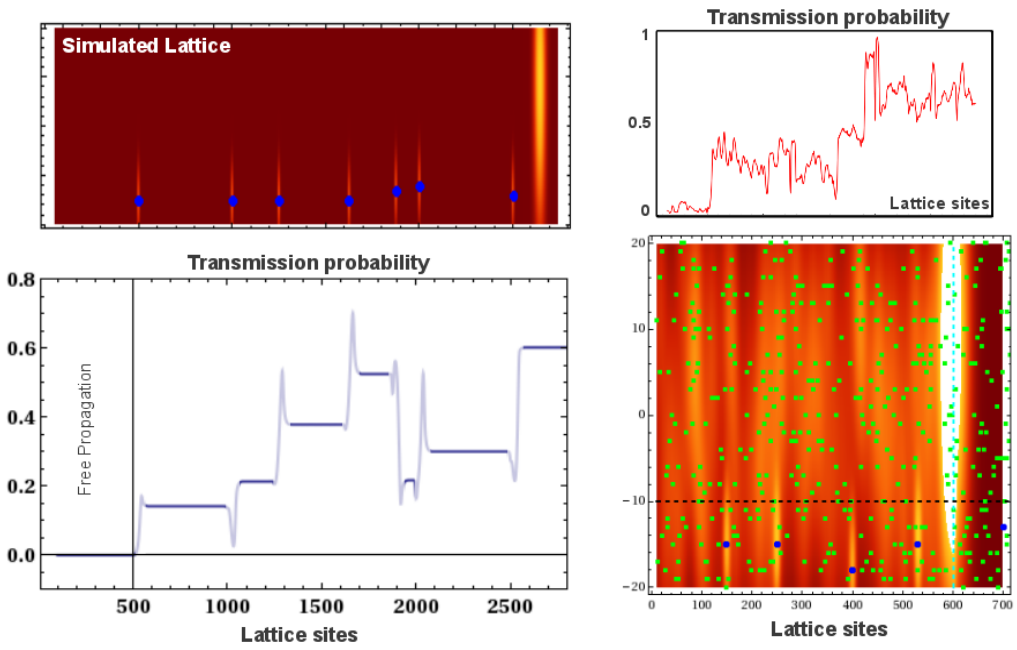

Figure 3.6: **Top left panel**: example of a simulated lattice with some *fixed* strong impurities (blue points) distributed randomly on the propagation channel. The Gaussian profile of the impurity potential is shown in the background (the strong ellipsoid at the end is the tip potential). The stretched shape is due to the aspect ratio of the simulated Hall-bar, whose size is $0.90\mu m \times 600\mu m$. **Bottom left panel**: transmission coefficient $|t_{12}|^2$ corresponding to the top panel when scanning with the tip on an horizontal trajectory: each strong impurity mixes randomly the channels. The transient spikes between the step-like structure are artifacts due narrow channel effects, since the tip potential plus the impurity induces a spurious reflection. **Bottom right panel**: example of a potential density plot of some fixed impurities (blue) with low-intensity *fluctuating* disorder (green points). **Top right panel**: example of how the transmission probability looks like once a given disorder configuration is included.

Dephasing and Disorder-Averaging In Section 2.2.1 we discussed the effect of a series of arbitrary scattering centers on the transmission amplitude between two incoming chiral IQH edge modes, and we found that the result strongly depends on the relative phase between the two channels at each scattering event. This scenario is indeed confirmed also in our 2D tight-binding simulations. In Fig.3.6 we show the effect in the mixing of a series of strong impurities in the regions where the two edge channels propagate. Each scatterer is responsible for a jump in the conductivity, but the actual amount and sign of charge transfer depends on the details of the potential.[11]

We need to acknowledge that the real transport system is millimetric in size and includes many more gates than our simulated system. This complexity can produce several sources of phase-averaging (thermal smearing, self-averaging...[2]) and/or decoherence (structured impurities, electron-electron interactions... [71, 72]) which are not present in our numerical model, but are likely to affect the current measurement.

[11] Being the channel narrow, we carefully placed the strong impurities in regions sufficiently close to the measured edge channels so to be sure that they wouldn't couple the modes on one edge with the counterpropagating modes in the other edge (backreflection). This condition is violated only when the tip potential adds up to the strong impurity potential (see the spikes in Fig.3.6).

These effects of decoherence or phase-averaging might be accounted effectively in calculations by evaluating the *average* transmission of many simulations run with the same fixed strong scatterers plus an additional random configuration of weak scatterers, or *background impurities*, which influences the mixing effect of the strong impurities differently for each system realization.

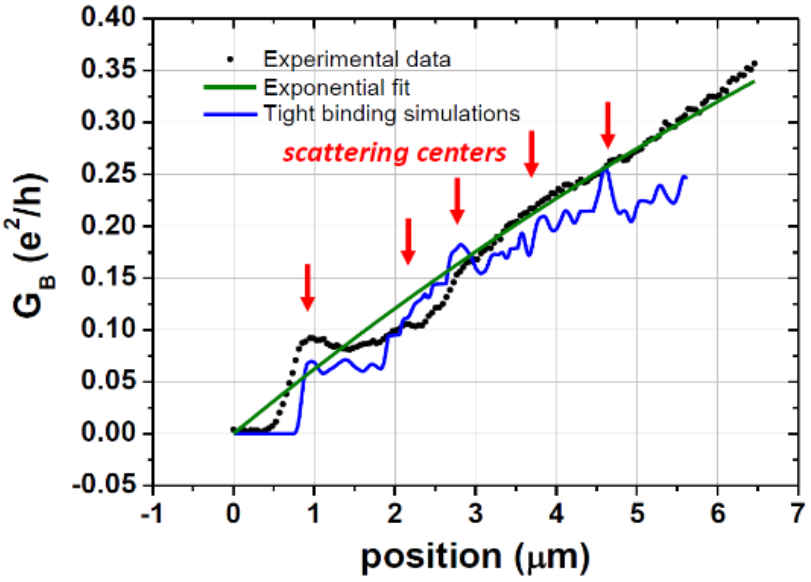

Figure 3.7: Spatially resolved channel equilibration, comparing experimental results, tight-binding simulations and incoherent exponential fit. The theoretical curve has been obtained as an average over 200 independent realizations of the disorder (see text for parameters and details). Fixed strong impurities positions (indicated as right arrows in the curve) have been placed on purpose in the region of channel propagation with reference to the inhomogeneities visible in the conductance maps (see Fig.3.5). The initial jump in the curve at the position of the first scatterer indicates also the region where the edge channels start to co-propagate and to be coupled by weak impurities.

More precisely, superimposing to the strong impurities a fixed "perturbative" disordered landscape of weak impurities still generates a non-monotonic transmission current signal (see Fig.3.6). The weak impurity background effectively randomizes the phase differences between the strong scattering centers, in the sense that the final value of the fully coherent transmission amplitude, after a given distance of propagation, strikingly depends on the microscopic details of the impurity spatial configuration encountered by the electrons propagating along the channels.

As already observed in section 2.2.1, the average among the possible phases acquired during propagation in the channels restores a monotonic increasing behavior of the mixed current as the number of scatterers gets bigger, which is intuitive from a classical point of view. The experimental findings (Fig.3.7) of the previously presented scanning-gate experiment suggest that there is some phase-averaging mechanisms going on, since after $1\mu m$ of propagation the curve has a smooth monotonic behavior (which can be compatible with a classical exponential equilibration model [22]). There are however visible bumps in the curve which hints the relevance of a coherent process in the mixing process.

Our conclusion is that in the elastic limit, when we introduce some averaging mechanisms over the phases of the ES in the system, the generic simulated model seems to

reproduce the basic physics of the equilibration process.

Future experiments aim to measure the noise in the channels and to create loops in the ES trajectories so to realize a tunable interferometric setup, as in Ref. [26]. Observing interference and measuring correlations in the signal is likely to allow more precise investigations on the nature of the dephasing mechanisms which, as different decoherence effects are indistinguishable in standard current measurements [23].

Spatially resolved analysis of edge-channel equilibration in quantum Hall circuits

Nicola Paradiso,[1] Stefan Heun,[1,*] Stefano Roddaro,[1] Davide Venturelli,[1,2] Fabio Taddei,[1]
Vittorio Giovannetti,[1] Rosario Fazio,[1] Giorgio Biasiol,[3] Lucia Sorba,[1] and Fabio Beltram[1]
[1]*NEST, Istituto Nanoscienze–CNR and Scuola Normale Superiore, Pisa (PI), Italy*
[2]*Institut NEEL, CNRS and Université Joseph Fourier, Grenoble, France*
[3]*Istituto Officina dei Materiali CNR, Laboratorio TASC, Basovizza (TS), Italy*
(Received 11 February 2011; revised manuscript received 18 February 2011; published 8 April 2011)

We demonstrate an innovative quantum Hall circuit with variable geometry employing the movable electrostatic potential induced by a biased atomic force microscope tip. We exploit this additional degree of freedom to identify the microscopic mechanisms that allow two co-propagating edge channels to equilibrate their charge imbalance. Experimental results are compared with tight-binding simulations based on a realistic model for the disorder potential. This work provides also an experimental realization of a beam mixer between co-propagating edge channels, a still elusive building block of a recently proposed new class of quantum interferometers.

DOI: 10.1103/PhysRevB.83.155305 PACS number(s): 73.43.−f, 72.10.Fk

I. INTRODUCTION

Suppression of backscattering and a very large coherence length are the characteristic properties of edge states[1] in the quantum Hall (QH) regime at the basis of the newly developed quantum electron interferometry. In this field a number of breakthroughs have appeared in recent years, such as the experimental realization of Mach-Zehnder,[2–5] Fabry-Pérot,[6] and Hanbury-Brown-Twiss[7] electron interferometers. In these devices the electronic analog of a beam splitter is obtained by a quantum point contact, a powerful tool which we have recently used to study the electron tunneling between *counterpropagating* edge states.[8–11] The constantly growing flexibility in the practical realization of QH nanostructures stimulates further investigations and different designs that are often inspired by quantum optics. One particularly appealing possibility is to exploit interference of *co-propagating* edge channels since it allows the concatenation of several interferometers.[12] Within this architecture, a beam splitter can be realized by sharp, localized potentials capable of inducing coherent interchannel scattering; see, e.g., Refs. 13–17. Appropriate design of such interferometers requires the detailed understanding of the physics of co-propagating edges.

Several groups[18–22] measured charge transfer and the electrochemical potential imbalance equilibration between co-propagating edge channels. Müller *et al.*[18] and Würtz *et al.*[21] interpreted their results in terms of classical rate equations, while only very recently the contribution of coherent effects in the equilibration process has been considered.[23,24] In these experiments, two co-propagating edge channels originating from two Ohmic contacts at different potential meet at the beginning of a common path of fixed length d where charge transfer tends to equilibrate their voltage difference.[21] At the end of the path the edge channels are separated by a selector gate and guided to two distinct detector contacts. Consequently, while these setups yield valuable information on the *cumulative* effect of the processes taking place along the whole distance d, they make it impossible to link charge transfer to local sample characteristics.

In order to shed light on this issue, in this paper we present a different approach to scanning gate microscopy (SGM) that allows us to investigate the spatial evolution of the interchannel scattering between co-propagating edge states in the QH regime with unprecedented spatial resolution. Here, the SGM tip is used not merely as a probe, but as an active component of a complex device which permits one to address quantum structures whose dimensions can be tuned during the measurement. For this purpose, we implemented a special QH circuit with variable geometry, in which the length of the interaction path can be continuously changed by positioning the biased tip of the SGM (see Fig. 1). This movable tip introduces a new degree of freedom for transport experiments, since it allows us to continuously control the size of a single component of the device under investigation during the same low-temperature measurement session. For large values of d our findings are consistent with the results of Refs. 18, 19, 21, and 22; i.e., the bias imbalance shows an exponential decay whose characteristic length is the equilibration length ℓ_{eq}. For small d, however, we are able to reveal by a direct imaging technique the effect of individual scattering centers in transferring electrons among co-propagating edges. Numerical simulations of the device based on the Landauer-Büttiker formalism[25,26] show that interchannel scattering can occur while coherence is maintained, suggesting the possibility that such mechanisms could be used as the basic ingredient to build simply connected, easily scalable interferometers along the lines proposed in Ref. 12.

II. EXPERIMENTAL DETAILS

The samples for this study were fabricated starting from an $Al_{0.33}Ga_{0.67}As/GaAs$ heterostructure with a two-dimensional electron gas (2DEG), which is confined 55 nm underneath the surface. Its electron sheet density and mobility at low temperature are $n = 3.2 \times 10^{15}$ m^{-2} and $\mu = 4.2 \times 10^{2}$ m^{-2}/V s, respectively, as determined by Shubnikov–de Haas measurements.

The Hall bar was patterned via optical lithography and wet etching. Ohmic contacts were obtained by evaporation and thermal annealing of a standard Ni/AuGe/Ni/Au multilayer (10/200/10/100 nm). All gates were defined by electron-beam lithography and consist of a Ti/Au bilayer (10/20 nm). Two nominally identical devices (S1 and S2) were produced, as outlined in Fig. 2.

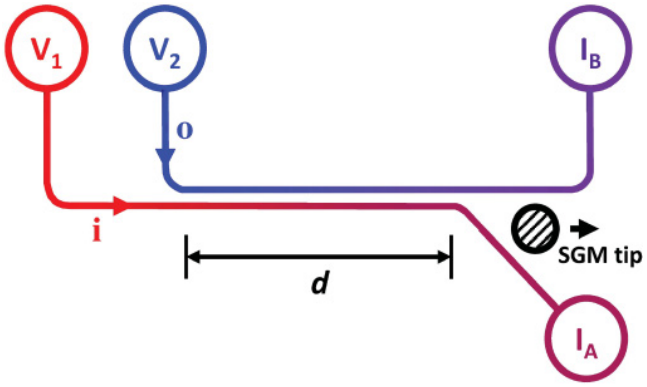

FIG. 1. (Color online) Schematic drawing of the key idea behind our experiment: The SGM tip is used to actively control the edge trajectories to obtain a continuously tunable interaction region length d. This allows a spatially resolved analysis of the equilibration process.

Our measurements were performed with the 2DEG at bulk filling factor $\nu_b = 4$ ($B = 3.32$ T). At such field, the effective distance between edge states separated by the cyclotron gap ($\hbar\omega_c = 5.7$ meV) is of the order of 100 nm, as we showed in our previous measurements on a similar sample.[27] In general, in a sample with a given confinement profile the interedge channel distance is proportional to the energy gap between Landau levels. Since the Zeeman gap is of the order of 0.1 meV (we assume $g^* = -0.44$),[28] the distance between Zeeman-split edge states is so small that they cannot be resolved in our experiment. Thus here we consider pairs of Zeeman-split edges as one individual channel carrying $2G_0 \equiv 2e^2/h$ units of conductance. Finally, since we work at $\nu_b = 4$, two spin-degenerate edge channels are populated.

The SGM system is mounted on the cold finger (base temperature 300 mK) of a ^{3}He cryostat.[27] The sample temperature, calibrated with a Coulomb blockade thermometer, is 400 mK. The maximum scanning area of the SGM at 300 mK is 8.5 μm × 8.5 μm. The coarse and fine control of the tip-sample position is provided by a stack of piezo-actuators.

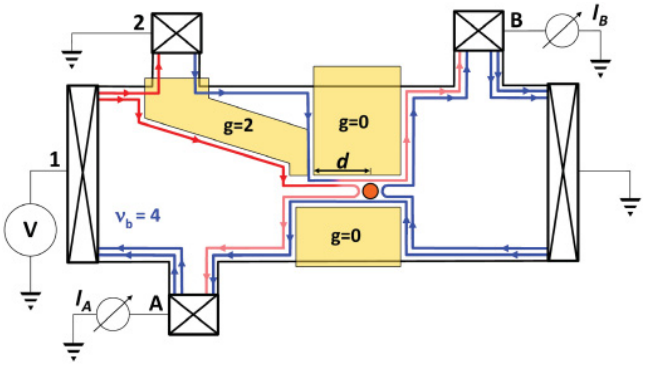

FIG. 2. (Color online) Scheme of the experimental setup. Three Schottky gates are used to independently contact two co-propagating edge channels and to define a 6-μm-long and 1-μm-wide constriction. Using the SGM tip it is possible to selectively reflect the inner channel and define a variable interedge relaxation region length d.

The sample is mounted on a chip carrier positioned on top of the piezo-scanner. The SGM tip was obtained by controlled etching of a 50-μm-thick tungsten wire. This resulted in tips with a typical radius of about 30 nm. The tip was then glued on a quartz tuning fork, which allowed us to perform topography scans by controlling the oscillation amplitude damping due to the tip-sample shear force. Due to the close tip-sample proximity, during the topography scans both the tip and the gates are temporarily grounded in order to avoid shorts. On the other hand, during the SGM measurements the tip (biased at the voltage $V_{\rm tip} = -10$ V) is scanned about 40 nm above the heterostructure surface, in order to avoid both accidental contacts between the biased tip and the gates and to keep the tip-2DEG distance constant, irrespective of the topographic details.

The cryostat is equipped with a superconducting magnet coil which provides magnetic fields up to 9 T. The whole setup is decoupled from the laboratory floor by means of a system of springs in order to damp mechanical noise. Images are processed with the WSXM software.[29] In all conductance maps shown in this paper, the effect of the series resistance of both the external wires and the Ohmic contacts has been subtracted.

The geometry of the QH circuit is determined by the electrostatic potential induced by three Schottky gates and the SGM tip. The upper left gate in Fig. 2 defines a region with local filling factor $g = 2$, which selects only one of the two channels propagating from contact 1 at voltage V and guides it toward contact 2. When this is grounded, an imbalance is established between edge channels at the entrance of the constriction defined by the two central gates at local filling factor $g = 0$. The two channels propagate in close proximity along the constriction, which is 6 μm long and 1 μm wide. In our experiments, we suitably positioned the depletion spot induced by the biased tip of the SGM so that the inner channel is completely backscattered, while the outer one is fully transmitted. As a consequence, the two channels are separated after a distance d that can be adjusted by moving the tip. Since the outer edge was grounded before entering the constriction, the detector contact B will measure only the electrons scattered between channels, while the remaining current is detected at contact A.

III. RESULTS

The peculiar geometry of this QH circuit implies that all measurements critically depend on the ability to set the edge configuration so that the inner edge is perfectly reflected while the outer one is fully transmitted. To this end, we first performed topography scans [Fig. 3(a)] yielding a reference frame to evaluate the relative position of the tip with respect to the confining gates in the subsequent SGM scans. Then we performed calibration scans aimed at establishing tip trajectories ensuring that the inner channel is indeed completely backscattered, while the outer one is fully transmitted (edge configuration as sketched in Fig. 2). In these scans, a small ac bias (50 μV) was applied to source contact 1, while contact 2 was kept floating so that both channels at the entrance of the central constriction are at the same potential and carry the same current $I_1 = I_2 = 2G_0V$. Figure 3(b) shows a

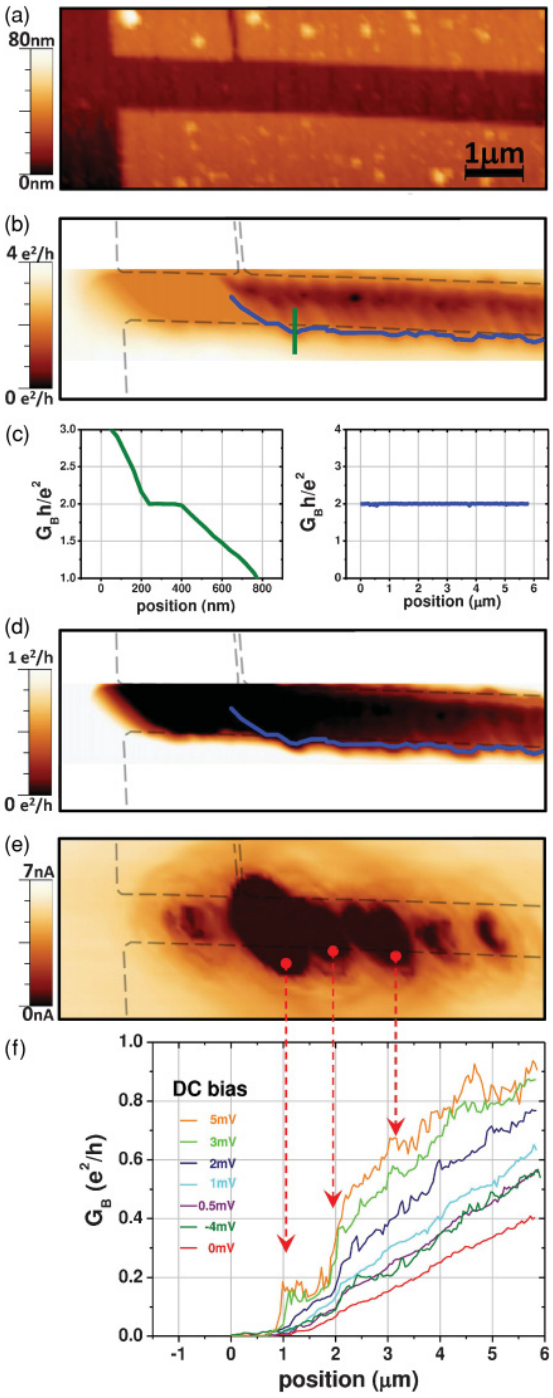

FIG. 3. (Color online) (a) Topography scan of device S1. (b) Calibration scan: The SGM map refers to the differential conductance signal measured at contact B when contact 2 is floating. $V_{\text{tip}} = -10$ V. (c) Conductance profiles measured along the green (left panel) and the blue (right panel) line in (b). (d) Imaging of the interchannel equilibration (contact 2 grounded). (e) SGM measurement at zero magnetic field, with dc source bias $V = 100$ μV. (f) Finite bias equilibration signal measured along the trajectory determined by means of the calibration scan. There is a clear correlation between the steps in the equilibration curves and the position of scattering centers in the SGM scan at zero magnetic field. Furthermore, we observe an enhancement of the equilibration steps with increasing bias.

map of the differential conductance $G_B = \partial I_B/\partial V$ measured at contact B by standard lock-in technique and obtained by scanning the biased tip inside the constriction. The color plot of Fig. 3(b) can be interpreted as follows: when the tip is far from the constriction axis both channels are fully transmitted to the drain contact B and the measured total conductance is $G_B = 4G_0$. By moving the tip toward the axis of the 1D channel, the inner edge channel is increasingly backscattered and the conductance decreases until we reach a plateau for $G_B = 2G_0$ [left panel of Fig. 3(c)]. This plateau is due to the spatial separation δ between the two edge channels. In fact, once the inner channel is completely backscattered, it is necessary to move the tip approximately 2δ further before reflection of the outer one occurs, as discussed in Refs. 30 and 27. Thus the tip trajectory ensuring the desired edge configuration (Fig. 2) was determined as the locus of the middle points of the plateau strip [blue line in Fig. 3(b)]. As shown in the right panel of Fig. 3(c), the conductance along this trajectory is constant and equals the conductance of a single channel, i.e., $2G_0$.

Next, we imaged the interchannel differential conductance. The two edge channels entering the constriction were imbalanced by grounding contact 2. In this configuration, at the beginning of the interaction path, only the inner channel carries a nonzero current, i.e., $I_1 = 2G_0V$, where V is the source voltage. The electrochemical potential balance is gradually restored by scattering events that take place along the interaction path, which yields a partial transfer of the initial current signal from the inner to the outer channel. The device architecture allowed us to detect both transferred electrons and reflected ones by measuring the current signal at contacts B and A, respectively. We verified that the sum of currents measured at A and B is constant and always equal to $2G_0V$.

Figure 3(d) shows the SGM map of the interchannel differential conductance G_B at zero dc bias. The key feature of this scan is the monotonic increase of the scattered current as a function of the interaction distance d. This can be directly observed in Fig. 3(f), where we show several finite-bias conductance profiles acquired along the trajectory determined in the previous calibration step. For a given value of d, the dramatic enhancement of the equilibration for finite dc bias is consistent with the results obtained by means of I-V characteristics in samples with fixed interaction length.[21] In particular, for dc bias of the order of the cyclotron gap, $\hbar\omega_c = 5.7$ meV, the differential conductance reaches its saturation value $G_B = G_0$, which corresponds to a transmission probability $T_{12} = 0.5$, i.e., $I_A = I_B$.

All curves in Fig. 3(f) are characterized by sharp steps in some positions. This behavior was confirmed by measurements on other devices, which showed the same stepwise monotonic behavior, albeit with different step positions. This indicates that the scattering probability is critically influenced by local details of each sample, e.g., by the location of impurities that can produce sharp potential profiles whose effect in the QH interchannel scattering can be revealed by the SGM technique.[31] In order to correlate the presence of scattering centers with the steps in the conductance profile, we performed SGM scans at zero magnetic field [Fig. 3(e)]. Such a scan provides a direct imaging of the disorder potential and

can identify the most relevant scattering centers (see Refs. 32 and 33 for similar scanning probe microscopy investigations). A comparison between Figs. 3(e) and 3(f) shows a clear correlation between the steps in the conductance profiles with the main spots in the disorder-potential map. This is the central finding of the present work and establishes a direct link between the atomistic details of the sample and the interchannel transport characteristics. Such correlation is impossible to detect with standard transport measurements and requires the use of scanning probe microscopy techniques.

It is important to note that interchannel transmission is nearly zero up to the first scattering center. This indicates that impurity-induced scattering is the dominant process equilibrating the imbalance, while other mechanisms that were invoked in literature, such as the acoustic-phonon scattering, have only a negligible effect for short distances, in agreement with the theoretical findings of Ref. 19. We also observe that the step amplitude is suppressed when the length of the interaction path d is bigger than about 3 μm.

IV. DISCUSSION

In view of possible applications to QH interferometry, it is necessary to determine the degree of coherence of the position-dependent, interchannel differential conductance. For this reason we make use of a theoretical model which accounts for elastic scattering only and restrict our analysis to the zero-dc bias case. The system is described through a tight-binding Hamiltonian, where the magnetic field is introduced through Peierls phase factors in the hopping potentials. According to the Landauer-Büttiker formalism,[25,26] the differential conductance is determined by the scattering coefficients, which are calculated using a recursive Green's-function technique. Apart from a hard-wall confining potential, electrons are subjected to a disorder potential consisting of a few strong scattering centers on top of a background potential. Scattering centers are modeled as Gaussian potentials whose positions (which are different from device to device) are deduced from SGM scans in the constriction at zero magnetic field [Fig. 3(e) shows one example]. The height of the Gaussian potentials is of the order of the cyclotron gap and their spatial variation occurs on a length scale of the order of the magnetic length ($\ell_B \approx 15$ nm). The background potential is modeled as a large number of randomly distributed smooth Gaussian potentials, whose height is of the order of one tenth of the cyclotron gap. The conductance is finally calculated averaging over a large number of random configurations of the background potential to account for phase-averaging mechanisms which are always present in the system.

Figure 4 shows results of our simulations (solid blue line), together with the experimental data from device S2 for $V = 0$ (filled black dots) and an exponential fit (dashed green line). For short distances the computed conductance exhibits steps in correspondence to the scattering centers (positions indicated by red arrows in Fig. 4), while at larger distances it presents a monotonic behavior where the steps are washed out by the averaging over the background. Both regimes are consistent with the experimental data.

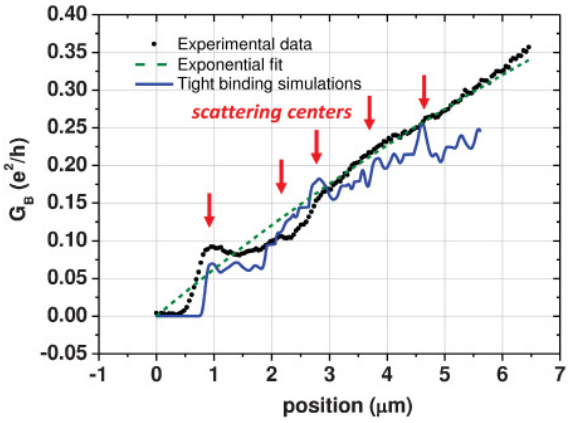

FIG. 4. (Color online) Results of the tight-binding simulations for the zero-bias case: the inter-channel, zero-temperature differential conductance (solid line) compared with experimental data from device S2 (filled dots). From the exponential fit (dashed line) we deduce an equilibration length $\ell_{eq} = 15$ μm. The position of strong scattering centers in the simulation is indicated by red arrows. Comparison of the curves in Figs. 3 and 4 demonstrates that the position of the jumps changes from sample to sample and critically depends on the specific distribution of the scattering centers in each sample, which is the main finding of our paper.

In Fig. 4 we also compare our experimental data with the exponential behavior $G_B = G_0(1 - e^{-d/\ell_{eq}})$ which was reported previously.[18,21] For short d, there is a discrepancy between the experimental conductance profile and the exponential curve, due to the discreteness of the scattering centers. On the other hand, for larger distances our experimental data are well fitted by the exponential curve. We would like to underline that here we actually directly verify this exponential behavior, by continuously tuning the interaction length d. In previous works, the equilibration length ℓ_{eq} was extracted from four-wire resistance measurements at fixed d, *assuming* an exponential dependence.[18,19,21,34] From our data we obtain an equilibration length $\ell_{eq} = 15$ μm, which is of the same order of magnitude as values reported in literature.[34]

We also performed measurements at bulk filling factor $\nu_b = 2$, so that the electron transfer takes place between two spin-split edge channels. In this case we did not observe equilibration at zero bias, consistent with the fact that typical equilibration lengths reported in literature for $\nu_b = 2$ are of the order of millimeters.[18] In view of possible applications such as beam splitter it is therefore advantageous to work at $\nu_b = 4$ since one needs to achieve a coherent mixing with an interaction path as short as possible.

In conclusion, we used the biased tip of a SGM as an active component of a QH circuit which implements a tunable beam splitter to mix co-propagating edge states. The ability to control the interaction path length allowed us to identify the microscopic mechanisms governing interchannel electron scattering. From the comparison of several conductance profiles [such as the one shown in Fig. 3(f)] acquired with different devices, we can conclude that scattering induced by impurities is the key process that enables charge transfer between the channels.

This conclusion is supported by theoretical simulations. This allows application of this device as a beam splitter in the simply connected Mach-Zehnder interferometer proposed in Ref. 12 and opens new possibilities in quantum electron interferometry.

ACKNOWLEDGMENTS

We acknowledge financial support from the Italian Ministry of Research (FIRB Projects No. RBIN045MNB, No. RBIN048ABS, and No. RBID08B3FM).

*stefan.heun@nano.cnr.it

[1]B. I. Halperin, Phys. Rev. B **25**, 2185 (1982).
[2]Y. Ji, Y. Chung, D. Sprinzak, M. Heiblum, D. Mahalu, and H. Shtrikman, Nature (London) **422**, 415 (2003).
[3]I. Neder, M. Heiblum, Y. Levinson, D. Mahalu, and V. Umansky, Phys. Rev. Lett. **96**, 016804 (2006).
[4]I. Neder, F. Marquardt, M. Heiblum, D. Mahalu, and V. Umansky, Nat. Phys. **3**, 534 (2007).
[5]P. Roulleau, F. Portier, D. C. Glattli, P. Roche, A. Cavanna, G. Faini, U. Gennser, and D. Mailly, Phys. Rev. B **76**, 161309(R) (2007).
[6]F. E. Camino, W. Zhou, and V. J. Goldman, Phys. Rev. Lett. **95**, 246802 (2005).
[7]I. Neder, N. Ofek, Y. Chung, M. Heiblum, D. Mahalu, and V. Umansky, Nature (London) **448**, 333 (2007).
[8]S. Roddaro, V. Pellegrini, F. Beltram, G. Biasiol, L. Sorba, R. Raimondi, and G. Vignale, Phys. Rev. Lett. **90**, 046805 (2003).
[9]S. Roddaro, V. Pellegrini, F. Beltram, G. Biasiol, and L. Sorba, Phys. Rev. Lett. **93**, 046801 (2004).
[10]S. Roddaro, V. Pellegrini, F. Beltram, L. N. Pfeiffer, and K. W. West, Phys. Rev. Lett. **95**, 156804 (2005).
[11]S. Roddaro, N. Paradiso, V. Pellegrini, G. Biasiol, L. Sorba, and F. Beltram, Phys. Rev. Lett. **103**, 016802 (2009).
[12]V. Giovannetti, F. Taddei, D. Frustaglia, and R. Fazio, Phys. Rev. B **77**, 155320 (2008).
[13]C. Tejedor and J. J. Palacios, Phys. Scr. T **35**, 121 (1991).
[14]J. J. Palacios and C. Tejedor, Phys. Rev. B **45**, 9059 (1992).
[15]J. J. Palacios and C. Tejedor, Phys. Rev. B **48**, 5386 (1993).
[16]O. Olendski and L. Mikhailovska, Phys. Rev. B **72**, 235314 (2005).
[17]D. Venturelli, V. Giovannetti, F. Taddei, R. Fazio, D. Feinberg, G. Usaj, and C. A. Balseiro, Phys. Rev. B **83**, 075315 (2011).
[18]G. Müller, D. Weiss, A. V. Khaetskii, K. von Klitzing, S. Koch, H. Nickel, W. Schlapp, and R. Lösch, Phys. Rev. B **45**, 3932 (1992).
[19]S. Komiyama, H. Hirai, M. Ohsawa, Y. Matsuda, S. Sasa, and T. Fujii, Phys. Rev. B **45**, 11085 (1992).
[20]Y. Acremann, T. Heinzel, K. Ensslin, E. Gini, H. Melchior, and M. Holland, Phys. Rev. B **59**, 2116 (1999).
[21]A. Würtz, R. Wildfeuer, A. Lorke, E. V. Deviatov, and V. T. Dolgopolov, Phys. Rev. B **65**, 075303 (2002).
[22]T. Nakajima, Y. Kobayashi, S. Komiyama, M. Tsuboi, and T. Machida, Phys. Rev. B **81**, 085322 (2010).
[23]E. V. Deviatov and A. Lorke, Phys. Rev. B **77**, 161302(R) (2008).
[24]E. V. Deviatov, B. Marquardt, A. Lorke, G. Biasiol, and L. Sorba, Phys. Rev. B **79**, 125312 (2009).
[25]M. Büttiker, Y. Imry, R. Landauer, and S. Pinhas, Phys. Rev. B **31**, 6207 (1985).
[26]M. Büttiker, Phys. Rev. B **38**, 9375 (1988).
[27]N. Paradiso, S. Heun, S. Roddaro, L. N. Pfeiffer, K. W. West, L. Sorba, G. Biasiol, and F. Beltram, Physica E **42**, 1038 (2010).
[28]K. J. Thomas, J. T. Nicholls, N. J. Appleyard, M. Y. Simmons, M. Pepper, D. R. Mace, W. R. Tribe, and D. A. Ritchie, Phys. Rev. B **58**, 4846 (1998).
[29]I. Horcas, R. Fernandez, J. M. Gomez-Rodriguez, J. Colchero, J. Gomez-Herrero, and A. M. Baro, Rev. Sci. Instrum. **78**, 013705 (2007).
[30]N. Aoki, C. R. da Cunha, R. Akis, D. K. Ferry, and Y. Ochiai, Phys. Rev. B **72**, 155327 (2005).
[31]M. T. Woodside, C. Vale, P. L. McEuen, C. Kadow, K. D. Maranowski, and A. C. Gossard, Phys. Rev. B **64**, 041310(R) (2001).
[32]M. A. Topinka, B. J. LeRoy, R. M. Westervelt, S. E. J. Shaw, R. Fleischmann, E. J. Heller, K. D. Maranowskik, and A. C. Gossard, Nature (London) **410**, 183 (2001).
[33]G. A. Steele, R. C. Ashoori, L. N. Pfeiffer, and K. W. West, Phys. Rev. Lett. **95**, 136804 (2005).
[34]T. Machida, H. Hirai, S. Komiyama, T. Osada, and Y. Shiraki, Phys. Rev. B **54**, 14261 (1996).

3.3 Non-homogeneous Magnetic Fields and Mixing of Spin-Resolved Edge Channels

As detailed in Sections 1.2.2, in order to induce any mixing between spin-resolved edge channels, we need some mechanism of coupling with the spin degree of freedom, such as spin-orbit effect or local non-perpendicular magnetic fields (see Eq.(1.13)).

The former is an intrinsic effect of 2DEGs based on GaAs, but it is very weak and it is hard to control for IQH edge states [51].[12] The latter is instead within the reach of nanotechnology: mesoscopic magnetic gates can be fabricated on the top of the heterostructure [77], so to produce in the 2DEG weak magnetic fields in the x and y direction.

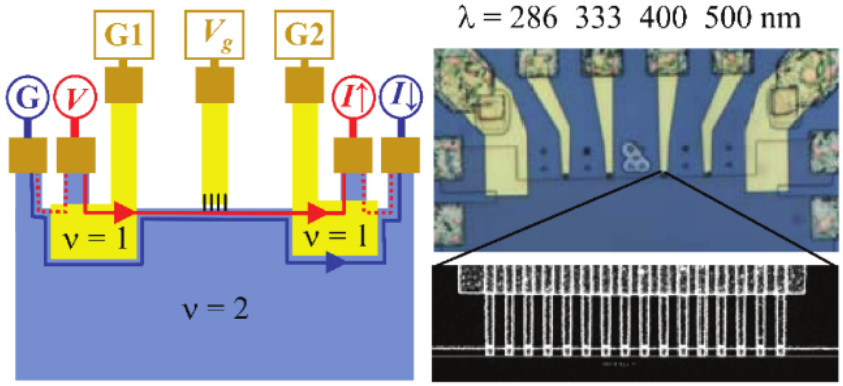

Figure 3.8: **Left panel**: pictorial view of the measurement setup. The outer ES is plotted as a blue line, the inner ES (which is biased at voltage V) is plotted in right. G_1 and G_2 are two gates used for the cross-gate technique, and a single array of fingers is drawn (at voltage V_G) **Right panel:** actual optical microscopy view of the nano-device, where the transport channel is interrupted by four independent finger arrays .The distance λ between the fingers in each array corresponds also to the width of each individual nanomagnet.

In order to test the *periodic poling* mixing strategy described in section 2.2.3, and thus being able to build a proper beamsplitter for co-propagating spin-resolved edge states, experimentalists managed to fabricate several arrays made of many equally spaced magnetic *fingers* (see Fig.3.8 for details) individually made by a ferromagnetic metal (Cobalt) on top of a 2DEG. Each array is defined by the periodicity of its modulation λ and consists of a number N of nanomagnets such that $N\lambda \simeq 6\mu m$. The arrays are independent since they are spaced apart several tens of micrometers, and can be individually deactivated by applying a large negative voltage on the fingers (see section 3.3.1).

When an array is activated, electronic transport along the edge channels is influenced by the local *fringing* field generated by this set of nanomagnets, which provides a non-negligible in-plane component of the global magnetic field $\vec{B}$, as discussed in the next paragraph. As in the experiment described in Section 3.2, the spin-resolved ES can be individually populated and measured with the cross-gate technique (see Section 1.3), so that the charge transfer between the channels can be measured as excess current carried on the outer/inner ES.

[12] Indeed there is experimental evidence that magnetic impurities are the dominant mechanism for equilibration in spin-resolved ES [78]

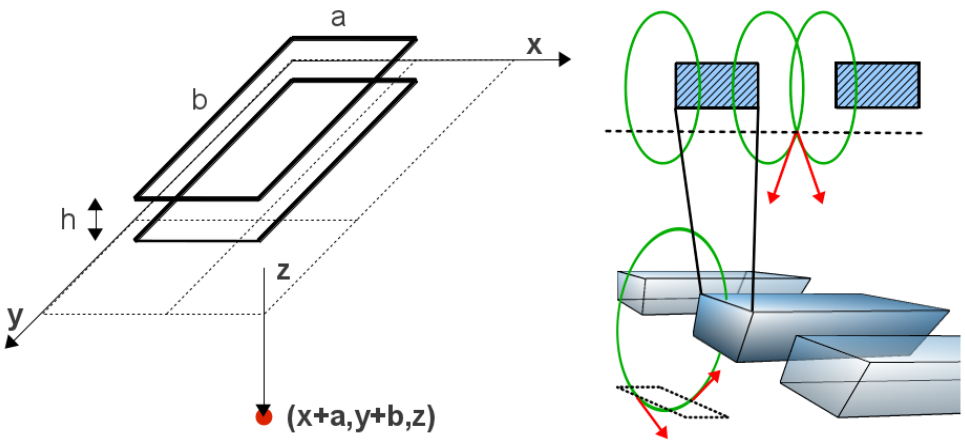

Figure 3.9: **Left panel:** scheme for calculation of the magnetic field of Cobalt fingers (Reference to Eqs.3.15-3.18). **Right panel:** pictorial view of the two components of the fringing field. Dashed rectangles are meant to be section (in the z-x plane) of the Cobalt finger.

Fringing field of Cobalt magnetic fingers We can approximate the magnetic field generated by a single magnetic finger as that of an equivalent orthorhombic structure lying over the mesa for half its length. Due to the linearity of Maxwell's equation, we can compute the field generated by a rectangular magnetized sheet (extending by a in x direction, and by b in the y direction, and with uniform magnetization M is taken to be in the z direction) as sum of contributions of rectangular regions where the magnetostatic field has simple analytical solution ([75] and see Fig.3.9). If z_0 is the distance of the magnetic sheet from the 2DEG, we have[13]

$$\begin{aligned} B^{sheet}_{i=x,y,z}(x,y,z_0) &= \mathcal{B}^s_i(\frac{a}{2}+x, b+y, z_0) + \mathcal{B}^s_i(x-\frac{a}{2}, y, z_0) + \\ &- \mathcal{B}^s_i(x-\frac{a}{2}, b+y, z_0) - \mathcal{B}^s_i(\frac{a}{2}+x, y, z_0) \end{aligned} \tag{3.15}$$

$$\mathcal{B}^s_x(a,b,z) = \frac{M}{4\pi}\ln\left(\frac{\sqrt{a^2+z^2}}{z}\frac{\sqrt{b^2+z^2}+b}{\sqrt{a^2+b^2+z^2}+b}\right) \tag{3.16}$$

$$\mathcal{B}^s_y(a,b,z) = \frac{M}{4\pi}\ln\left(\frac{\sqrt{b^2+z^2}}{z}\frac{\sqrt{a^2+z^2}+a}{\sqrt{a^2+b^2+z^2}+a}\right) \tag{3.17}$$

$$\mathcal{B}^s_z(a,b,z) = -\frac{M}{4\pi}\arcsin\left(\frac{ab}{\sqrt{(a^2+z^2)(b^2+z^2)}}\right) \tag{3.18}$$

The magnetic field generated by a solid finger of cobalt of height h can be modeled then as $B_i(x,y,z_0) = B^{sheet}_i\left(x,y,z_0+\frac{h}{2}\right) - B^{sheet}_i\left(x,y,z_0-\frac{h}{2}\right)$ (see Fig.3.10).

The case of an infinitely long finger in the y direction ($b\to\infty$) is a good approximation for the field on the region far away from the edge of fingers (see Fig.3.11c). In this region the magnetostatic field has then zero B^∞_y component, while the other transverse component, for $a=\lambda$, reads [76]

$$B^\infty_x(x) = \frac{M}{4\pi}(\ln\left[\frac{(x+\frac{\lambda}{2})^2+(z+\frac{h}{2})^2}{(x+\frac{\lambda}{2})^2+(z-\frac{h}{2})^2}\right] - \ln\left[\frac{(x-\frac{\lambda}{2})^2+(z+\frac{h}{2})^2}{(x-\frac{\lambda}{2})^2+(z-\frac{h}{2})^2}\right]). \tag{3.19}$$

[13]The saturation magnetization of Cobalt at low temperature is about $1.8T$ [76].

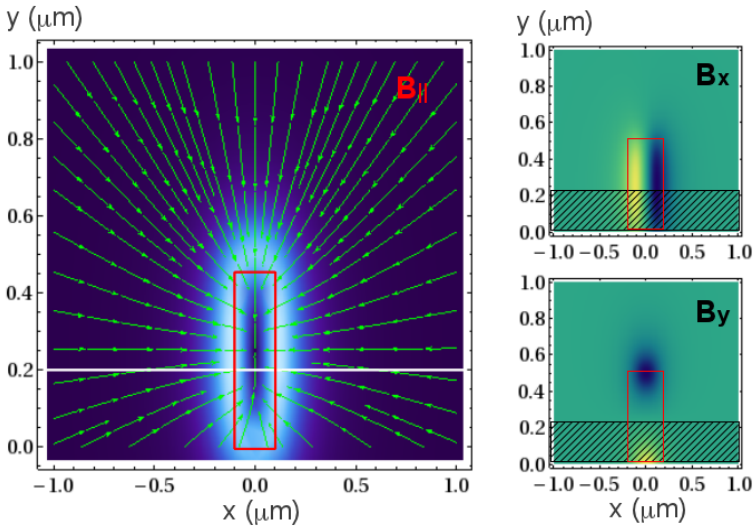

Figure 3.10: Vector plot of the $B_{\parallel}$ magnetic field generated by one magnetic finger. **Left panel:** vector field B_x+B_y projected on the 2DEG. **Right panel:** individual contributions of both component of the vector field. The rectangular projection of the magnetic finger ($a = 0.2\mu m$, $b = 0.5\mu m$, $h = 0.12\mu m$, $z = 0.16\mu m$) is shown in red. For transport models, it should be considered that the finger extends beyond the mesa (shaded zones in right panels and region under the white line in left panel).

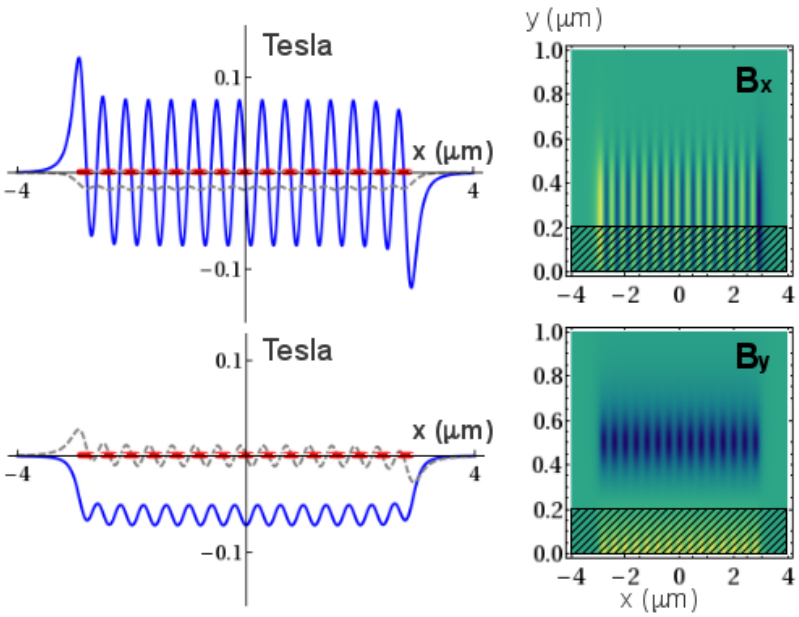

Figure 3.11: In-plane magnetic field generated by 15 cobalt fingers extending on the mesa for 50 nm, with a periodic spacing of $\lambda = 400$ nm. **Top left panel:** magnetic field profile for B_x (blue line) compared to B_y (dashed gray) calculated 10 nm from the edge of the mesa. Red markers indicate regions covered by the fingers. **Bottom left panel:** magnetic field profile calculated at 20 nm after the end of the rectangular fingers on the mesa. B_y (blue line) is now bigger than B_x (gray dashed line). **Right panels**: density plots of B_x and B_y for the considered finger array.

We can then easily compute the total transverse field generated by a complete set of N magnetic fingers, seen by electrons which are transmitted in regions under the array or just outside the array (See Fig.3.11).[14]

Not considering the small intensity variations and the effects at the beginning and at the end of the array, the magnetic modulation under the finger goes as[15]

$$B_{\parallel} \simeq B_x^{\infty}(x) \simeq B_{\parallel}^0 \sin\left(\frac{2\pi x}{\lambda}\right) , \tag{3.20}$$

while the modulation in the region outside the finger arrays takes the form

$$B_{\parallel} \simeq B_y(x) \simeq B_{\parallel}^0 + \delta B_{\parallel} \cos\left(\frac{2\pi x}{\lambda}\right) , \tag{3.21}$$

where $B_{\parallel}^0$ is of the order of $0.05T$ and $\delta B_{\parallel}$ considerably smaller as shown in Fig.3.11.

3.3.1 Coherent Mixing of Spin-Resolved Channels

According to the Born approximation, we can estimate the effect of the transverse potential in order to induce coherent mixing as described in Section 2.2.3.

Being the field of sinusoidal form (3.20)-(3.21), the transmission coefficient $|t_{12}|^2$, approximated by Eq.(2.11) has a peak for resonant periodicity λ (2.10). We performed numerical simulations by modeling a four-terminal device (see Fig.3.12, upper panel. See also Appendix I on page 87) with magnetic fingers of different spacings and varying the effective strength of $B_{\parallel}$. The simulation results confirm that the non-perturbative solution of the scattering problem maintains the qualitative features described by Eq.(2.11).

As already discussed in the previous section, the tight-binding numerical model is also very well suited to study the impact of random inhomogeneities in the system such as magnetic disorder or imperfections in the finger spacings. We introduced in the simulations different types of disorders, such as local random variations of the Zeeman energy in each site, as well as uncertainties on the finger width, spacing and intensities. As long as the average value of fluctuating parameters is the same as the value of reference of the non-averaged simulation, all resonance patterns obtained proved very similar to the ideal case, unless the fluctuations were so huge as to destroy completely the regularity of the device. In the coherent non-interacting limit, this result provides confidence that static-disorder cannot realistically introduce qualitative variations upon our result.

In Fig.3.12 we also present the results of the experiment for the mixing of the channels under the action of a single array of fingers separated by λ=200 nm, 286 nm, 333 nm, 400 nm, 500 nm.[16]

We observe non-zero values of the transfer current for the arrays corresponding to $\lambda = 400$ and $\lambda = 500$. It should be noted that such a non-monotonic dependence in periodicity is necessarily a proof that a coherent effect (such as the one described in our model) is acting. Indeed as shown for the mixing model in Section 2.2.1, the concatenation of several weak mixers provide a "classical" linear amplification of the mixing,

[14] The in-plane field varies in a range of about 0.1T, so the mutual dipolar interaction between the finger is negligible compared to the magnetization imposed by the large external field B_z.

[15] We should note that there is also a periodic contribution of the perpendicular component $B_z^{\infty}(x)$. Its contribution adds up to the Zeeman term of the Hamiltonian and can influence locally the wave-number separation Δk . The variation of the Zeeman energy due to this field is however so tiny (μeV) that its effect can be neglected in first approximation (See Section 1.13).

[16] In the simulations we can arbitrarily vary λ by performing different runs, each with a spacing differing up to the lattice step a. At the contrary, in the experiments each λ corresponds to a different previously nano-fabricated device

unless a precise control of the phases accumulated between the scattering centers is achieved. In the framework of the previously described periodic poling effect, this result hints at a coherent resonance with a maximum intensity lying between $\lambda = 400$ and $\lambda = 500$. This is reproduced in our simulations by fixing the effective[17] $g - factor$ to be about 1.8, which sets the resonant $\Delta k = 2\pi\lambda^{-1} = 13.8\ \mu m^{-1}$.

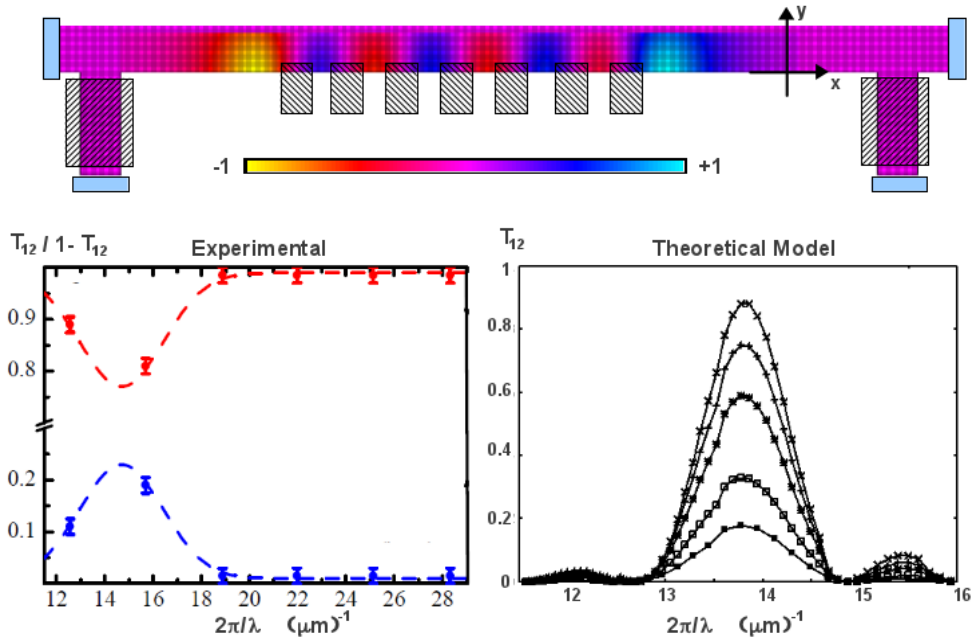

Figure 3.12: **Top panel**: example of a simulated Hall bar with seven fingers, where the color density corresponding to $|B_x|$ is plotted in color-code (see also Fig.3.11). **Bottom left panel**: Experimental results demonstrating the selectivity of the engineered charge transfer with respect to λ. The dashed line represents a guide to the eye indicating a resonance occurring for a periodicity in between $\lambda = 500$ nm and $\lambda = 400$ nm **Bottom right panel**: theoretical resonance pattern from RGF calculations, for different values of $\left|B_{\|}\right|$ (from $B_{\|} \simeq B_z/100$ to $B_{\|} \simeq B_z/5$). The qualitative shape of the resonance is consistent with first order perturbation theory (see Section 2.2.3).

If the resonance is ultimately due to the periodic poling effect, the experimental findings seem to indicate the presence of a large broadening of the theoretical resonant peak. Indeed in the real experiment we expect the situation to be complicated by dephasing effects (temperature, phonon emission, structured magnetic impurities), and elastic/inelastic influence of Coulomb interactions. The main contribution of these neglected effects will be both to renormalize the parameters (as it is the case of the inclusion of the renormalized $g^\star$ approach, discussed in Section 1.2.2) or to blur the interference effects, such to produce the observed broadening.

Electric Potential Effect and Magnetic Mixing The Cobalt nanomagnets are metallic bars that can be electrostatically polarized. The applied voltage V_G will influence the 2DEG under the fingers, and it is reasonable to assume that the nanomagnets will

[17] Experimental results about the temperature-dependence of the channel equilibration also confirm that the effective spin-gap at the edge is much higher than the bare one (see our paper at the end of the Chapter for the measurements).

act as top gates as described in Section 1.3.3. The band lifting triggered by increasing voltage on the fingers will influence the spatial arrangements of the channels and will eventually completely expel them from the finger region.

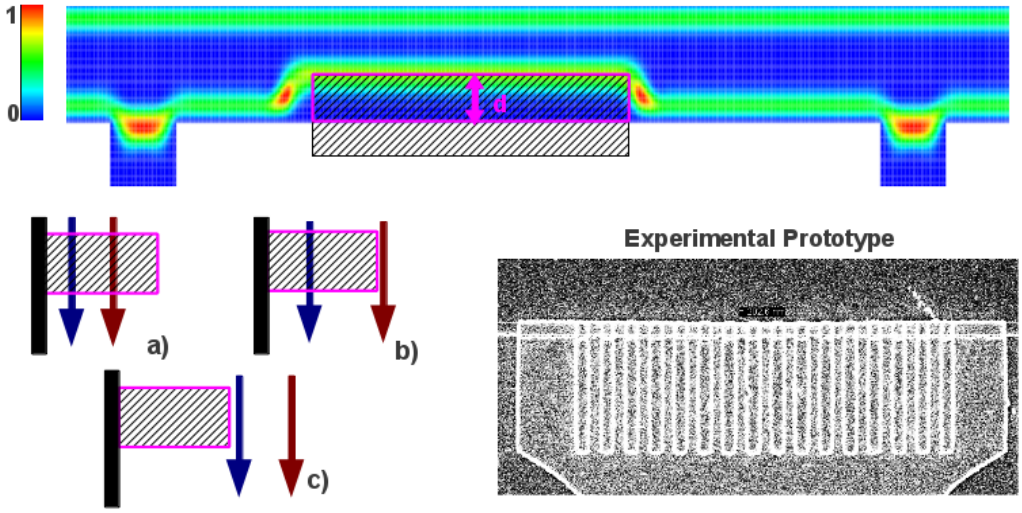

Figure 3.13: **Top panel**: planar plot of the charge density of the outer edge channel expelled by a large gate region extending on the mesa by the length d on a simulated Hall bar (high V_G case). **Left bottom panel**: a) at small V_G, the ES are expected to propagate under the gate region. b) there is an intermediate value of V_G for which one edge channel is expelled from the gate region (i.e. case (c)) and one still propagates under (see also section 1.3.3) **Right bottom panel**: Scanning-Electron-Microscopy image of an experimental device consisting of a large top-gated region of gold under which magnetic fingers of cobalt are fabricated.

Still disregarding the Coulomb interactions, we can identify two main effects which play a role in the channel mixing with the application of gate voltage:

- The *local* mixing **magnetic field** B_x and B_y depends strongly on the path taken by the edge channels, and thus on V_G.
- The *local* wave-number difference Δk (and thus the **resonance condition** Eq. (2.10)) depends on the *local* spatial separations of the channels, which depends on V_G.

The experimental results show that in the region of interest V_G influences the mixed current in a very non-linear way (See Fig.4 of the submitted paper attached at the end of the present Section). While a realistic modeling of the experiment would imply to consider the exact finite-range electric potential generated by the Cobalt fingers we can discuss some properties of idealized models in order to understand the appearance of multiple resonances in the experimental results.

In Fig.3.14 we show the local Δk defined between two ES under an extended gate region of finite transverse extension (the finger is considered to be translational invariant in the y direction, for this reason we will refer to the wave-number separation as Δk^{∞} for this model). This long gate is considered to be deposited *over* the magnetic fingers, so that the edge channel experience a periodic magnetic modulation *and* a uniform electrostatic potential in the propagation direction. Transport in such a device has not been experimentally tested yet at the time of writing, however the first prototypes have already been fabricated (see Fig.3.13).

On the lattice, we approximate the effect of increasing V_G by increasing rigidly the local onsite energy under the gate regions, so that there is a maximum in $\Delta k^{\infty}(V_G)$ corresponding to the situation where the outer ES is completely expelled from the finger region while the inner ES is still energetically allowed to lie under the finger. At high voltage the simple model predicts that both ES are expelled. The applied gate voltage provides a strong confinement potential comparable to the impenetrable hard wall at the end of the lattice, so that $\Delta k^{\infty}(V_G \gg 1) \simeq \Delta k^{\infty}(0)$.

We immediately see in this simple uniform model that, depending on the characteristics of the gate and the spacing of the fingers, the resonance conditions Eq. (2.10) can be met for different values of V_G. This is clarified in Figure 3.14, where we calculate the transfer current as a function of V_G for different periodicity of the magnetic fingers, and we explicitly show that peaks occur[18] where $\Delta k(V_G)$ meets the resonant condition Eq.2.10.

In the performed experiment, the actual electric field generated by the Cobalt fingers is not uniform, but it is periodic with the same periodicity as $B_{\|}$. Experimentalists are also able to vary the external perpendicular magnetic field B_z and so to map the full dependence of the transferred current for a given array of fingers as a function of B_z and V_G. Increasing B_z is expected to influence the overlap of the wavefunctions (see Fig. 1.3 in Section 1.2.2) and in general to increase the coherence of the ES.[19]

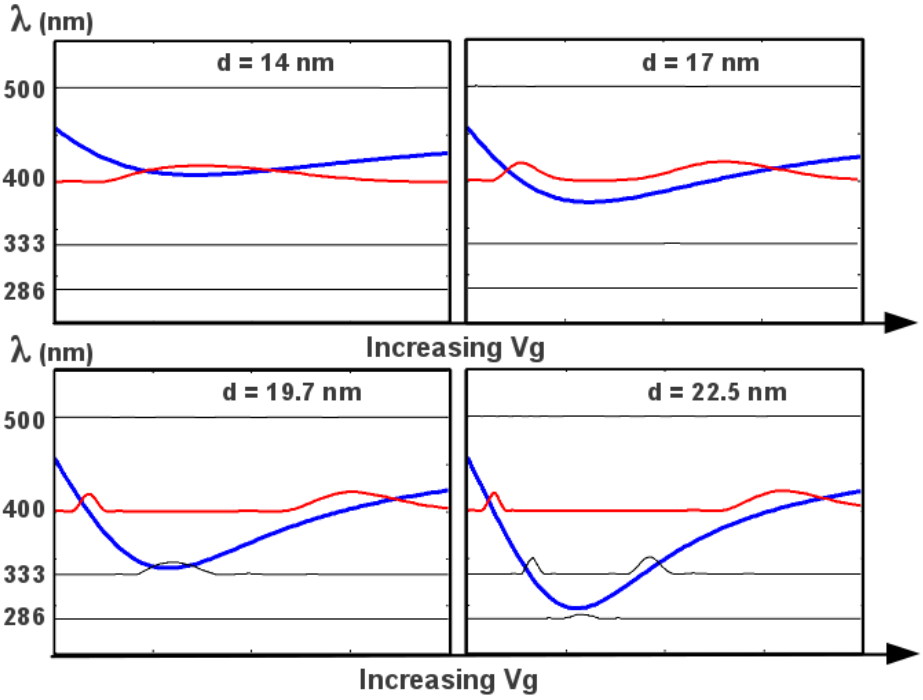

Figure 3.14: The appearance of multiple resonances while increasing V_G, for different devices. Horizontal lines in each panel represent current signals (in a rescaled notation) for the transfer current for nanoarrays of different λ (the red line corresponds to the transfer current for $\lambda = 400$ nm). The blue curve represents the resonance condition $\lambda = 2\pi/\Delta k$ computed for $\Delta k = \Delta k^{\infty}(V_G)$. Different panels correspond to different lengths d of the top gate (see Fig.3.13).

[18] all curves show several multiple resonance which are invisible at the present scales since they represent the effect of secondary peaks of the interference pattern whose mixing is $\lesssim 0.01\%$

[19] It is an experimental fact that in MZI the visibility of oscillations generally increase as B_z increases [79].

Following the semi-classical picture where the edge states are considered to adiabatically follow the equipotential lines (Section 1.3.3) we can define a periodic local wave-number $\bar{k}_i(B_z) + k_i\left(x, V_G, B_z\right)$ for each channel[18]. Eq.(2.11) becomes

$$t_{12} \propto \mathcal{M}\left(V_G, B_z\right) \int_0^L e^{i\Delta\bar{k}(V_G,B_z)x} e^{i\phi(x,V_G,B_z)} B_{\|}\left(V_G, x, B_z\right) dx \ , \tag{3.22}$$

where $\phi(x, V_G, B_z) = \int_0^x \left[k_1\left(\xi, V_G, B_z\right) - k_2\left(\xi, V_G, B_z\right)\right] d\xi$ is a monotonically increasing function representing the phase accumulated thanks to local variation of the potential with respect to the translational invariant phase. We are thus introducing a new important periodicity in the transition amplitude: the period p for which $\phi(x+p, V_G, B_z) = \phi(x, V_G, B_z)+2\pi$. The dependence on the parameters of $\phi(x, V_G, B_z)$ is highly non-trivial, but preliminary investigations on simple models (such as the one just presented in Fig. 3.14 which consists in $\phi = 0$ and $\Delta\bar{k} = \Delta k^{\infty}(V_G)$) are all consistent with the appearance of multiple resonances. Further research is in progress in order to shed light on the interplay and influence of B_z and V_G in the current signal for understanding experimental results.

Controlled coupling of spin-resolved quantum Hall edge states

Biswajit Karmakar[1], Davide Venturelli[1,2,3], Luca Chirolli[1], Fabio Taddei[1], Vittorio Giovannetti[1], Rosario Fazio[1], Stefano Roddaro[1], Giorgio Biasiol[4], Lucia Sorba[1], Vittorio Pellegrini[1], and Fabio Beltram[1]
[1]*NEST, Scuola Normale Superiore and Istituto Nanoscienze-CNR, Piazza San Silvestro 12, I-56127 Pisa, Italy,*
[2]*Institut NEEL, CNRS and Université Joseph Fourier, Grenoble, France,*
[3]*International School for Advanced Studies (SISSA), Via Bonomea 265, I-34136 Trieste, Italy,*
[4]*Istituto Officina dei Materiali CNR, Laboratorio TASC, Basovizza (TS), Italy.*
(Dated: September 27, 2011)

We introduce and experimentally demonstrate a new method that allows us to controllably couple co-propagating spin-resolved edge states of a two dimensional electron gas (2DEG) in the integer quantum Hall regime. The scheme exploits a spatially-periodic in-plane magnetic field that is created by an array of Cobalt nano-magnets placed at the boundary of the 2DEG. A maximum charge/spin transfer of $28 \pm 1\%$ is achieved at 250 mK.

PACS numbers: 73.43.-f, 03.67.-a, 72.25.Dc, 72.10.-d

Topologically-protected edge states are dissipationless conducting surface states immune to impurity scattering and geometrical defects that occur in electronic systems characterized by a bulk insulating gap [1]. One example can be found in a clean two-dimensional electron gas (2DEG) under high magnetic field in the quantum Hall (QH) regime [2]. In the integer QH case, spin-resolved edge states (SRESs) at filling fraction $\nu = 2$ (number of filled energy levels in the bulk) are characterized by very large relaxation [3] and coherence [4] lengths. This system is a promising building block for the design of coherent electronics circuitry [4–8]. It represents also an ideal candidate for the implementation of dual-rail quantum-computation architectures [9] by encoding the qubit in the spin degree of freedom that labels two distinct co-propagating, energy-degenerate SRESs of the *same* Landau level (LL) at the *same* physical edge of the 2DEG [10]. A key element for the realization of such architecture [10–12] is a coherent beam splitter that makes it possible to prepare any superposition of the two logic states, thus realizing one-qubit gate transformations. This requires the ability to induce controlled charge transfer between the two co-propagating SRESs, a goal which up to date has not been yet achieved. Here we solve the problem by targeting a resonant condition, in analogy with the periodic poling technique adopted in optics [13].

In the integer QH regime the SRESs are single-particle eigenstates $\psi_{nks}(x,y) = |s\rangle\ e^{ikx}\ \chi_{nk}(y)/\sqrt{L}$ of the Hamiltonian $H = (\mathbf{p} + e\mathbf{A})^2/2m^* + V_c(y) - \frac{1}{2}g^*\mu_B B\sigma_z$ which describes a 2DEG in the (x,y)-plane, subject to a strong magnetic field B in the z-direction and confined transversely by the potential $V_c(y)$ [14]. Here $\mathbf{p} \equiv (p_x, p_y)$ and $\vec{\sigma} \equiv (\sigma_x, \sigma_y, \sigma_z)$ are respectively, the particle momentum and spin operators, $\mathbf{A}$ is the vector potential, L is the longitudinal length of the Hall bar, while m^* and g^* are the effective electron mass and g-factor of the material. Each $\psi_{nks}(x,y)$ represents an electron state of the nth LL with spin projection $s \in \{\uparrow, \downarrow\}$ along z-axis, which is characterized by a transverse spatial distribution $\chi_{nk}(y)$, and which propagates along the sample with longitudinal wave-vector k. In our analysis we will focus on a $\nu = 2$ configuration, where the longitudinal electron transport occurs through the SRESs of the lowest LL, i.e. $\Psi_\uparrow \equiv \psi_{0,k_\uparrow,\uparrow}(x,y)$ and $\Psi_\downarrow \equiv \psi_{0,k_\downarrow,\downarrow}(x,y)$ (the values $k_\uparrow, k_\downarrow$ being determined by the degeneracy condition at the Fermi energy $E_F = \epsilon_{k_\uparrow} = \epsilon_{k_\downarrow}$ of the corresponding eigenenergies). Specifically in our scheme the two SRESs are separately contacted, grounding $\Psi_\downarrow$ and injecting electrons on $\Psi_\uparrow$ via a small bias gate V. The spin resolved currents $I_\uparrow$ and $I_\downarrow$ of the two SRESs are then separately measured at the output of the device, after an artificial charge transfer from $\Psi_\uparrow$ to $\Psi_\downarrow$ is induced during the propagation. Since in general $\Delta k \equiv k_\uparrow - k_\downarrow \neq 0$, $\Psi_\uparrow$ and $\Psi_\downarrow$ support electrons at different wave vectors. Hence any external perturbation capable of inducing charge transfer between them must both flip the spin *and* provide a suitable momentum transfer to match the wave-vector gap Δk. In our scheme we achieve this by introducing a spatially-periodic in-plane magnetic fringing field $\vec{B}_\parallel(x,y)$ [15] generated by an array of Cobalt nanomagnet (*magnetic fingers*) placed along the longitudinal direction of the 2DEG, see Fig. 1a. The system Hamiltonian acquires thus a local perturbation term $\Delta H = -g^*\mu_B \vec{B}_\parallel(x,y)\cdot\vec{\sigma}/2$, which at first order induces a transferred current $I_\downarrow = (e^2V/h)|t_{\uparrow\downarrow}|^2$, where $t_{\uparrow\downarrow} = (L/i\hbar v)\langle\Psi_\downarrow|\Delta H|\Psi_\uparrow\rangle$ is the associated scattering amplitude, and v is the group velocity of the SRESs. To capture the essence of the phenomenon, consider for instance an array of periodicity λ and longitudinal extension ΔX described by a $\vec{B}_\parallel(x,y)$ field of the form $B_y(y)\cos(2\pi x/\lambda)\hat{y}$ for $x \in [-\Delta X/2, \Delta X/2]$ and zero otherwise (here for simplicity x and z component of $\vec{B}_\parallel$ have been neglected). The corresponding transmission amplitude computed at lowest order in the T-matrix expansion [16] is

$$t_{\uparrow\downarrow} = ig^*\mu_B\langle B_y\rangle\tfrac{\Delta X}{4\hbar v}\ \mathrm{sinc}[(2\pi/\lambda - \Delta k)\Delta X/2]\ , \quad (1)$$

with $\mathrm{sinc}[\cdot] \equiv \sin[\cdot]/[\cdot]$ being the sine cardinal function and $\langle B_y\rangle \equiv \int dy B_y(y)\chi_{0,k_\uparrow}(y)\chi_{0,k_\downarrow}(y)$. The ex-

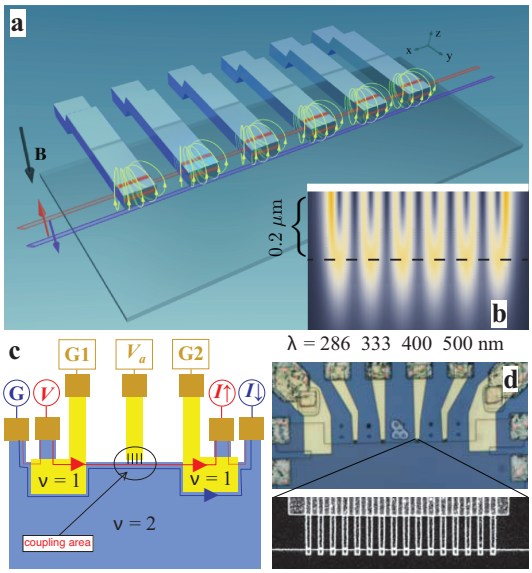

FIG. 1: (Color online) a) Schematics of the device. The Cobalt fingers (blue bars) produce a fringing field (yellow lines) resulting in an in-plane, oscillatory, magnetic field $\vec{B}_\parallel$ at the level of the 2DEG (textured gray) residing below the top surface. The field induces charge transfer between the spin up $\Psi_\uparrow$ SRES (red line) and spin down $\Psi_\downarrow$ SRES (blue line). b) Density plot of the modulus $\vec{B}_\parallel$ in the proximity of the magnetic fingers on 2DEG plane. The dashed line indicates the end of the finger array at 0.2 μm from the physical edge of the mesa (white stripe). c) Measurement set-up: The $\Psi_\uparrow$ channel is excited by a bias voltage V, while $\Psi_\downarrow$ is grounded at the contact denoted by G. The SRESs can be reversibly decoupled by negatively biasing the array with a voltage V_a (G1 and G2 are contacts for the top gates). d) Optical image of the device showing four sets of magnetic fingers with different periodicity λ placed serially at the mesa boundary (the yellow elements are gold eletrical contacts). Zoomed region is the scanning electron microscopic image of the array of periodicity $\lambda = 400$ nm: it is nearly 6 μm long and has an overlap on the mesa of 0.2 μm.

pression clearly shows that even for small values of longitudinal field a pronounced enhancement in inter-edge transfer occurs when λ matches the wave-vector difference of the two SRESs (i.e. $\lambda_{res} = 2\pi/\Delta k$), the width of the resonance being inversely proportional to ΔX.

The quantity Δk that defines the resonant condition depends on the Zeeman energy gap and on the details of the confinement potential $V_c(y)$. An estimate based on numerical simulations (see Supplemental Material (SM)) leads to an approximate value $\lambda_{res} \approx 400$ nm at B = 4.5 T, which we assumed as a starting point in designing our setup. The device was fabricated on one-sided modulation-doped AlGaAs/GaAs heterostructure grown by molecular beam epitaxy. The 2DEG resides at the AlGaAs/GaAs heterointerface located 100 nm below the top surface. A spacer layer of 42 nm separates the 2DEG from the Si δ-doping layer above it. The 2DEG has nominal electron density of $2 \times 10^{11}/\mathrm{cm}^2$ and low-temperature mobility nearly 4×10^6 Vcm/s. The Cobalt nano-magnet array was defined at the mesa boundary of the 2DEG using e-beam lithography and thermal evaporation of 10 nm Ti followed by 110 nm Co. Eight nano-magnet arrays at different periodicities (specifically $\lambda = 500, 400, 333, 286, 250, 222, 200$ and 182 nm) were fabricated, keeping the total spatial extension of the modulation region nearly constant, $\Delta X \simeq 6.2$ μm (four of them are on the other side of the mesa and therefore not visible in the microscope image of Fig. 1 d). The magnetization of the Cobalt fingers is aligned along the applied perpendicular magnetic field B (Fig. 1a), if B is large enough [15]. The actual value of the oscillatory $\vec{B}_\parallel$ can reach 50 mT in the proximity of the fingers and it decays away from the array (see Fig. 1b). Importantly, coupling between the SRESs and a chosen set of fingers can be activated by increasing the voltage bias V_a of the array from -3 to 0 V (Fig. 1c), while keeping all other arrays at $V_a = -3$ V. In these conditions, the SRESs are brought close to the selected array only and exposed to its oscillatory in-plane field $\vec{B}_\parallel$. Transport measurements were carried out in a He3 cryo-system with a base temperature of 250 mK equipped with 12 T superconducting magnet. An ac voltage excitation of 25.8 μV at 17 Hz was applied to the electrode V of Fig. 1 c) and the transmitted current was measured by standard lock-in techniques using current to voltage preamplifiers.

We first measured the two-terminal magneto-current at $T = 250$ mK in order to locate the plateau associated with a number of filled LLs in the bulk ν equal to 2 (see Fig. 2a). The working point was set in the center of the plateau, i.e. at $B = 4.75$ T. The two SRESs can be separately contacted as schematically shown in Fig. 1c by negatively biasing the gates G1 and G2 at a voltage V_G^*, such that the filling factor below the corresponding top gates becomes $\nu = 1$ and one edge channel only is allowed underneath the gates. The actual V_G^* value can be determined by measuring the currents $I_\uparrow$ and $I_\downarrow$ as a function of V_G (see Fig. 2b). When inter-edge coupling is suppressed by applying $V_a = -3$ V to all the nanofingers, we find that spin up electrons are entirely transmitted (yielding a current $I_\uparrow$ of about 1 nA, as expected for a single channel of unit quantized resistance $h/e^2 \approx 25.8$ KΩ), while the spin down current $I_\downarrow$ is nearly zero for $V_G^* = -0.47 \pm 0.08$ V (see Fig. 2b). In agreement with [3], this implies the absence of significant spin flip processes over the distance of about 100 μm traveled by the co-propagating SRESs when the magnetic fingers are deactivated. For completeness, Fig. 2c shows the dependence of the currents $I_\uparrow$ and $I_\downarrow$ on temperature: SRESs fully relax only for $T \sim 1.6$ K (i.e. $1/(k_B\mathrm{T}) \approx 7.2$ meV^{-1}), while edge mixing becomes negligible at our working point $T = 250$ mK. Moreover, analyzing our data as in

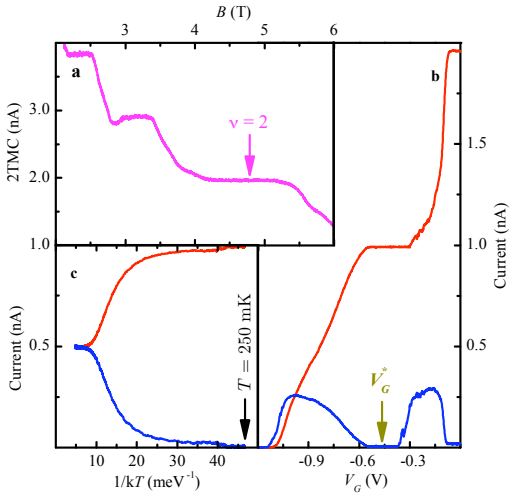

FIG. 2: (Color online) a) Plot of the two terminal magneto-current (2TMC) measured at 250 mK. The value of magnetic field $B = 4.75$ T, indicated by an arrow, is used to place the 2DEG approximately at the center of the $\nu = 2$ plateau. b) Plot of the currents $I_\uparrow$ (red) and $I_\downarrow$ (blue) measured at the current terminals red and blue respectively (Fig. 1c) with the voltage V_G applied to the gates G1 and G2, while the nano-magnets are deactivated by applying a voltage bias of $V_a = -3$ V to all the arrays. The value of V_G is set to V_G^*, indicated by an arrow, for separately contacting the spin-resolved edge states (see Fig. 1c). c) Temperature dependence of $I_\uparrow$ (red) and $I_\downarrow$ (blue) currents shows enhancement of relaxation between SRESs with increasing temperature. Thermally mediated mixing of currents becomes negligible at $T = 250$ mK.

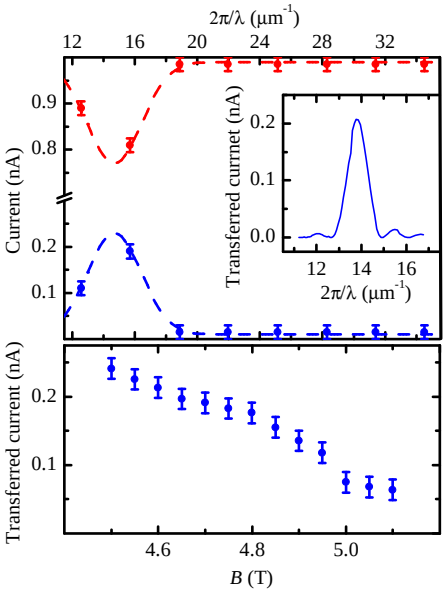

FIG. 3: (Color online) Upper panel: Plot of the transmitted currents $I_\uparrow$ (red) and transferred current $I_\downarrow$ (blue) as a function of the inverse periodicity of the activated (by applying $V_a = 0$) set of nano-fingers at the working point $B = 4.75$ T and $T = 250$ mK. The measured current $I_\uparrow$ and $I_\downarrow$ are guided by the dashed line which demonstrates selectivity of nano-magnet at periodicity between $\lambda = 400$ nm and 500 nm. The inset shows a numerical simulation of transferred current which in the absence of the static disorder and/or inelastic mechanisms predicts a width of the peak that scales inversely on ΔX as in Eq. (1). Lower Panel: measured transferred current $I_\downarrow$ as a function of the perpendicular magnetic field B for the nano-magnet array of periodicity $\lambda = 400$ nm.

Refs. [3] we can conclude that the relaxation length is of the order of 1 cm at $T = 250$ mK.

The upper panel of Fig. 3 shows the measured $I_\uparrow$ and $I_\downarrow$ when coupling occurs at several different individual arrays (one at a time) as identified by their $2\pi/\lambda$ value. Since inter-edge coupling leads to charge transfer between the two spin-resolved edge channels it results in a decrease of $I_\uparrow$, with the consequent increase of $I_\downarrow$ while the total current remains constant at about 1 nA. Note that current transfer is significant only for a specific interval of λ values: indeed a resonance peak appears to occur at λ_{res} between 400 and 500 nm. Such behavior is consistent with Eq. (1) and with a more refined theoretical analysis based on the Landauer-Büttiker transport formalism [17] which we have solved numerically in order to go beyond the result of first-order perturbation theory [18] (see inset of the upper panel of Fig. 3 and SM). Static disorder and/or inelastic mechanisms induced, e.g. by the finite temperature and Coulomb interactions, may affect the resonance, resulting in a broadening of the current peak versus $2\pi/\lambda$. Importantly, if the fingers were an incoherent series of scatterers one should expect a monotonic λ-dependence of the charge transfer [19], while the observed non-monotonic selective behavior of the current suggests an underlying constructive interference effect.

For the case of $\lambda = 400$ nm, the lower panel of Fig. 3 shows the dependence of transferred current $I_\downarrow$ on the perpendicular magnetic field B when the latter spans the $\nu = 2$ plateau (see Fig. 2a). The monotonic decrease of $I_\downarrow$ is a consequence of at least three combined effects: (i) the ratio $|\vec{B}_\parallel|/B$ decreases as B is increased, so that the net effect of the in-plane magnetic modulation is weakened; (ii) the magnetic length decreases with increasing B, causing the reduction of the spatial overlap of the transverse wavefunctions; (iii) the change of SRES spatial configuration with increasing magnetic field due to interaction effects [20, 21].

Apart from activating/deactivating the various nano-finger sets, the voltage V_a can also be used as an external control to adjust the resonant mixing condition. Figure 4 shows the measured transferred current $I_\downarrow$ as a function of V_a and B for the array of periodicity $\lambda = 400$ nm (similar data were obtained for different λ, see SM). The pronounced features present for intermediate values of V_a show that the coupling between SRESs can be controlled and amplified. Re-

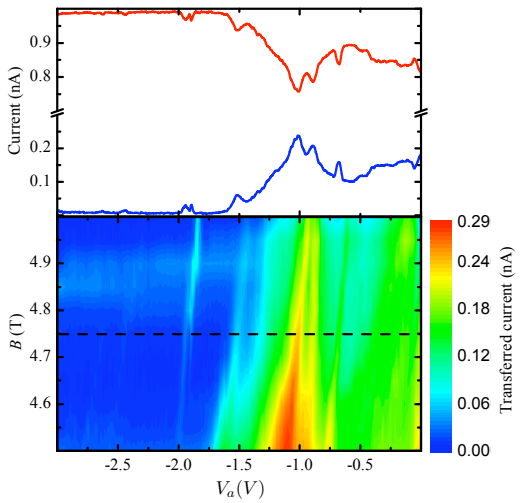

FIG. 4: (Color online) Upper panel: Dependence of the transmitted current $I_\uparrow$ (red) and transferred current $I_\downarrow$ (blue) upon the voltage V_a applied to activated nano-finger of periodicity $\lambda = 400$ nm at $B = 4.75$ T. For $V_a < -2.0$ V the fingers are effectively decoupled from the SRESs with negligible transfer current; for $V_a \simeq 0$ instead the edges feel the presence of the fingers and a non-zero transfer of current is evident. For intermediate values of V_a a series of pronounced peaks in $I_\downarrow$ are evident. Lower panel: contour plot of $I_\downarrow$ upon V_a and B for the nano-finger set of periodicity $\lambda = 400$ nm. The horizontal line indicates the center of the $\nu = 2$ plateau ($B = 4.75$ T).

markably, a charge transfer of $28 \pm 1\%$ was achieved at $B = 4.5$T with $V_a \approx -1.1$ V. At large negative V_a's the SRESs are pushed away from the region where the magnetic fringe field is present and, as expected, the coupling vanishes. The same Fig. 4 reveals additional resonances occurring at specific values of V_a. A non-monotonic dependence of the local value of Δk on V_a, can be invoked to explain these features. A system simulation shows that a local change of the confinement potential in the proximity of the associated nano-fingers modifies the relative distance of the SRESs and hence the local value of Δk in a non-monotonic way (see SM). More precisely, for low V_a the fingers act as top gates for the underlying edge states: the transverse distance between SRESs can locally increase and reach a maximum as V_a gets negative, since $\Psi_\downarrow$ and $\Psi_\uparrow$ are pushed away from the finger region, one after the other. As we further increase V_a the transverse distance between the SRESs increases again. It is worth stressing, however, that the process just described is not necessarily smooth: electron-electron interaction may in fact induce abrupt transitions in SRESs distances when the slope of the effective local potential decreases below a certain critical value which depends on the details of the sample properties [21] (also the gate voltage can influence the Fermi velocity, as shown in edge magnetoplasmons time-of-flight experiments [22]). The trajectories of SRESs are unknown and (differently from what shown in the graphical rendering of Fig. 1a) are likely to be outside the regions corresponding to the projections of the fingers when a significant voltage is applied. Nevertheless non-linear repulsive effect is expected to be effectively active in the experiment where the electrostatic potential profiles extends much beyond the length of the fingers. Moreover, the functional dependence of the potential induced by V_a upon the longitudinal coordinate x presents also an oscillatory behavior with periodicity λ. As a consequence of the adiabatic evolution of the edges, their transverse distance will also show such oscillations. A detailed modeling of the observed resonance features would require to take fully into account these effects and is beyond the scope of the present paper. However it clearly deserves further investigation as it represents a positive feature of the system, since any value of the modulation periodicity λ has typically more than one value of V_a that can fulfill the resonant condition.

Our proposal provides a way to realize beam splitters for flying qubit using topologically protected SRESs. It employs a nanofabricated periodic magnetic field operated at a resonant condition which enhances quite significantly the weak magnetic field produced by the Cobalt nanomagnets. Already at $T = 250$ mK the effect is significant and should be enhanced at lower temperatures.

This work was supported by MIUR through FIRB-IDEAS Project No. RBID08B3FM and by EU through Projects SOLID and NANOCTM. We acknowledge useful discussions with N. Paradiso and S. Heun.

[1] C. L. Kane and E. J. Mele, Phys. Rev. Lett. **95**, 226801 (2005); B. A. Bernevig, T. L. Hughes, and S. C. Zhang, Science **314**, 1757 (2006); D. Hsieh, *et al.*, Nature **452**, 970 (2008); S. Das Sarma, M. Freedman, and C. Nayak, Phys. Rev. Lett. **94**, 166802 (2005).

[2] K. v. Klitzing, G. Dorda, and M. Pepper, Phys. Rev. Lett. **45**, 494 (1980); D. C. Tsui, H. L. Stormer, and A. C. Gossard, *ibid.* **48**, 1559 (1982).

[3] G. Müller, *et al.*, Phys. Rev. B **45**, 3932 (1992); S. Komiyama, H. Hirai, M. Ohsawa, and Y. Matsuda, *ibid.* **45**, 11085 (1992).

[4] Y. Ji, *et al.*, Nature **422**, 415 (2003); I. Neder, *et al.*, Nature **448**, 333 (2007); Phys. Rev. Lett. **96**, 016804, (2006); *ibid.* **98**, 036803 (2007).

[5] P. Roulleau, *et al.*, Phys. Rev. B **76**, 161309(R) (2007); Phys. Rev. Lett. **100**, 126802 (2008); *ibid.* **102**, 236802 (2009).

[6] L. V. Litvin, H.-P. Tranitz, W. Wegscheider, and C. Strunk, Phys. Rev. B **75**, 033315 (2007); *ibid.* Phys. Rev. B **78**, 075303 (2008).

[7] S. Roddaro, *et al.*, Phys. Rev. Lett. **103**, 016802 (2009).

[8] E. Bieri, *et al.*, Phys. Rev. B **79**, 245324 (2009).

[9] I. Chuang and Y. Yamamoto, Phys. Rev. A **52**, 3489 (1995); E. Knill, R. Laflamme, and G. J. Milburn, Nature **409**, 46 (2001).
[10] V. Giovannetti, F. Taddei, D. Frustaglia, and R. Fazio, Phys. Rev. B **77**, 155320 (2008).
[11] T. M. Stace, C. H. W. Barnes, and G. J. Milburn, Phys. Rev. Lett. **93**, 126804 (2004).
[12] C. Nayak et al., Rev. Mod. Phys. **80**, 1083 (2008).
[13] M. M. Fejer, G. A. Magel, D. H. Jundt, and R. L. Byer, IEEE J. Quantum Electron. **28**, 2631 (1992).
[14] R. E. Prange, and S. M. Girvin, The Quantum Hall Effect (Springer, 1990); D. Yoshioka, The Quantum Hall Effect (Springer, 2002).
[15] A. Ursache, J. T. Goldbach, T. P. Russell, and M. T. Tuominen, J. of Appl. Phys. **97**, 10J322 (2005); J. U. Bae, *et al.*, IEEE Trans. on Magnetics **44**, No. 12 (2008).
[16] M. Di Ventra, Electrical Transport in Nanoscale Systems (Cambridge University Press, Cambridge, 2008).
[17] M. Büttiker, Phys. Rev. B **46**, 12485 (1992).
[18] K. Kazymyrenko and X. Waintal, Phys. Rev. B **77**, 115119 (2008).
[19] D. Venturelli, *et al.*, Phys. Rev. B **83**, 075315 (2011); N. Paradiso, *et al.*, *ibid.* **83**, 155305 (2011).
[20] E. Ahlswede, *et al.* Physica B **298**, 562 (2001).
[21] J. Dempsey, B. Y. Gelfand, and B. I. Halperin, Phys. Rev. Lett. **70**, 3639 (1993); L. Rijkels and E. W. Bauer, Phys. Rev. B **50**, 8629 (1994).
[22] G. Sukhodub, F. Hohls, and R. J. Haug, Phys. Rev. Lett. **93**, 196801 (2004); H. Kamata, T. Ota, K. Muraki, and T. Fujisawa, Phys. Rev. B **81**, 085329 (2010); N. Kumada, H. Kamata, and T. Fujisawa, Phys. Rev. B **84**, 045314 (2011).

4 Interactions in Spin-Resolved Transport

In this final chapter we introduce an analytical model (Chiral Tomonaga Luttinger Liquid) describing interacting spin-resolved edge states. We discuss a possible tunneling experiment where the spin-state and the energy of transported electrons can be completely filtered before and after propagating on edge channels, and we evaluate the effect of the interactions on the steady state current by means of the non-equilibrium Green's function formalism.

4.1 Effective Model of Interactions between Edge States

The analytical non-interacting model for ES used in Chapters 1-2 makes it clear that the physics of transport in edge channels is mainly one-dimensional, as the features of the models that involve the existence of a second dimension are all phenomenologically accountable in a set of parameters (wavefunction overlap integrals, effective Δk...) defined on a 1D scattering theory. We have furthermore shown that this theory is corroborated by the numerical approach used in Chapter 3, where the ES solutions completely emerge from a 2D discrete inhomogeneous Hamiltonian, yet the physics seems to be very well described by approximate phenomenological models.

The models and numerical calculations treated in the previous chapters could in principle be extended by considering the proper form and effects of many-body Coulomb interactions in the 2DEG under high magnetic fields. This is possible in 2D if we accept to work with heavy numerics [80]. For the sake of understanding the physics, what we need is an *effective* theoretical model that includes Coulomb interactions in the transport dynamics.

By always bearing in mind that the LB theory of ES transport worked spectacularly well for describing the physics of the vast majority of experiments since the discovery of IQH effect, in this section we will review the experimental and theoretical grounds about the current investigation of Coulomb interactions in edge channels, and we will motivate the choice of a 1D *Tomonaga-Luttinger* model as the framework of choice for interacting ES (at $\nu = 2$).

4.1.1 Effects of the Interactions in the IQH channels

As discussed in Section 1.1, the electron gas is completely incompressible in the bulk, as the quantum picture of a 2DEG in a strong magnetic field predicts a collapse of the continuous electronic DOS in delta peaks at Landau energies, so that the Fermi level is not pinned at $\hbar\omega_c(n + \frac{1}{2})$. An incompressible liquid does not screen interactions, so the long range character of the Coulomb potential can be neutralized mainly by the metallic surrounding. We already mentioned in Section 1.2.2 that interactions can still have a non-negligible effect at $\nu = 2$, as they influence the g-factor of the system, leading to a possibly enormous "exchange enhancement" of this constant.

At the edge of the Hall bar the situation is more complicated since the density of the electron liquid must fall to zero due to the confinement potential (or the end of the

mesa). From a purely classical electrostatic level, we can already infer that Coulomb interactions can have a dramatic effect. In their celebrated work, D. Chklovskii et al. [92] indeed observed that a mean field treatment of the interaction (Hartree potential or Thomas-Fermi theory [95]) alone is already sufficient to obtain ES which are not one-dimensional Fermi liquids, but compressible stripes of finite width[1]. This is unavoidable for smooth confinement potentials, but if the strong confinement is falling off over nanometric scales, Dempsey and Halperin [101] have first shown that this *edge reconstruction* is suppressed at $\nu = 2$, due to the exchange energy between electrons of opposites spins, which stabilizes the existence of one-dimensional channels at the edge, at a physical separation which is in general larger than the one predicted by non-interacting theory.

In addition to the possibility of changing the very nature of the ground state of edge channels, and influence all parameters relevant for LB theories such as the Fermi velocity [94], the effect of the interaction on the *dynamics* of transport in ES is even more complicated, since the electrons on the wide edge can in principle excite transverse collective modes [96], and there is no clear indication on what could be the good form and the intensity of the *effective* two-body interaction potential of propagating particles in the ES.

The Chiral Tomonaga Luttinger Model We decide to focus on interacting effective one-dimensional models, implicitly assuming either that the confinement potential is sufficiently sharp to justify narrow, incompressible ES, or that the presence of the compressible stripes does not influence strikingly the transport, which occurs at the edge of the stripes[2]. If we take the non-interacting model described in Chapter 1, and we disregard the effect of the transverse wavefunctions, we can write the Hamiltonian of the system in the second quantized notation (see Fig.4.1)[3]

$$H_0 = \sum_{\sigma} \sum_{k} \hbar v_F^{\sigma}(k - k_F^{\sigma}) c_{k\sigma}^{\dagger} c_{k\sigma} \ , \tag{4.1}$$

where $\sigma = \uparrow, \downarrow \equiv (+1, -1)$. In the following the difference between the spin-resolved wave-numbers will be denoted as $\Delta k = k_F^{\uparrow} - k_F^{\downarrow}$, and between the spin-dependent Fermi velocities as $\delta v = v_F^{\uparrow} - v_F^{\downarrow}$.

Coulomb interactions between two chiral 1D channels should add this generic term to the Hamiltonian [65]

$$H_{int} = \frac{1}{2L} \sum_{\sigma,\sigma'} \sum_{q,p} \sum_{k} [U_{\sigma\sigma'}(q,p,k) c_{q\sigma}^{\dagger} c_{p\sigma'}^{\dagger} c_{(p-k)\sigma'} c_{(q+k)\sigma}] \ , \tag{4.2}$$

where $U_{\sigma\sigma'}(q,p,k)$ represents the interaction potential between electrons projected on the same edge channel ($\sigma = \sigma'$) or on different edge channels ($\sigma = -\sigma'$).

[1] These compressible regions can indeed screen the realistic interaction of injected electrons on the channel, making the effective description of transport models even more complex.

[2] This is a strong assumption from the theoretical point of view. Many experimental facts are however supporting the view that the pinning effects due to the existence of the stripes are not extremely relevant for effective transport models (unless high-bias is concerned [132]). For tunneling contacts, a zero bias peak in the tunneling density of states is never observed, and it is expected that for transport of single-particles occurring at energies over the Fermi level, as in the setup that is described in Section 4.2.1, the unoccupied states available for transport are compatible with a 1D transport model.

[3] There are some technicalities concerning what is the physical Hilbert space of the TL model [66]. It should be noted that we are considering H_0 to be *normal ordered*, i.e. we subtract the energy of the filled Fermi sea (which is the right-mover band filled up to k_F^{σ}), which represents the vacuum of the creation/annihilation operators.

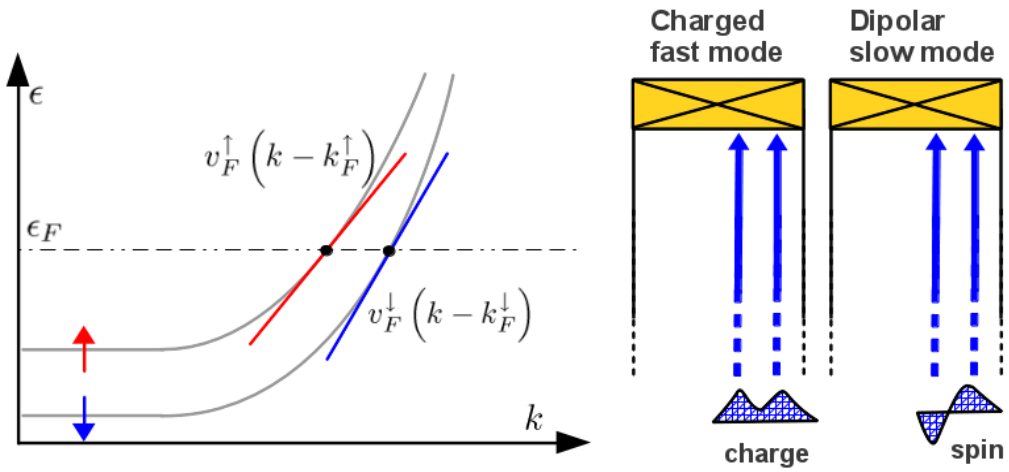

Figure 4.1: **Left panel**: schematics of the bands of the 1D model from which the chiral TL model is derived. $v_F^{\uparrow}$ and $v_F^{\downarrow}$ correspond to the two different slopes of the tangent of the bands at Fermi energy ϵ_F. **Right panel**: the eigenmodes of the chiral TL model if $v_F^{\uparrow} = v_F^{\downarrow}$: the collective charge and spin modes are delocalized on both edge channels, but one is charged and "fast" while the other is neutral and "slow" (see text).

When it comes to deal with interactions, the choice of working with 1D edge channel, from a theoretical point of view can heavily benefit of the experience maturated in the theoretical field of study of Luttinger liquid theory. Indeed it is a well known fact that the quasiparticle picture of Fermi liquid theory breaks down in one dimension for arbitrary interaction strength [82], and excitations of the Fermi sea are expressed in terms of bosonic collective charge and spin fluctuations.[4]

Following recent approaches [103, 104, 105, 106], the model defined by $H_{edge} = H_0 + H_{int}$ can be inscribed in the *Tomonaga Luttinger* (TL) model as long as we assume that the effective interaction of electrons on the ES couple charge density fluctuations, and not individual electron operators. Physically, this is the case if we are interested only in the long-wavelength properties of the system, or if the exchange of momentum occurs between states which are close to the Fermi surface (so that in the interaction potential $U_{\sigma\sigma'}(k,p,q)$ we put $q,p = k_F^{\sigma}$), or also if we approximate the interaction within the Hartree-Fock approach [97, 151].

If $\bar{\sigma} = -\sigma$, the interacting TL Hamiltonian in k-space is given by

$$H_{int}^{TL} = \frac{1}{2L}\sum_{\sigma}\sum_{q,p}[U_1(k)c_{q\sigma}^{\dagger}c_{p\sigma}^{\dagger}c_{(p-k)\sigma}c_{(q+k)\sigma} + U_2(k)c_{q\bar{\sigma}}^{\dagger}c_{p\sigma}^{\dagger}c_{(p-k)\sigma}c_{(q+k)\bar{\sigma}}] \ . \tag{4.3}$$

4.1.2 Solution of the Model through Bosonization

We can re-write the Hamiltonian Eqs.(4.1),(4.3) in terms of density operators

$$\rho_{\sigma}(k) = \sum_{q} c_{q\sigma}^{\dagger}c_{(q+k)\sigma} \ , \tag{4.4}$$

which follow a Bose statistics ($[\rho_{\sigma}(k), \rho_{\sigma'}(k')] = k\delta(k-k')\delta_{\sigma\sigma'}\frac{L}{2\pi}$) in the physical Hilbert space [84]. Due to the linear dispersion, the non-interacting part H_0 can also be written

[4] The few approaches that have been advanced [97, 110, 98] to study the effective transport model for the wide edge, are also describing the transport in terms of bosonic collective modes, and are completely compatible with the chiral Luttinger liquid picture in the zero-width limit.

in terms of these operators so that the total Hamiltonian turns out to b

$$\begin{aligned} H_{edge} &\simeq \frac{2\pi}{L}\sum_{k>0}\sum_{\sigma}\hbar v_F^{\sigma}\rho_\sigma(k)\rho_\sigma(-k) \\ &+ \frac{1}{2L}\sum_{k>0}\sum_{\sigma}[U_1(k)\rho_\sigma(k)\rho_\sigma(-k)+U_2(k)\rho_\sigma(k)\rho_{-\sigma}(-k)] \ . \end{aligned} \tag{4.5}$$

We now introduce the total charge and spin densities operators $s(k)=\frac{1}{\sqrt{2}}(\rho_\uparrow(k)-\rho_\downarrow(k))$, and $\rho(k)=\frac{1}{\sqrt{2}}(\rho_\uparrow(k)+\rho_\downarrow(k))$, and we re-express the Hamiltonian in terms of these fields by doing a canonical transformation (Bogoliubov rotation). In order to make the bosonic nature of the operators more explicit, we denote $s(k)=\sqrt{L\,|q|\,(2\pi)^{-1}}[\Theta(k)s_k+\Theta(-k)s_k^\dagger]$ and $\rho(k)=\sqrt{L\,|q|\,(2\pi)^{-1}}[\Theta(k)\rho_k+\Theta(-k)\rho_k^\dagger]$, where now the operators ρ and s obey canonical bosonic commutation rules. The Hamiltonian now takes the for

$$\begin{aligned} H &= \frac{1}{2\pi}\sum_{k>0}v_{ch}(k)k\rho_k^\dagger\rho_k+\frac{1}{2\pi}\sum_{k>0}v_{sp}(k)ks_k^\dagger s_k \\ &+ \sum_{k>0}(\hbar\delta v)k[s_k^\dagger\rho_k+\rho_k^\dagger s_k] \ . \end{aligned} \tag{4.6}$$

If $\delta v=0$ we would have already diagonalized the Hamiltonian in terms of two bosonic modes ρ and s (and that would correspond to the so-called *spin-charge separation*[5] [123, 124]). We need to implement a second rotation, defining the modes $\rho_k=A_k\cos\theta_k-B_k\sin\theta_k$ and $s(k)=A_k\cos\theta_k+B_k\cos\theta_k$ [83]. In terms of this operators, which are still fully Bosonic, for $\theta_k=\frac{1}{2}\arctan[2\delta v/(U_2(k))]$ the Hamiltonian is finally quadratic

$$H=\sum_{k>0}v_+(k)kA_k^\dagger A_k+\sum_{k>0}v_-(k)kB_k^\dagger B_k \ , \tag{4.7}$$

where the dispersion relations are

$$\boxed{v_\pm(k)=\bar{v}+\frac{U_1(k)}{\pi}\pm\frac{1}{2}\sqrt{\delta v^2+\frac{U_2(k)^2}{\pi^2}} \ ,} \tag{4.8}$$

where $\bar{v}=(v_F^\uparrow+v_F^\downarrow)/2$.

fermionic Correlators The general single-particle Green's function can be computed thanks to the Mattis-Mandelstam formula [84] applied to our quadratic Hamiltonian, which states that the fermion annihilator operator in real space can be written as[6]

$$\psi_\sigma(x)\equiv\lim_{\alpha\to0}\frac{\hat{F}}{\sqrt{2\pi\alpha}}e^{-ik_F^\sigma x}\exp[\sum_{k=0}^{\infty}\sqrt{\frac{2\pi}{kL}}e^{-\frac{\alpha k}{2}}(e^{ikx}\rho_\sigma(k)-e^{-ikx}\rho_\sigma(-k))] \ , \tag{4.9}$$

where the bosonic density operators are defined in Eq.(4.4) (and can be straightforwardly related to the eigenmode operators A, B) and the *Klein Factors* $\hat{F}$ are fermionic "dummy" operators whose role, in the limit of an infinite 1D system, is just to ensure the proper anti-commutation relations $\{\psi_\sigma(x,t),\psi_{\sigma'}(x',t)\}=\delta(x-x')\delta_{\sigma\sigma'}$.

The Ground state with respect to which we evaluate expectation values is a Fermi sea at zero temperature: $\sum_k\left\langle c_{k\sigma}^\dagger c_{k\sigma}\right\rangle=f(\epsilon)=\Theta(-\epsilon_F)$.

[5] v_{ch} and v_{sp} are the spin/charge dispersion relations, whose expression is easily deduced from the more general formula Eq.(4.8), for $\delta v=0$.

[6] Note that in this chapter, since the model is strictly 1D, the x variable will always refer to the coordinate along the direction of propagation, differently from previous chapters where the axis of propagation was the y axis.

Exploiting the Gaussian Identity valid for zero-temperature expectation values of exponential of bosonic operators $A(k)$, $A^\dagger(k)$ multiplied by c-numbers α and β,

$$\left\langle e^{\sum_k \alpha_k A^\dagger(k)} e^{\sum_k \beta_k A(k)} \right\rangle = e^{\sum_k \alpha_k \beta_k \langle A^\dagger(k) A(k) \rangle} = e^{\frac{1}{2}\sum_k \alpha_k \beta_k} \ , \tag{4.10}$$

we obtain finally [103]

$$\left\langle \psi(x,t)\, \psi^\dagger(0,0) \right\rangle = i G^{>}_{0\sigma}(x,t)\, F^{+}(x,t)\, F^{-}(x,t)\, S_\sigma(x,t) \ , \tag{4.11}$$

where we isolated the bare greater Green's function (see next Section)

$$G^{>}_{0\sigma}(x,t) = \frac{1}{2\pi} \frac{e^{ik_F^\sigma x}}{x - \bar{v}t + i0^+} \ , \tag{4.12}$$

the slow and fast mode components ($m = 1, 2$)[7]

$$F^m = \exp\left[- \int_0^\infty \frac{dp}{2p} e^{-rp} K_m(x,t) \right] \ , \tag{4.13}$$

and a "spin part" which is non-zero only if $\delta v \neq 0$

$$S_\sigma = \exp\left[-\sigma \int_0^\infty \frac{dp}{2p} e^{-rp} \sin\theta_p K_m(x,t) \right] \ , \tag{4.14}$$

where $K_m(x,t) = (e^{ip(x-\bar{v}t)} - e^{ip(x - v_m(p)t)})$, and θ_p is the Bogoliubov rotation angle used in the diagonalization of the Hamiltonian (see previous paragraph).

4.1.3 Single-Particle Green's Functions and Diagrammatics

Conventions and Useful identities for Green's Functions We start by summarizing some useful definitions and identities concerning Green's functions. In the following sections we will indicate with the calligraphed notation $\mathcal{G}$ only the Green's functions belonging to the TL-model computed in section 4.1.2, while we will use the symbol G when describing Green's functions in general.

Symbol	Green's Function Explaination
$g_{R,L}$	Detector/Injector (not spin resolved)
$G_\sigma(x_1, x_2)$	Complete, defined on the channel (interactions+reservoirs)
$\mathcal{G}_\sigma(x_1, x_2)$	Chiral Tomonaga Luttinger (only interactions)

Table 4.1: Differences between symbols used in the present non-equilibrium Green's function theory.

We already introduced in section 3.1.1 the "matrix" version of the retarded Green's function. Its corresponding definition by means of second-quantization formalism (i.e. ψ_σ are fermionic operators) is

$$G^{ret}_\sigma(x,t) = -i\Theta(t) \left\langle \left\{ \psi_\sigma(x,t), \psi^\dagger_\sigma(0,0) \right\} \right\rangle \ . \tag{4.15}$$

For non-interacting electrons the linear-dispersion model presented at the beginning of this chapter give

$$G^{ret}_{0\sigma}(x,t) = -i\Theta(t)\delta(x - v_F^\sigma \Delta t) e^{ik_F^\sigma x} \ . \tag{4.16}$$

[7] We use alternatively the continuum or the discrete version of the momentum expansion, related by $\sum_k F(k) = \frac{L}{2\pi} \int dp F(p)$. We also introduced the momentum cut-off r, which is a real positive small quantity necessary to regularize the theory. We will discuss further its role in Section 4.1.3.

As anticipated in the previous Section, for the following calculations, we will need the so-called *non-equilibrium* Green's functions

$$G_\sigma^< (x,t) = i \left\langle \psi_\sigma^\dagger (0,0)\, \psi_\sigma (x,t) \right\rangle \quad \longrightarrow \quad G_{0\sigma}^<(x,t) = \frac{e^{ik_F^\sigma x}}{x - v_f^\sigma t - i0^+} \ , \tag{4.17}$$

$$G_\sigma^> (x,t) = -i \left\langle \psi_\sigma (x,t)\, \psi_\sigma^\dagger (0,0) \right\rangle \quad \longrightarrow \quad G_{0\sigma}^>(x,t) = \frac{e^{ik_F^\sigma x}}{x - v_f^\sigma t + i0^+} \ , \tag{4.18}$$

as well as the *time-ordered* Green's function (or *electron propagator*), which is defined by

$$G_\sigma^T (x,t) = \theta (t)\, G_\sigma^> (x,t) + \theta (-t)\, G_\sigma^< (x,t) \ . \tag{4.19}$$

The calculation of transport quantities at steady state will benefit from being able to represent the Green's functions in the energy/momentum representation, through Fourier transforms such as[8]

$$G (k,\omega) = \int_{-\infty}^{+\infty} dt \int_{-\infty}^{+\infty} dx e^{-i(kx-\omega t)} G (x,t) \ . \tag{4.20}$$

In this representation it will be of foremost importance to state and exploit the *fluctuation-dissipation theorem* (FDT) which at equilibrium connect the greater/lesser Greens functions with the spectral function $A_{\sigma k}(\omega) = -\frac{1}{\pi}\mathrm{Im} G_\sigma^{ret}(k,\omega)$

$$G_\sigma^<(k,\omega) = i\Theta(-\omega) A_{\sigma k}(\omega) \qquad G_\sigma^>(k,\omega) = -i\Theta(\omega) A_{\sigma k}(\omega)\,, \tag{4.21}$$

where we assumed the distributions functions $f(\omega)$ defined in Eq.(1.16) to be evaluated at T=0 (and ϵ_F has taken to be 0).

Green's Functions for the Interacting ES In order to evaluate the correlators analytically, as customary in these cases, we "artificially" introduced a momentum-cutoff r in the integrals and a regularization cutoff 0^+ in the bare green's function.[9]

In calculations r will be considered finite but small so that in the integrals we can neglect the scale of variation of $U_i(p)$ and the curvature of the dispersion relation of the physical model[10]. This means in real space that the "bare" interactions can effectively be considered local (delta-like) in the space direction of propagation.

So we can write $U_1(p)/\pi \simeq w$, $U_2(p)/\pi \simeq u$ (these asymptotic values are often denoted in the g-ology literature as $g_{4\|}$ and $g_{4\perp}$) and $\theta_p \simeq \theta_0$. We may note that the intraedge interaction w enters in the equations simply by adding itself to the average Fermi-velocity. We include this renormalization in the following notation considering $\bar{v}$ to include the effect of the intraedge interaction.

Within these approximations, noting $v_\pm = \bar{v} \pm u$, we obtain the following analytical form for the retarded Green's function

$$\begin{aligned} \mathcal{G}_\sigma^{ret}(x,t) &= \Theta(t)[\mathcal{G}_\sigma^>(x,t) - \mathcal{G}_\sigma^<(x,t)] \\ &= \frac{\Theta(t)}{2\pi i} e^{ik_F^\sigma x}\Big[\prod_{j=+,-} \frac{g(x,t,r)}{(i(x-v_j t)+r)^{\frac{1}{2}+j\sigma\delta}} + (x\to -x,\ t\to -t)\Big] \ , \end{aligned} \tag{4.22}$$

[8] Inverse Fourier transforms are defined accordingly, introducing $(2\pi)^{-1}$ factors where necessary.

[9] We would like to point-out that, as reviewed by Solyom [86], the bosonization procedure allows to obtain results for the Green's function without the necessity to introduce these *physical* cut-offs since algebraic identities for the Tomonaga-Luttinger model are determined as a function of a single parameter α which is taken to zero at the end of the calculations to ensure proper commutation relations (see Eq.(4.9)). However, formally introducing a finite-range exponential suppression of the interactions (in momentum space) with constant interaction parameter results in formulas equal to those of constructive bosonization where α is simply replaced by the cut-off r.

[10] This automatically implies that $U_i(p)$ do not diverge for $p \to 0$, which is not the case for unscreened Coulomb interactions, which diverge logarithmically [104]. It is however very much likely that the interaction is screened and regularized by the metallic surroundings or the compressible stripes.

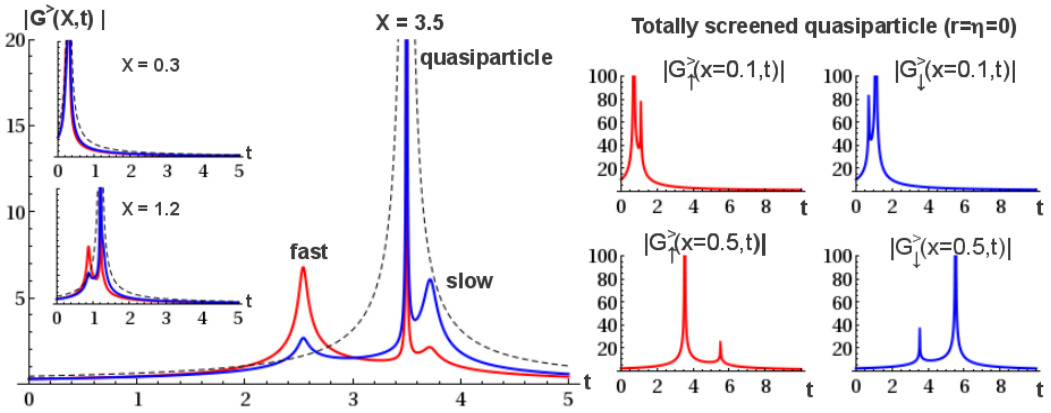

Figure 4.2: **Left panel**: $|\mathcal{G}_\sigma^>(x,t)|$ calculated with $r = 0.1$ (see Eqs.(4.12)-(4.14)) for different distances (Units are such that $v_F^\sigma = 1 \pm \delta v$, and $\delta = \frac{1}{5}$). **Right panel**: $|\mathcal{G}_\sigma^>(x,t)|$ with $r = 0$, $\delta = \frac{1}{5}$, for spin up (blue) and down (red) for distances of 100 and 500 nanometers. Times are measured in hundreds of nanoseconds. Interactions parameters, for both panels are the same as discussed in the text and as in Fig.(4.3).

where we introduced the *spin-asymmetry* parameter $\delta = \frac{1}{2}\sin\theta_0$ and the quasiparticle weight function $g(x,t,r) = (i(x-\bar{v}t)+r)(i(x-\bar{v}t)+0^+)^{-1}$. We note that while for $\delta = 0$ the "usual" spin/charge mode decomposition is perfect, if $\delta \lesssim \frac{1}{2}$ we are in the limit of strong asymmetry between spin-resolved channels, and the fast/slow modes are associated mainly with a particular spin-projection, since one of the two spin-charge peak will be strongly enhanced and the other strongly suppressed (see Fig.4.3) [142, 145, 144]. The spin dependency is manifested as well in the wavevector separation $\Delta k = k_F^\uparrow - k_F^\downarrow$, which is straightforwardly connected with the real-space separation of the edge channel (see Section 1.2.2).

In Fig.4.3 we show several plots of $\mathcal{G}_\sigma^>(X,\tau)$, which physically represent the probability amplitude of propagation of an electron from a point $x = 0$ at time $\tau = 0$ to a point $x = X$ at point $\tau = t$. The effect of the interaction cutoff is analyzed in the pictured example: the quasiparticle contribution (peak at $\bar{v}t = X$) corresponding to the total absence of spin-charge separation is visible only for r sufficiently large. For $r \neq 0$, at small distances of propagation, the quasiparticle contribution is so large that it smears out completely the peaks due to the fast and slow modes. For the transport calculations we will focus on the situation where $r = 0$ ("totally screened quasiparticle") and X is sufficiently large as to make distinguishable the effect of the collective modes (right panel of Fig.4.2).

We note that the Fourier transforms of the non-equilibrium Green's functions $\mathcal{G}_\sigma^>(x,\omega)$ and $\mathcal{G}_\sigma^<(x,\omega)$ have an analytical form in terms of Confluent Hypergeometric Functions [85]. For $r = 0^+$

$$\mathcal{G}_\sigma^>(x,\omega) = \frac{i\Theta(\omega)}{2\pi} e^{i[k_F^\sigma + \omega(\frac{1}{v_-})]x} \Phi[\frac{1}{2} + \sigma\delta, 1, ix\omega(\frac{1}{v_+} - \frac{1}{v_-})] \,, \tag{4.23}$$

where $\Phi(a,b,z)$ is the Kummer's confluent hypergeometric function[11]. By exploiting the relation $\Phi(a-b,b,-z) = e^z\Phi(a-b,b,-z)$ it can be shown that $\left|\mathcal{G}_\uparrow^>(x,\omega)\right| = \left|\mathcal{G}_\downarrow^>(x,\omega)\right|$ (see Fig.4.3) but the spin-dependence, which is only a phase in the space-

[11] Eq.(4.23) is already normalized (by choosing proper momentum/energy cutoffs) such that $\mathcal{G}_\sigma^>(x = 0,\omega) = -i\Theta(\omega)\int A(k,\omega)(2\pi)^{-1}dk = 1$

energy representation, is non trivial in time. One nice property of the analytical form of $\mathcal{G}_\sigma^>$ is the functional equivalence between ω and x, which always appear as ωx, so its algebraic decay in energy is the same as the decay with increasing distances. Indeed in the asymptotic limit

$$\left|\mathcal{G}_\sigma^> (x \gg 1, \omega)\right|^2 \simeq |\omega x p_-|^{2\delta-1} \ , \tag{4.24}$$

with $p_- = \left(\frac{\bar{v}^2-u^2}{u}\right)$. The divergences of the Green's function for $t = x/v_\pm$ determine the fundamental frequency oscillation periods in the Fourier transform $\mathcal{G}_\sigma^{ret}(x,\omega)$ [125, 105].

We would like to point-out that, restricting our study to 1D fermions of the TL of a single branch (the "right movers"), the Retarded/Advanced Green's functions, both bare[12] and dressed by the interactions, obey the "chirality identities"

$$\mathcal{G}^{ret}(x,\omega) = 0 \quad \text{for } x < 0 \tag{4.25}$$

and equivalently $G^{adv}(x,\omega) = 0$ for $x > 0$. This leads to the very useful identity for positive coordinates: $G^R(x,\omega) = G^>(x,\omega) - G^<(x,\omega)$ which allows analytical calculation of retarded Green's functions. We would like to point-out also that for $\omega > 0$ the following relation hold

$$\mathcal{G}^{ret}(x,\omega) = \mathcal{G}^>(x,\omega) \quad \text{for } x > 0, \omega > 0 \tag{4.26}$$

These identities have also strong consequences in deriving the Quantum Kinetic Equations discussed in the next section.

Physical parameters for the interacting ES model As thoroughly discussed in Chapter 1, typical effective models of narrow edge states that include interaction effects find a separation of the order of the magnetic length $l_B \simeq 10nm$ (at $\nu = 2$ with $B \simeq 5T$) which means that $\Delta k \simeq l_B^{-1}$. This difference in k-numbers enters in all Green's functions just as a global phase $e^{i\delta k x}$, so its effect is energy independent[13]. At fixed distance x, Δk provides a fixed phase difference between the two channels, whose effect on transport (within our setup described in the next Section) can be totally compensated by an appropriate phase difference $\delta\phi = \phi_L - \phi_R$ between the injection and detection basis, as it will be discussed in the next Section. For this reason, Δk is irrelevant for the sake of evaluating the effect of interactions in spin-interferometry , and we will set $\Delta k = 0$ in all our following numerical evaluations.

As we will see in more detail in Section 4.2.5, the spin-asymmetry is a crucial parameter for determining the interferometric pattern. In the non-interacting models discussed in Chapter 1, the dispersion bands are likely to have very similar slope in a hard-wall model, and in general the dependence of v_F on the wave-number through Eq. (1.10) is very small, so $\bar{v}/\delta v \ll 1$. It is however very hard to have a realistic idea on what might be the spin-asymmetry between the channels in interacting models also in the hard-wall confinement limit as the bands are heavily influenced by the interactions [101]. In the following we will consider the test-case of $\delta = 1/5$ (i.e. a deviation of about 10% from the average value $\bar{v}$).

Intra-edge interaction w and inter-edge interaction u must be of the same order of magnitude, with u in principle smaller due to the physical separation between the edge states, of the order of l_B. All previous assumptions lead to consider $v_F > w \gtrsim u$, but we stress that all these parameters depend non-trivially on the details of the nanostructures such as the presence of the metallic surrounding that can screen the interactions. In

[12] That is the Fourier transform of Eq.(4.16), i.e. $G^R_{0\sigma}(x,\omega) = -i\Theta(x)(2\pi v_F^\sigma)^{-1}\exp[i(k_F^\sigma + \omega/v_F^\sigma)x]$.

[13] It is obviously true that the physical separation influences the transport through the effective interaction parameters u and w.

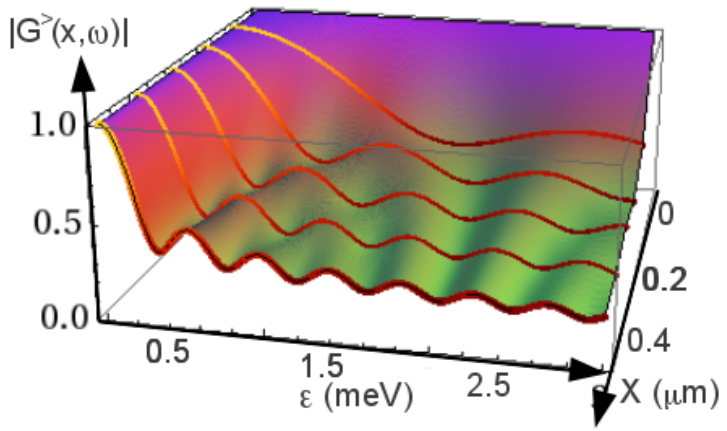

Figure 4.3: $|G^{>}_{\sigma}(x,\epsilon)|$ is plotted for $u = w = \frac{v_F}{2}$, $\delta = \frac{1}{5}$. The oscillating pattern follows the periods $\Delta\omega = \frac{2\pi}{x}\frac{v_+v_-}{v_-\pm v_+}$. The function profile for x =0.1, 0.2, 0.3, 0.4, 0.5 μm has been highlighted. The Green's function has been normalized so to respect the sum rule on the spectral function $-2\int \mathrm{Im}\mathcal{G}^{ret}_{\sigma}(x=0,\omega)\frac{d\omega}{2\pi} = 1$.

order to make calculations we take $w \simeq u \simeq v_F/2$, so: $v_+ \simeq 2v_F$ (fast mode) and $v_- \simeq v_F$ (slow mode). The quasi-particle weight is 1 for $r \to 0^+$, and in this case the transport is dominated by the collective modes.

The temperature will be taken to be zero, which with our parameters means that $k_BT \lesssim 10^{-6}eV$.

Considering Fermi velocities of the order of $10^5 ms^{-1}$ (see Table 1.1; it is the typical value measured in the experiment in [111]) and propagation distances of some microns,[14] we expect these peaks should occur at energies $\epsilon = \hbar\omega$ of the order of hundreds of μeV. Maximum energy for which the TL model is justified is $\epsilon_{max} \lesssim \hbar\omega_C \simeq 10^{-3}eV$, so we expect interesting dynamical transport features to arise in the energy window where the chiral TL model is valid.

4.2 Calculation of Electronic Current and Spin-Interference

In Section 1.3.4 we presented the scalable MZI and we explained how spin-resolved injection would be a straightforward way to obtain the delocalization on $\nu = 2$ ES. Using nanomagnetic spin-mixer devices such as the ones described in Section 3.3 would be perfect for setting up a practical spin-interferometer. However, for the sake of a theoretical analysis that includes interactions, the dynamical effects of a structured nanostructure consisting of an array of magnetic fingers would be very complicated to describe.

We notice however that two co-propagating channels of the same length characterized by different Fermi velocities are supposed to naturally induce different phase shifts on the electronic states travelling through them. As it is intuitive for non-interactive electrons (see Section 4.2.3), it is formally equivalent to consider two channels of different lengths or two channels of different v^{σ}_F, so that if $\delta \neq 0$ we can fabricate an interferometer without the necessity of spatially separate the trajectories of the co-propagating ES, if we have a way to create a superposition of spin-states at the entrance of the channels and we to filter out a given spin direction at the exit.

[14] We remind that at $\nu = 2$ the coherence length is expected to be of the order of tens of microns [25]

For this reason in this section we decided to focus on studying the properties of an idealized setup which allows arbitrary spin-state injection on spin-asymmetric edge channels and perfect spin-state filtering of the electronic current.

4.2.1 Spin-Resolved, Energy-Resolved Gedanken Experiment

The idealized setup (shown in Fig.4.4) consists of two non-interacting QDs which are weakly tunnel-coupled to an IQH Hall bar which is maintained at a given chemical potential ϵ_F by strong coupling with distant grounded ohmic contacts. QDs are in contact with non-interacting electron reservoirs at chemical potential μ_R and μ_L so that we can define a steady-state tunneling current I_{LR} from the left lead to the right lead, passing through the QDs L and R, and the edge channel.

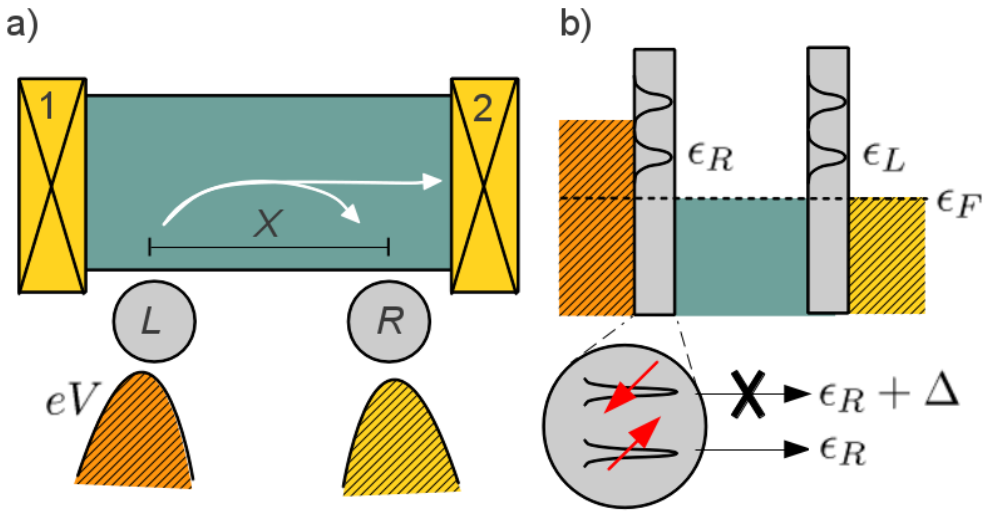

Figure 4.4: Setup of the gedanken experiment. **Left panel**: Planar view of the four-terminal device, reservoirs are Ohmic contacts 1,2 and the shaded regions under the quantum dots L,R are reservoirs maintained at chemical potential μ_L and μ_R. Contacts 1,2 are intended to be very far from L,R, ideally at infinity, and they are grounded. Only the reservoir connected to L is biased with respect to the ground. White arrows indicate the only non-compensated electronic currents. **Right panel**: Energy level view of the transport experiment. Transport occurs through resonances present in the quantum dots which are accessible within the transport window determined by the bias eV. **Zoom inset**: the tilted arrows represent the magnetic fields in the dots (see Eq.(4.31)), which allow only one spin-projection in an arbitrary basis to be transmitted in the propagation region.

The QDs are tuned so to provide single resonant energy levels ϵ_L and ϵ_R in the transport window of the system (see Fig.4.4), so that they can be represented by the following Hamiltonian

$$H_L^d = \epsilon_L d_L^\dagger d_L \qquad H_R^d = \epsilon_R d_R^\dagger d_R \ , \tag{4.27}$$

(d_i are fermionic operators representing the charge occupation of the level of the dot). If we set $\mu_R = \epsilon_F$ and $eV > \epsilon_F$, because of chirality the only non-zero current in the system will be originated from dot L and will be drained either by the reservoir of dot R or by the distant ohmic contact 2. We are of course interested in the current passing

through the right QD, defined as

$$I_R = e\frac{d}{dt}\left(d_R^\dagger d_R\right) \ . \tag{4.28}$$

If we include spin into the picture, the energy of the resonant levels $\epsilon_{i=R,L}$ becomes spin-resolved ($\epsilon_{i\uparrow} = \epsilon_{i\downarrow} + \Delta$) due to Zeeman energy and Coulomb blockade so that a single spin projection is allowed in the transport window (say $\downarrow$), while transport of $\uparrow$ (possible in principle through cotunneling) is exponentially suppressed at low temperature and for large Δ .[15]

We imagine that it is experimentally possible to orient the magnetic field acting on the dot along an arbitrary direction in space (defined by Euler's angles θ and ϕ). The energy levels would be eigenstates with respect to the new spin direction $|\nearrow\rangle = \cos\left(\frac{\theta}{2}\right)|\uparrow\rangle + e^{i\phi}\sin\left(\frac{\theta}{2}\right)|\downarrow\rangle$. In other words *only an electron with spin state* (θ_i, ϕ_i) *and energy* ϵ_i *would be allowed to tunnel through the dot* i *and contribute to* I_R. This gedanken situation would define the spin-resolved, energy-resolved steady state transport problem object of this work. This situation is reproduced by the following model Hamiltonian

$$\begin{aligned} H &= H_R^d + H_L^d + H_R^{Res} + H_L^{Res} + H_{TR} + H_{TL} + \\ &+ H_R^{TE} + H_L^{TE} + H_{edge} \ , \end{aligned} \tag{4.29}$$

where the reservoir Hamiltonians are just free Fermi liquids (electronic operators c_k), tunnel coupled (by means of tunnel amplitudes labeled T_k) to the quantum dots

$$\begin{aligned} H_i^{Res} &= \sum_k \left(\epsilon_k - \mu_i\right) c_k^\dagger c_k \ , \\ H_{Ti} &= \sum_k \left(T_k c_k^\dagger d_i + T_k^\star d_i^\dagger c_k\right) \ , \end{aligned} \tag{4.30}$$

which as previously explained are transmitting a specific spin projection on the edge through tunneling

$$H_i^{TE} = t_i \sum_\sigma V_i^\sigma \psi_\sigma(x_i) d_i^\dagger + h.c. \ , \tag{4.31}$$

where $V_i^\uparrow = \cos\frac{\theta_i}{2}$ $\quad V_i^\downarrow = \sin\frac{\theta_i}{2} e^{i\phi_i}$ represent the spin projection on the Bloch-sphere, and $\psi_\sigma(x_i)$ is the wavefunction of an electronic state (whose spin projection is σ) defined on the edge, that has been defined in the Hamiltonian H_{edge} (see Section 4.1).

Experimental Considerations We would like to point out that it is not realistic to have local and strong magnetic fields such to define a proper arbitrary basis in the quantum dots of our setup, but such strong static fields have been introduced in the model in order to have a simple treatment of the electronic transport.

However it is now technologically possible to prepare locally an electronic spin-state in quantum dots by mean of Electron Spin Resonance [114], and to measure its spin state by means of spin-dependent tunneling rates [115, 116]. Recently it has also been shown in an experiment that the preparation can indeed be followed by propagation of the single electron over a chiral channel (controlled by surface acoustic waves) and by detection and entrapment in a second quantum dot [117]. It is also experimentally demonstrated that tiny quantum dots can be coupled to the edge states reliably in

[15] Spin-blockade transport effects of this kind are behind what is called "Spin-to-charge conversion" in the literature [118, 135], and they are nowadays very well controlled experimentally [116, 141].

such a way to filter the energy of the incoming wavepackets [134], and energy-resolved single-electron injection in edge channels has been recently achieved [112].

In principle, it would be highly desirable to couple the time-dependent procedures necessaries for spin-state preparation with the amazing control over transport offered by these energy-resolved setups, despite the challenge looks formidable from the experimental point of view.

Keeping in mind these technological considerations, we can assess the steady state transport calculation described in this Chapter as an approximation of a realistically achievable time-dependent transport procedure.[16]

Moreover, we mention that while our idealized setup has in mind planar, gate-defined quantum dots and GaAs 2DEGs, our calculations might be as well relevant for conceptually similar future experiments in systems employing tunneling by suspended Tips in surface 2DEGs [153], Graphene [51], Topological insulators [152, 157] or clean Nanotubes [158] .

4.2.2 Tunnel-coupled Detectors and Current Formula

The current I_{LR} is straightforwardly computed by the LB formalism (see Eq.(1.15)) if the system is non-interacting, once the transmission coefficient between the leads L, R is defined

$$I_{LR} = \frac{e}{h} \int \frac{d\omega}{2\pi} \left[f_L(\omega) - f_R(\omega) \right] \rho_L(\omega) \, \rho_R(\omega) \, T(\omega) \ . \tag{4.32}$$

This transmission coefficient physically represents the probability amplitude of arrival of an electron wavepacket traveling at fixed energy ω, and we already observed in Section 3.1.1 that in non-interacting system it is connected to a microscopic model through the Fisher-Lee formula (see Eq.(3.10))

$$T(\omega) = |t_R|^2 \, |t_L|^2 \sum_{s\sigma} \Gamma_{s\sigma} G^{ret}_{0s}(x,\omega) G^{adv}_{0\sigma}(-x,\omega) \ , \tag{4.33}$$

with $\Gamma_{s\sigma} = V_R^{\sigma} \left(V_R^{s}\right)^* V_L^{s} \left(V_L^{\sigma}\right)^*$ and $G_0^{ret/adv}$ are the non-interacting retarded / advanced Green's functions defined on the edge channels, properly normalized in order to give unit probability current flux.

As it will be detailed in Section 4.2.5, this formula can be easily understood in the non-interacting limit as the amplitude of a double projection of a spin-state performed by the injector/detector quantum dots. The initial spin state injected on the edge channel is $|\psi_{in}(x = L)\rangle = V_L^{\uparrow} |\uparrow\rangle + V_L^{\downarrow} |\downarrow\rangle$. After propagation the spin components might have accumulated a phase difference $\Delta\varphi$ due to different path lengths or different channel velocities $|\psi_{in}(x = R)\rangle = V_L^{\uparrow} |\uparrow\rangle + V_L^{\downarrow} e^{i\Delta\varphi} |\downarrow\rangle$. The state can tunnel in the detector quantum dot, with amplitudes $V_R^{\uparrow,\downarrow}$: $|\psi_{dotR}\rangle = \left(V_L^{\uparrow} V_R^{\uparrow} + V_L^{\downarrow} e^{i\Delta\varphi} V_R^{\downarrow} \right) |d\rangle$. We need to take the modulus square of this state to evaluate the probability of occupation of the dot, obtaining "direct" terms $\Gamma_{\sigma\sigma}$ and "interference" terms $\Gamma_{\sigma,-\sigma}$. The phase difference $\Delta\varphi$ will play a role in the crossed transmission coefficient (see Eq.4.50).

The Fisher-Lee formula is a useful relation which is valid only in the non-interacting weak-bias regime, while the gedanken experiment presented in the previous section considers interacting electrons injected at energies ϵ_L and ϵ_R which can be, in principle, well above the Fermi level. In order to obtain a close expression for the current in terms

[16] The typical timescales of operation of the external field required for the spin-state preparation are at least one order of magnitudes smaller (μs) than the inverse tunneling rates in the weak coupling regime ($10^{-5} s$), so in first approximation the steady model where the spins are polarized by local constant fields is relevant.

of computable observables for arbitrary bias and many-body interactions, we need to turn our attention to a more complex Green's function theory.

Before discussing the theory at the technical level in the next Section, we present the general philosophy of the current calculation. The current signal of interest Eq. (4.28) is a local quantity evaluated *in the dectector*, whose computation involves of course the knowledge of the non-equilibrium dynamics of the whole system. Being the current detector a tunnel contact weakly coupled to the Hall bar, its detection probability (probability of transition from 0 to 1 electrons in the dot, $R_{0\to1}$) up to time t could be described, without losing generality, by Fermi's golden rule:

$$R_{0\to1}(t) = \int_{-\infty}^{t} f(\tau-\tau')S(x_R,x_R;\tau-\tau')d\tau d\tau' \tag{4.34}$$

where f is a function describing the detector and S is the square modulus of the transition matrix element among the states in the edge channel, which corresponds to the local density of state multiplied by the distribution function. At steady state, these correlators corresponds respectively to the Green's functions $g_R^>(\omega)$ and $G^<(x_R,x_R;\omega)$ in the energy representation.

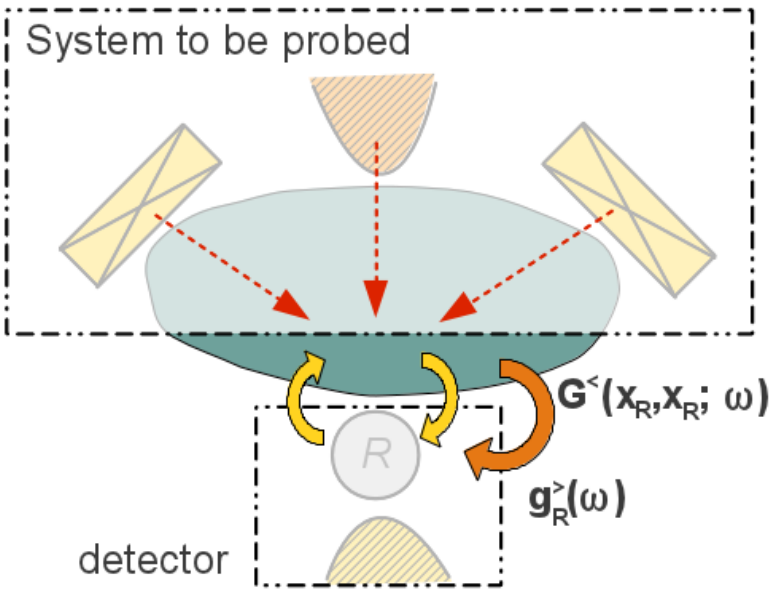

Figure 4.5: Pictorial view of the current formula at lowest order in perturbation theory. The current is seen as the tunnel transition between two regions (detector and system) characterized by their Green's functions. The function $G^<(x_R,x_R;\omega)$ includes the injector and the other reservoirs, which do not contribute to the excess current in the system as they are at the same chemical potential as the detector (yellow arrows).

This signal is straightforwardly linked with the energy-resolved current observable, as long as we consider the detector function to filter out a single energy level, similarly to the detector used in the experiments in Ref. [111].

In the stationary regime, the Fourier transform of D is then proportional to $\delta(\epsilon-\epsilon_R)$.[17] The whole difficulty of the problem consists in the proper calculation of Green's

[17] We note that the choice of having an energy-resolved detector is very particular case. It could be interesting to consider *time-resolved* detectors[107] or detector functions with special spectral properties adapted for particular tasks.

function $G^<(x_R, x_R; \omega)$, which contains information about the many-body out of equilibrium state of the 2DEG connected to its reservoirs (See Fig.4.5). The non-equilibrium Green's function diagrammatic technique described in the next section is capable to rederive the perturbative formula for the current, and to provide a general framework of calculation of this local quantity for an interacting system (at the perturbative level with respect to the tunnel amplitude of injection).

4.2.3 Non-Equilibrium Green's Functions

Following the early works of Caroli and Nozieres [121], Meir and Wingreen [69], we express the non-equilibrium tunneling current in mesoscopic devices in terms of the non-equilibrium Green's functions $G^<$ and $G^>$ defined in Section 4.1.3. Their computation is achievable to arbitrary order in perturbation theory by means of a diagrammatic quantum field theory (QFT) technique originally developed by Keldysh, whose application to non-equilibrium transport problem has become a standard for steady-state current calculations [70].

The idea is based on the observation (originally made by Schwinger) that the Gellman-Low theorem for ground-state expectation values (with respect to H_0) of operators in equilibrium QFT (at T=0 for simplicity) is generalizable for time-dependent Hamiltonians [67].

This theorem (together with Wick's theorem) defines the diagrammatic expansion in terms of the Taylor series of the time-ordered evolution operator $\mathcal{T}_t \exp[-i \int_{-\infty}^{+\infty} H'(t)dt]$, where $H'(t) = e^{iH_0 t} H' e^{-iH_0 t}$ is a time-independent Hamiltonian in the interaction picture, and $\mathcal{T}_t\{\dots\}$ indicates time-ordering of the operators inside the brackets.[18]

For explicitly time-dependent Hamiltonians $\mathcal{H}'(t)$ (which are in principle necessary to define steady state non-equilibrium transport, see Section 1.3.2), the formula that initiates the perturbative expansion (or alternatively the diagrammatic series) reads

$$\langle \hat{O}(\tau_0 \dots)\rangle_{\mathcal{K}} = \mathcal{Z}_0^{-1} \langle \mathcal{T}_\tau \{ e^{-i \int_{\mathcal{K}} \mathcal{H}'(\tau) d\tau} \hat{O}(\tau_0 \dots)\}\rangle \ , \tag{4.35}$$

where the expectation value is still taken with respect to H_0, and $\mathcal{Z}_0$ is formally just a normalization factor meant to cancel the disconnected diagrams of the expansion (Cancellation Theorem).

In Eq.(4.35) the time variables τ and τ_0 are taken on the *Keldysh Contour* $\mathcal{K}$ (see Fig.4.6), i.e. over an unphysical one-dimensional manifold where times are orderly labeled from $-\infty$ to an arbitrarily large $\bar{\tau}$ $(+\infty)$, and then back to $-\infty$. The first part of the ordered infinite line from $-\infty$ to $\bar{\tau}$ determines the *upper branch* of the contour (times on this line are labeled with a $+$ superscript, e.g. t^+), while the second part (from $\bar{\tau}$ to $-\infty$) is the *lower branch* (times are labeled t^-).

Contour-ordered Green's functions are just observables composed by electronic operators whose times live on $\mathcal{K}$. There exist analytical continuation rules that allow to express regular Green's functions in terms of contour-ordered Green's functions, so Eq.(4.35) can indeed be used to compute useful quantities.

In particular, greater Green's functions[19] are

$$G^>(x, \tau_1 - \tau_2) \equiv G_{\mathcal{K}}(x, \tau_1^- - \tau_2^+) \ , \tag{4.36}$$

where $G_{\mathcal{K}}$ is the Green's function obtained through Eq.(4.35), for $\hat{O}(\tau_1, \tau_2) = \psi(\tau_1)\psi^\dagger(\tau_2)$.

[18] We will not remind the diagrammatic technique here. For a complete review, including Feynman rules for constructing diagrams, see [65].

[19] Lesser Green's functions have a similar relations with $+$ and $-$ inverted, and retarded Green's functions can be computed by means of $G^{ret}(t) = \Theta(t)[G^>(t) - G^<(t)]$.

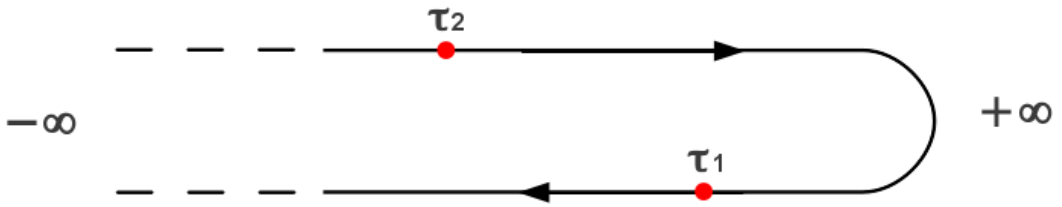

Figure 4.6: Keldysh Contour $\mathcal{K}$. τ_1 lives on the lower branch (τ_1^-), τ_2 lives on the upper branch (τ_2^+). As detailed in textbooks such as Ref. [70], $G^<(t_2-t_1) = G_\mathcal{K}(x, \tau_2^+ - \tau_1^-)$ and $G^>(t_1-t_2) = G_\mathcal{K}(x, \tau_1^- - \tau_2^+)$

The analytical continuation rules that lead to Eq.(4.36) can be extended to products and τ-convolutions of Green's functions (Langreth's theorem), such as the ones that arise in the diagrammatic expansion of Eq.(4.35). For example, for $G_\mathcal{K}(\tau_0 - \tau_0')$ we obtain the *Dyson equation* in $\mathcal{K}$, which has the generic form

$$G^T(\tau_0 - \tau_0') = G_0^T\left(\tau_0 - \tau_0'\right) + \int_\mathcal{K} d\tau_1 \int_\mathcal{K} d\tau_2 G_0^T\left(\tau_0 - \tau_1\right) \Sigma^T\left(\tau_1 - \tau_2\right) G^T\left(\tau_2 - \tau_0'\right) \tag{4.37}$$

(we omitted spatial variables for clarity and generality, and we noted Σ^T the generic contour-ordered *self-energy* of the system).[20] Noting as $\star$ the contour-time convolution integrals[21], the greater $G^>(t_0 - t_0')$ is then

$$G^> = G_0^> + [G_0^{ret} \star \Sigma^{ret} \star G^<] + [G_0^{ret} \star \Sigma^< \star G^{adv}] + [G_0^< \star \Sigma^{adv} \star G^{adv}] \ , \tag{4.38}$$

where t_0 and t_0' are now defined on the physical timeline. For steady-state transport calculations it is useful to use the time-Fourier transformed version of Eq.(4.38), so that convolutions in time are replaced by products in the frequency domain. By manipulating the resulting equation, and eliminating some terms proportional to $G_0^<$ which vanish at steady-state [70], we are left with the famous *Keldysh Equation* (KE)

$$G^>(\omega) = G^{ret}(\omega)\Sigma^>(\omega)G^{adv}(\omega) \ . \tag{4.39}$$

The Dyson's equations for the retarded Green's functions are instead analytically continued from the contour ordered ones by maintaining completely their structure:

$$G^{ret}(\omega) = G_0^{ret}(\omega) + G_0^{ret}(\omega)\Sigma^{ret}(\omega)G^{ret}(\omega) \ . \tag{4.40}$$

In the next subsection we show how the full knowledge of $G^>$ and G^{ret} is sufficient to compute the current at lowest perturbative order for the setup described in Section 4.2.1, and all the complexity of the problem will be contained in the definitions of the self energies.

4.2.4 The Non-Crossing Approximation

In the previous discussion on the diagrammatic theory we did not comment on the explicit form of the self-energies. Formally speaking, the self-energies are summations of diagrams which represent the influence of the perturbations on the base Hamiltonian H_0^{TL} (i.e. the effect of the vertices of the theory). In our transport problem, the perturbative vertices are those defined by H_{int}^{TL} (4.3) and H_i^{TE} (4.31).

[20] The diagrammatic equation previously shown in Fig.4.11 has also this form, where Σ is represented by Π.

[21] I.e. $G_1 \star G_2 = \int_\mathcal{K} d\tau G_1(\tau_0 - \tau_1)G_2(\tau_1)$. Also summations on spin-indices is implicit, respecting the conservation rules.

When Coulomb interactions or other many-body effects are taken into account the scattering picture is likely to be completely spoiled. Indeed, LB-like formulas can be usually recovered in the presence of interactions only if they are approximated as one-body potentials. For Coulomb interactions the presence of the particle-hole continuum makes this task in principle impossible even for weak interactions [120]. Despite these discouraging considerations, here we will show that, due to the chiral properties of our system, in the "high energy" elastic regime for small tunneling amplitudes we can apply the so-called "non crossing approximation" (NCA) to recover a LB-like formula Eq.4.32, which embodies also some non-perturbative effects of interactions.[22]

The NCA (widely used in the context of electron-phonon coupled systems, and in strongly correlated system such as impurities in the Kondo regimes) states that the self-energy due to the tunneling Hamiltonian and the self-energy due to electron-electron interactions are completely decoupled. More clearly, the total self-energy of the electron on the channel would be[23]

$$\Sigma_{tot} = (\Sigma_{tL} + \Sigma_{tR} + \Sigma_{int}) + \Sigma_{cr} \ . \tag{4.41}$$

The first two terms in the parenthesis are the tunneling self-energies due to the coupling to the dots. The third term is the self-energy due to Coulomb interactions, while Σ_{cr} represent the crossed irreducible diagrams between the tunneling and the interaction vertices. Neglecting this last self-energy (which has non-vanishing contributions at order $|t_i|^2$, see later) is the NCA. Dependencies on frequency and position are implicit in Eq. (4.41), but note that we assume the tunneling process to be local in space: $\Sigma_i^t(\bar{x}, \bar{x}'; \omega) \propto \delta(\bar{x} - \bar{x}')\, \delta(\bar{x} - x_i)\, \tilde{\Sigma}_i^T(\omega)$.

Although the examined setup is a four-terminal system, due to the bias configuration is arbitrary to evaluate the current in the right dot or left dot, as long as we keep only terms at order $|t_R|^2 |t_L|^2$ in perturbation theory.[24] If we take the NCA as granted (see later for justifications), following the standard approach detailed in textbooks such as Ref.[70], the tunneling current I_R might be written in terms of the local density of states as long as we take into account at the lowest non-vanishing order in the tunneling amplitude t_L the full expression of the Green's functions[25]

$$I_R = \frac{e}{h} |t_R|^2 \sum_{\sigma\sigma'} V_\sigma^R V_{\sigma'}^{R*} \int \frac{d\omega}{2\pi} [G^>_{\sigma\sigma'}(x_R, x_R;\ \omega) g_R^<(\omega) - G^<_{\sigma\sigma'}(x_R, x_R;\ \omega) g_R^>(\omega)] \ . \tag{4.42}$$

Note that this formula correspond to the Fermi golden rule result for the current signal in a weakly coupled detector discussed in the previous section, Eq. (4.34).

[22] As long as we stay perturbative at lowest order in the tunneling amplitudes, in principle it is not necessary to introduce further approximations since the Bosonization technique allows an exact calculation of the four-fermions correlation functions that result out of the exact perturbative treatment [143]. Despite the existence of analytical results, the current formulas are quite involved to deal with, both numerically and at the interpretative level, for the single-branch TL model with spin. Simplifications exists instead for tunneling in IQH systems for $\nu \leq 1$ [99], and between interacting *counter-propagating* edge channels [100, 139].

[23] We remind that in our setup we can disregard the four-terminal nature of the transport as the ohmic contacts 1 and 2 are grounded and placed at infinity, so their effect is included when we take expectations value over the ground state of H_{edge}.

[24] We note that the proper treatment of transport should include self-energies concerning all four terminals in order to be consistent with total current conservation in this chiral system, but if stick to the present perturbative calculation in the limit of a very long Hall-bar we can avoid discussing about ohmic contacts 1,2. It is however important to note that these terminals *must be present* in the real experiment, otherwise the "channel" would be formally a closed system where energy relaxation doesn't occur. This is indeed also verified experimentally [111].

[25] Green's functions with double spin indices imply that their perturbative development can in principle result in a non-zero propagator from spin σ to spin $-\sigma$. But of course when electronic operators are evaluated on the Fermi sea, spin conservation implies that $\mathcal{G}_{\sigma\sigma'} = \mathcal{G}_\sigma \delta_{\sigma\sigma'}$.

We immediately note that in our idealized setup, the reservoir+dot Green's functions g_R at zero temperature can be written as $g_R^<(\omega) = if_R(\omega)\rho_R\delta\left(\omega - \epsilon_R\hbar^{-1}\right)$ and $g_R^>(\omega) = -i[1-f_R(\omega)]\rho_R\delta\left(\omega - \epsilon_R\hbar^{-1}\right)$ so for positive $\epsilon_R < eV$ (in the elastic limit $\epsilon_L = \epsilon_R$) we can already disregard the second part of the equation in the parenthesis, as the right QD is forced to be empty by the reservoir. This means that the current can be expressed in terms of the diagrammatic expansion of $G^<_{\sigma\sigma'}(x_R, x_R;\,\omega)$ alone.

With reference to the notations summarized in Table 4.1 on page 65, the interacting Green's function, calculated in Section 4.1.3 through the Bosonization procedure, can be formally expressed by a Dyson's expansion

$$\mathcal{G}^T_\sigma(x,x') = G^T_{0\sigma}\left(x,x'\right) + \int d\bar{x}d\bar{x}' G^T_{0\sigma}\left(x,\bar{x}\right) \star \Sigma^T_{int}\left(\bar{x},\bar{x}',\sigma\right) \star \mathcal{G}^T_\sigma\left(\bar{x}',x'\right) \ . \tag{4.43}$$

Still on the contour, as long as we stay at order $|t_L|^2$, we can rewrite Dyson's equation for the *full* Green's function in terms of the tunneling self-energies and $\mathcal{G}^T$ only

$$G^T(x,x') = G^T_0\left(x,x'\right) + \int d\bar{x}d\bar{x}' G^T_0\left(x,\bar{x}\right) \star \Sigma^T_{tot}\left(\bar{x},\bar{x}'\right) \star \mathcal{G}^T\left(\bar{x}',x'\right) \ . \tag{4.44}$$

By applying the KE, after time Fourier transform, the greater component reads

$$G^<(x_R,x_R;\omega) \;\; = \;\; \int d\bar{x}d\bar{x}' \mathcal{G}^{ret}(x_L,\bar{x};\omega)\Sigma^<_{tot}(\bar{x},\bar{x}';\omega)\mathcal{G}^{adv}(\bar{x}',x_L;\omega) \ , \tag{4.45}$$

where the real-time Green's functions $G^{ret}$and G^{adv} have been immediately identified with their interacting counterparts $\mathcal{G}^{ret}$ and $\mathcal{G}^{adv}$, since for Eq.(4.25) their contribution at order $|t_L|^2$ is zero. This simplification states that the only contribution of Eq.(4.45) to the current at this order comes by considering $\Sigma_{tot} = \Sigma_{tR}$.

The final formula for the current at order $|t_R|^2 |t_L|^2$ has a simple term which looks like Eq.(4.32)-(4.33) where the Green's functions are now the interacting ones[26]

$$I_{RL} = \frac{e}{h}|t_R|\,|t_L|^2 \rho_R\rho_L \sum_{s\sigma} \Gamma_{s\sigma}\mathcal{G}^{ret}_s(X;\epsilon)\left[\mathcal{G}^{ret}_\sigma(X,\epsilon)\right]^* \tag{4.46}$$

where $X = x_L - x_R$, $\epsilon = \epsilon_R = \epsilon_L$ and $\mathcal{G}^{ret}$ follow the Dyson equation Eq.(4.43) (for retarded functions instead of time-ordered functions). Eq.(4.46) is a very general one for chiral system weakly coupled to the tunneling contacts.[27]

We stress that despite Eq.(4.46) looks like a simple generalisation of the LB non-interacting formula, its validity in an interacting system is *not* a standard result. In our setup, this form is a consequence of the elastic transport regime, of the technical simplifications due to chirality, of the assumption of weak tunneling and of the application of the NCA approximation[28].

Crossed contributions and elastic current We would like to point out that the NCA approximation as in Eq.(4.41) gives a purely elastic contribution to the current. Indeed if $\epsilon_R \neq \epsilon_L$ the product of the two density of states of the quantum dots will give zero, unless some broadening of the resonance line is introduced. So the crossed diagrams which we neglected are responsible for all the inelastic current passing through the device. One question remains: do the disregarded "crossed contributions" have an important influence also in the elastic case?

[26] A similar result has been obtained also in Ref.[126], where the NCA was applied for a non-chiral spinless TL liquid.

[27] In the following we will resum all the interactions in the diagrammatic theory by exploiting the solution of the TL model. However at this stage, the form of the interaction is still to be specified through Eq.(4.43).

[28] We note that a similar result can be obtained in terms of the plasmonic scattering formalism developed in Refs. [155, 107].

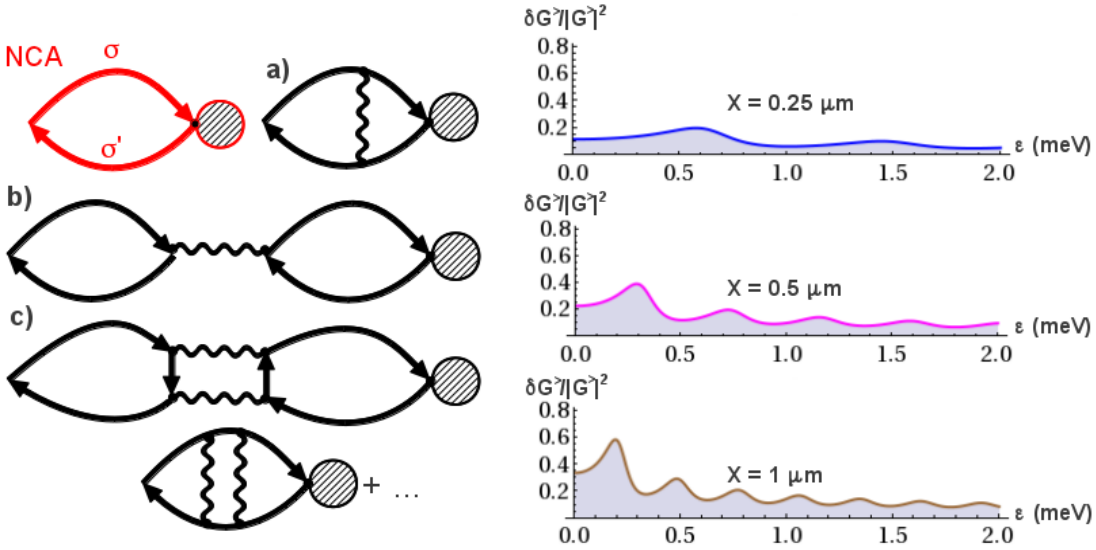

Figure 4.7: **Left panel**: $G\left(x_i x_i, \omega\right)$ contribution to the elastic current I_{RL} is visualized in terms of diagrams implementing diagrammatic non-crossing approximation (NCA, shown in red) and corrections. The thick arrows represent fully interacting Green's function with a give spin-index. Double wavy lines are renormalized propagators of the interaction (see Fig.4.11). All Fermionic Green's functions are considered to be evaluated at the same energy ω. The shaded circles are the tunneling self-energy relatives to dot R **(a)** some examples of irreducible corrections to the NCA. The first order diagram is equivalent do diagram of type-b. **(b)** reducible corrections to the NCA that can be evaluated. The NCA is assumed to be valid in the Fermionic loops which are not affected by diagrams of type a. **(c)** high-order irreducible corrections to the NCA which are disregarded. **Right panel**: $\delta G^{>}/\left|G^{>}\right|^2$ for X =0.25 (blue), 0.5 (purple), 1 (brown) μm. The parameters are the same as Fig. 4.3, and the effective interaction for these examples has been taken to be the maximum between $\tilde{u}$ and $\tilde{w}$ (See appendix III on page 89).

We can evaluate some crossed contributions in the elastic limit in order to estimate the validity of NCA, thanks to some diagrammatic properties of the TL model. In Fig.4.7 we give a diagrammatic view of Eq.(4.46), and we made clear what type of diagrams we are excluding by implementing the NCA.

Diagrams as those of type a) in Fig.4.7 are irreducible vertex corrections to the tunneling self-energy.[29]

We can also choose to retain the terms of type b) in Fig.4.7, which give rise to a "reducible" contribution of the diagrammatic expansion of $G^T_{\sigma\sigma'}(x_L, x_L;\ \omega)$. Since we are working in the elastic limit, and the interaction propagators are local in space, this contribution is formally equivalent to the first order diagrams of type-a. Once the contour-ordered convolution integrals are analytically continued in real-time, and Fourier transformed to frequency domain, the crossed correction would result in the

[29] We note that while we would be tempted by the diagrammatic structure of the current diagrams of type (a) to use Ward's identities [86] for the interacting vertex (evaluated for interactions carrying zero energies) and apply them for dressing the tunneling self-energy. Computing these dressings would solve the elastic perturbative limit exactly. However, these identities strongly rely on charge/spin conservation, and it is still not clear if they can be used for the simplification of vertex corrections of local tunneling vertices in a four-terminal geometry such as the one of our setup.

sum of many products of six Green's functions of the form

$$\begin{aligned}\delta G^{>}_{\sigma\sigma'} = \quad & \int dx dx' G^{ret}_{\sigma}(x_L - x;\epsilon_L) G^{ret}_{\sigma}(x - x_L;\epsilon_L) \\ & \times D^{ret}_{\sigma\sigma'}(x - x';\omega = 0) V^{R}_{\sigma'} V^{R*}_{\sigma'} g^{ret}_{R}(\epsilon_R) \\ & \times G^{<}_{\sigma'}(x' - x_R;\epsilon_R) G^{adv}_{\sigma'}(x_R - x';\epsilon_R) \\ + \quad & \text{(other projections}\dots\text{)} \quad .\end{aligned} \tag{4.47}$$

First, we note that the interaction propagator $D_{\sigma\sigma'}(x, x';\omega)$ is enforced to be evaluated at zero energy by the NCA, because of the energy conservation at the vertex with fermionic lines. It is then proportional to $\delta(x - x')$ as discussed in Section 4.1.3. Second, we observe that in principle the diagrams that we consider can give also an inelastic contribution, but we will limit ourselves to the study of the elastic case $\epsilon = \epsilon_R = \epsilon_L$ since otherwise also the higher-order diagrams might be quantitatively relevant.

Terms such as those of type c) in Fig.4.7 are of higher order in the renormalized interactions, and can be thus neglected in first approximation if $\tilde{u}$ and $\tilde{w}$ are smaller than $v_F + \delta v$. In this sense we are introducing a further approximation in the model, which is considered to be weakly interacting, but still exhibits non-perturbative effects.

The Green's functions labels in Eq.(4.47) can be finally found by means of the chirality identities Eq. (4.25): among all possible combinations the only contributing term to $\delta G^{>}_{\sigma\sigma'}(x_L, x_L;\ \epsilon_L)$ is

$$\delta G^{>}_{\sigma\sigma'} = V^{R}_{\sigma'} V^{R*}_{\sigma'} D_{\sigma\sigma'} \int_{x_L}^{x_R} dx \left|\mathcal{G}^{R}_{\sigma}(x_L - x;\epsilon)\right|^2 \left|\mathcal{G}^{R}_{\sigma'}(x;\epsilon)\right|^2 g^{<}_{R}(\epsilon) \ . \tag{4.48}$$

Note that the prefactor to the integral (4.48) encodes the only spin dependence of the correction, since the "transmission coefficients" $\left|\mathcal{G}^{R}_{\sigma}(x;\epsilon)\right|^2$ are spin independent as detailed in Section 4.1.3.

In Fig.4.7 we plot the contributions of this term as a function of the energy for several distances. It is immediately evident that at fixed distance X, for high-enough energy these corrections becomes less important. However the importance of this contributions grows with X, as it is clear from the integration boundaries. For the chosen parameters in the Figure it is easy to see that, for energies bigger than 0.5 meV with respect to ϵ_F, the contribution is less than 10% to the total signal and thus can be neglected. For energies close to ϵ_F, the contribution might be important for long propagation distances, this is why we consider the present theoretical work to be quantitatively valid only for relatively "hot" electrons.

The NCA is usually a non-controlled approximation. Computing its first corrections and checking that are small adds confidence in the approach (at least for weak interactions) but a more general result on its validity can in principle be explored by trying to extract the exact elastic contribution from the general perturbative results, which involves four-fermions correlators. Some preliminary works in this directions, that benefit of the plasmonic scattering formalism [155, 107] indicate that the NCA formula (4.46) might be valid also for elastic low-energy current. We finally also note that another technical solution could be provided by the recent non-equilibrium Bosonization approach [108].[30]

[30] Note that in the plasmonic scattering approach, an energy-resolved injector would be formalized as an initial state of the electron defined as fermionic operator in an arbitrary-spin state. In the non-equilibrium bosonization approach the interactions are confined to the propagation zone, and absent before and after this region. Conceptually speaking, both formalisms do imply an independence between the injection/detection tunneling process and the interactions, similarly to the spirit of the NCA.

4.2.5 Spin-Interference

Eq.(4.46) can be rewritten in the form

$$T(\omega) = [\cos^2\frac{\theta_L}{2}\cos^2\frac{\theta_R}{2} + \sin^2\frac{\theta_L}{2}\sin^2\frac{\theta_R}{2}]M(\omega) + \frac{1}{2}\sin(\theta_L)\sin(\theta_R)\mathrm{Re}[e^{i\delta\phi}F(\omega)] \tag{4.49}$$

where $M(\omega) = \left|\mathcal{G}^R_\sigma(L,\omega)\right|^2$ and $F(\omega) = \mathcal{G}^R_\downarrow(L,\omega)\,\mathcal{G}^R_\uparrow(L,\omega)^*$ where L is now the distance of propagation.

In the non-interacting case the transmission coefficient reads $M^0(\omega) = 1$ and the interference term is

$$F^0(\omega) = \exp\left[i\left(\delta k + \delta v/\left(v_F^2 - \delta v^2\right)\omega\right)L\right]. \tag{4.50}$$

This total transmission coefficient illustrates the interferometric nature of the idealized setup that we are studying: sweeping the configurations of the magnetic fields of the injector and detector dots we get oscillations, as well as energy dependence of the transport due to interactions. In particular if we fix $\theta = \theta_R = \theta_L$ we define a proper spin-basis of transport, and we can think of the current as a signature of the quantum-state transfer probability of spin-states oriented on a given axis in space (flying spin qubits).[31] We stress that what allows our setup to act as an interferometer is the *spin-orbital entanglement* intrinsic in the spin-resolved edge channels. The phase acquired by the difference in the Fermi velocities (an orbital effect) is automatically transferred to the spin-state when the charge state is measured (in the detector). All charge transfers between the channels being forbidden, it is clear that the interactions can influence the interference signal only through the last term in Eq. (4.49). We expect the interactions to introduce some non-trivial effects of the phase between the channels, so we are mostly interested in studying the current oscillations that we obtain changing the $\delta\phi$ variable, which is a direct measure of the relative phase accumulated between the two spin-states after propagation through the channel.

As a working example we fix $\theta = \pi/2$, which means that we are symmetrically coupled to both spin channels on the Hall bar (or alternatively, we are transporting spin qubits on the cartesian x direction on the Bloch sphere). Then the transmission coefficient of this spin state, by means of Eq.(4.49), will oscillate in $\delta\phi$ as

$$T_X(\omega) = \frac{1}{2}[M(\omega) + \cos(\delta\phi)\mathrm{Re}F(\omega) - \sin(\delta\phi)\mathrm{Im}F(\omega)] \tag{4.51}$$

We can immediately see that if $\delta v = 0$ the interference pattern has a very simple $\delta\phi$ dependence (See Fig. 4.8, top panels). The effect of the interactions is just a damping of the transmission which oscillates with energy, indicating a loss of the signal which is transferred to other energies (by inelastic processes). This can be visualized as a distortion of the precession of the spin, which is expected to occur in the non-interacting system as pictured in Fig. 4.9.

If $\delta \neq 0$ the interference term $F(\omega)$ introduces an energy dependence on the oscillations even in the non-interacting case, as expected since for $u = 0$ the difference in Fermi velocities can be directly mapped in difference in "effective path length" in the interferometer. The constructive/destructive interference will then depend on the absolute value of the kinetic energy as predicted by Eq.4.50.

[31] Note that in actual experiment the elastic regime is defined as the signal obtained when the linewidths of the injector and detector quantum dots overlap in energy. This does not necessarily results in a perfect $\delta(\epsilon - \epsilon')$ function. In a non-ideal case Eq. (4.46) here should be modified with electron retarded propagators at energies ϵ, ϵ' convoluted with $\rho_R(\epsilon)\rho_L(\epsilon')$, i.e. the (lorentzian) shapes of the Fano resonances in the QDs.

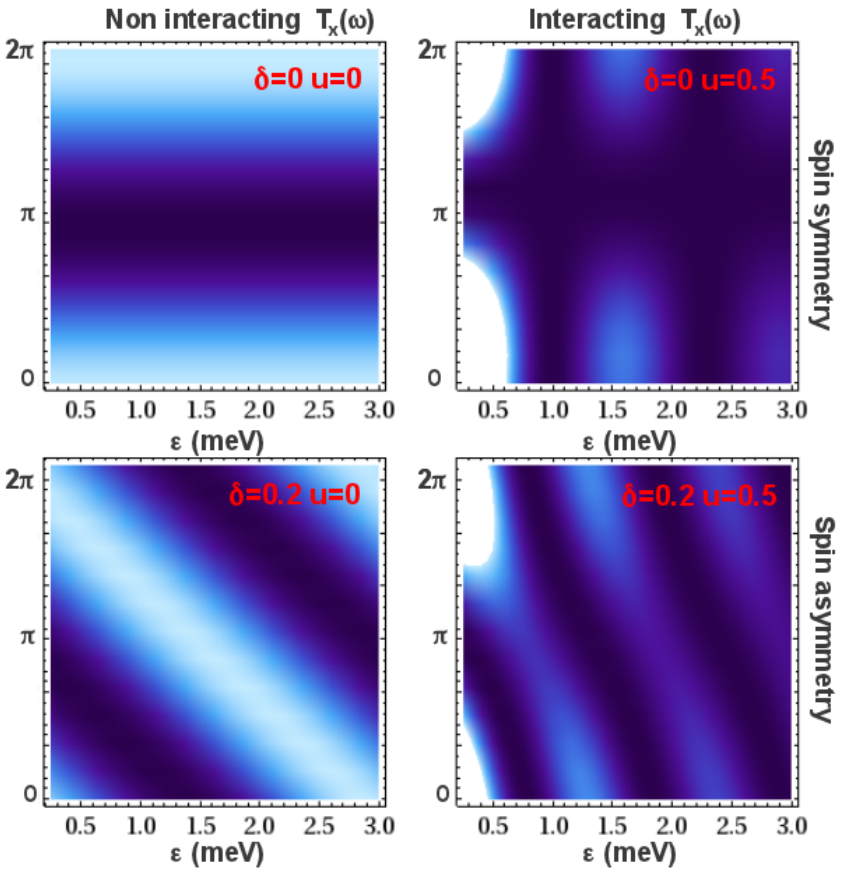

Figure 4.8: Elastic transmission coefficient for $\theta_R = \theta_L = \frac{\pi}{2}$ (lighter colors are closer to unity, darker closer to zero), in functions of energy and the phase difference $\phi = \phi_R - \phi_L$. Propagation distance has been taken to be $0.2\mu m$. Parameters of the model are the same as Fig.4.3, and crossed contributions to the current has been neglected (the plots start at 0.3 meV of the Fermi energy, so the NCA is justified)

For interacting channels the relevant velocities for the modes to propagate are v_+ and v_-, which reduce to $v_F + \delta v$ and $v_F - \delta v$ only for $u = w = 0$. This means that the period of oscillation, and the slope of the resonance in the (ϕ, ϵ)-plane are controlled by the u and w interaction parameters,[32] and the interferometric pattern can be significantly different from the non-interacting one (See Fig. 4.8).[33]

We discover then a very relevant impact of the interactions in the interferometer: the frequency and the shape of the oscillations is strongly dependent on the interactions, so that in principle a spin-interferometric experiment could give very accessible information (through the interferometric pattern) on the characteristics of the interaction between the ES (see Section 4.1.1). As discussed at the beginning of the Chapter, these interaction parameters are directly tunable through the control of the confinement potential, and in principle the inter-edge interaction w can be completely canceled in

[32] Although the intra-edge interaction determines the oscillations at long distances, the intra-edge interaction w is important for the progressive energy decrease of the signal.

[33] We note that interactions do introduce modifications also for short finite-range Coulomb potential ($r \neq 0$), but for high r ($r \gtrsim 0.1$) the quasiparticle contribution dominates. For what it concerns energy relaxation, the system behaves like a spinless chiral Luttinger liquid (the model that we would have for $\nu = 1$). Energy relaxation and single-particle Green's functions for this case have been studied in [154].

regions by separating edge channels by the cross-gate technique (Sect. 1.3.3) so that a real experiment could test our predictions and understand under which exact conditions the presented chiral TL model is fully valid, with great benefit for future effective modeling of IQH transport experiment.

Coherence and Quantum Information While this gedanken electronic device is interesting *per se*, it would be interesting to rephrase the transport problem in terms of basic quantum information theory, in order to answer the question of whether hot electrons traveling on interacting chiral edge channels can faithfully transfer spin-quantum information from one physical point to another, as desired in some quantum computing setups.

This task seems quite involved, as the final state of the electronic system after propagation is a collective, delocalized mode, so it is not clear whether the quantum information of interest can be easily isolated from the many-body state (this would be even more complicated in presence of inelasticity). Indeed, in the absence of spin-dependent extrinsic effects (such as fluctuating magnetic impurities) at zero temperature energy relaxation is the only dephasing mechanisms. The spin degree of freedom is entangled with the orbital state by construction: while this feature is interesting in view of engineered spin-manipulation (see Section 1.3.4) it implies that decoherence in the orbital sector entails decoherence of the spin-qubit as well.

We will not address this interesting problem here in its proper generality. We will limit ourselves to interprete the current formula as if the energetic electronic quasiparticle state and its spin would be well defined at the moment of injection and detection, as in the non-interacting case.

We are not formally introducing an external "bath" in our many-body problem, but we are interested only in some property (the spin) so there are many degrees of freedom of the system that can act as an environment. If we consider the transport of the quantum state from one point (dot L) to another (dot R) as a quantum gate, the transfer can be considered perfect as long as we interpret the decrease of the signal due to the coefficients $\Gamma_{s\sigma}$ as a probability of outcome on the result of the projection measurements of the qubit on the spin state that we want to transfer.[34]

The initial state of the electron injected in the channel has a well defined energy and spin $|\epsilon\rangle\,|s\rangle$. After propagation the electron is decomposed on the Fermi Sea which is left in a complex state consisting of many particle-hole excitations, that we picture *effectively* by considering that at the time of measurement we have different probabilities of finding the original electron in a given energy and spin state $|\epsilon'\rangle\,|s'\rangle$. This is clearly an oversimplified model, as in 1D the interacting eigenstates are collective waves, so this ansatz for the final state it is not necessarily exact even in the elastic limit.[35] In this single-particle view, the measured current signal can be interpreted as a projection measurement of this final state on the energy and spin subspaces corresponding to the configuration of dot L.

We can formalize this interpretation by considering the current signal as the expectation value of the operator

$$\hat{I}_{LR} \equiv \left(\frac{\mathbb{I} + \vec{\sigma}\cdot\hat{n}}{2}\right) \otimes |\epsilon\rangle\,\langle\epsilon| \ , \tag{4.52}$$

[34] See also the discussion on the non-interacting interpretation of the Fisher-Lee formula Eq.(4.33), on page 72.

[35] Note however that in the high-energy limits there are indications, for spin-less chiral Luttinger liquid, that the single-particle Green's functions can be very well approximated by semiclassical Green's functions where interactions are treated at the mean-field level[154]. By extension we might expect that at high energies also the spinful model will match the semiclassical limit where electronic quasiparticles are well-defined.

where the first term is projection on the spin-direction $\hat{n}$ (acting on the two dimensional Hilbert space of electronic spins, spanned by states $|\sigma\rangle = |\uparrow\rangle, |\downarrow\rangle$), and the second term represents a projection on the states of the many-body electron system which are degenerate at some energy ϵ. Formally this "energy projection" is responsible of a suppression for the signal since the final state has only a finite probability to be found in a given energy state at the time of measurement. However, the spin evolution due to the interaction is independent from this energy measurement because the Coulomb interaction Eq.(4.2), which is the only term in the Hamiltonian which could provide dephasing, does couple symmetrically to both spin-channels.

If the total density matrix of the system is ρ_{tot}, then $\left\langle \hat{I}_{LR} \right\rangle = \mathrm{Tr}_{\epsilon_n} \mathrm{Tr}_\sigma \left[\rho_{tot} \hat{I}_{LR} \right]$ $= \mathrm{Tr}_\sigma \left[\tau_S \left(\mathcal{P}_{\vec{n}} \right) \right]$, where

$$\tau_S = \langle \epsilon | \rho_{tot} | \epsilon \rangle = \sum_{\sigma\sigma'} \tau_{\sigma\sigma'} |\sigma\rangle \left\langle \sigma' \right| \ , \tag{4.53}$$

and we obtain

$$\left\langle \hat{I}_{LR} \right\rangle = \cos^2\left(\frac{\theta}{2}\right) \tau_{\uparrow\uparrow} + \sin^2\left(\frac{\theta}{2}\right) \tau_{\downarrow\downarrow} + \frac{1}{2} \sin\theta [e^{i\phi} \tau_{\uparrow\downarrow} + e^{-i\phi} \tau_{\downarrow\uparrow}] \ , \tag{4.54}$$

Note that τ_S is not the *reduced density matrix* of the system, as indeed it does not satisfy the identity $\tau_{\uparrow\uparrow} + \tau_{\downarrow\downarrow} = 1$. We can however normalize it and indeed obtain the reduced density matrix of the system which is at a given energy state ϵ and a given spin state $\hat{n}$:

$$\rho_{S,\epsilon} = \frac{\tau_S}{\mathrm{Tr}\left(\tau_S\right)} \ . \tag{4.55}$$

The quantity $\mathrm{Tr}\left(\tau_S\right)$ is indeed the probability of measuring the electron in a given energy state.

When dealing with qubits, the coherence of an initially pure state is typically evaluated by observing how its capability of interfering disappears with increasing time [148]. By analogy with quantum optics, in our steady-state transport equation we can test the spatial coherence [155], i.e. look at how the coherent properties of the current disappear as we increase the propagation distance (or equivalently the energy, because of Eq.(4.23)).

By making these considerations, looking at our steady-state solution Eq.(4.49), within the limits of our analogy it seems appropriate to identify the probabilities and the coherences of the density matrix $\rho_{S,\epsilon}^{\sigma\sigma'}$ appearing in Eq.(4.54) with the transport coefficients $M(\omega)$ and $F(\omega)$. By making this correspondence we obtain

$$\rho_S \simeq \begin{pmatrix} \cos^2\left(\frac{\theta}{2}\right) & \frac{F(\epsilon)}{2M(\epsilon)} \sin\theta e^{i\phi} \\ \frac{F(\epsilon)^*}{2M(\epsilon)} \sin\theta e^{-i\phi} & \sin^2\left(\frac{\theta}{2}\right) \end{pmatrix} \ . \tag{4.56}$$

We can now observe that in this interpretation we do not have "spin-decoherence" *stricto-sensu*. Despite $\frac{F(\epsilon)}{M(\epsilon)}$ being a non-trivial complex function, $\left|\frac{F(\epsilon)}{M(\epsilon)}\right|$ is always a constant equal to unity, and has no energy dependence. As mentioned already, in the context of spin-qubit transfer, this is analog to say that the interactions do modify the spin-precession, but do not induce spin-dephasing (despite a loss of the signal. See Fig. 4.9). We stress that the absence of decoherence in the elastic limit relies on a single-particle ansatz for the final electronic state, which has to be verified or improved by more detailed theories. Furthermore these considerations are also a consequence of the fact that interactions do not couple asymmetrically to the spin-sector of the Hilbert Space.

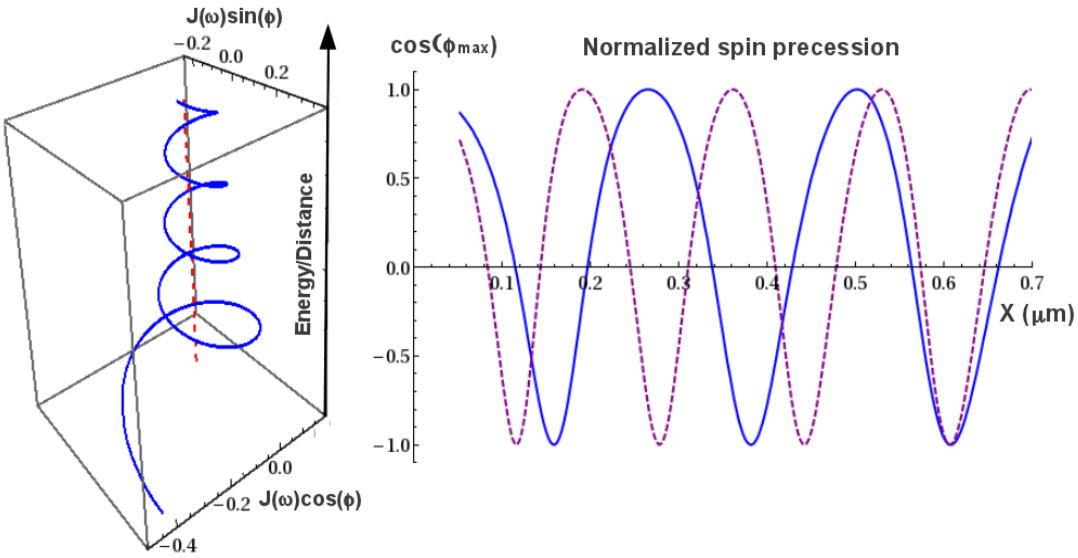

Figure 4.9: **Left panel**: Most-likely trajectory of the electronic state in the polar plane represented by the phase-angle ϕ, as a function of the distance of detection (or equivalently the energy of detection), for $\delta = 0.2$ and $u = 0.5\bar{v}$. The trajectory is defined by the ϕ which gives maximum of the current signal $J(\omega)$ computed through Eq.(4.46) for a given ϵ/L. **Right panel**: the value of ϕ which maximizes the current signal is compared with the non-interacting case (dashed line) as a function of distance of propagation at fixed energy ($\cos\phi$ is plotted).

Current research is in progress, aiming at the characterization of the proper spin-density matrices of the general, inelastic case, and to identify effective models of transport that could reproduce the features of the many-body treatment of the problem.

Final Summary and Conclusions

Edge states are transport channels which emerge in 2-dimensional electron gases under high-magnetic fields ("the integer Quantum Hall regime"). Because of their properties of topological protection, chirality and coherence, these states received much attention by the condensed matter community, which recognized their potential for exchange of quantum-information (flying qubits) in coherent nanoelectronic devices.

In this thesis we explored the unprecedented opportunity of controlling the quantum transport of electronic wavepackets delocalized over two co-propagating edge channels, which could lead to some new interesting applications for quantum interferometry (a scalable Mach-Zehnder interferometer) and transport of spin-qubit states. Adjacent chiral channels in wide Hall bars are usually independent and selectively populated, but there are several indications that the channels might be coupled in a coherent way by means of abruptly varying electric potentials, or external localized magnetic fields. We explored this idea by assessing the effectiveness of several mechanisms of coherent mixing between edge states which might be either spin-degenerate or spin-resolved, and we examined the experimental attempts to realize such couplings by developing simulations that aim to explain the features of transport of electrons mixed between more than one channel.

In the first chapter of the thesis we introduced in detail the edge states a the properties of edge states and the analytical models that can be used to describe their physics. The non-interacting theory has been used to properly evaluate the effect of sharp potentials (local, non-adiabatic variations of the energy landscape in the electron gas) that are supposed to be able to coherently mix the channels. We explained the Landauer-Buttiker transport model for edge states and conventional and new, non-conventional interferometric setups.

In the second chapter we computed the scattering-matrices of these sharp "potential steps", carefully matching the propagating and evanescent solutions of the Schrödinger equation in a 2-dimensional model of the Hall bars. The numerical results of this mode-matching technique show that potential variations whose energies are smaller than the Landau gap are able to mix only few percent of the current. However some architectural strategies are identified in order to tune the mixing up to be useful for quantum-information purposes; more precisely we discussed the effects of high-energy steps, of the sequential operation of several independent mixers, and of the constructive interference effect that might arise by controlling the electronic phases during propagation (for example through the periodic poling technique).

The mode-matching technique was improved in chapter 3 of the thesis, which presented a numerical approach based on Green's functions (and still the Landauer-Buttiker formalism) which is applied to evaluate the cross-over to adiabaticity of electric potentials and to model two experiments which have been conducted at NEST laboratory of Scuola Normale Superiore di Pisa. In one experiment, the charge transfer between two spin-degenerate edge channels of variable length is measured by means of the scanning gate technology. Simulations of the disordered Hall bar are able to reproduce the main features of the experimental finding, and to deduce the presence of dephasing effects in the system. As for the second experiment, we numerically modeled spin-resolved edge channels which are under the influence of periodic nanomagnets. We confirmed the results of first-order perturbation theory with simulations, and we

analyzed the interplay of the effect of an electric potential applied together with the periodic magnetic modulations in order to predict useful effects for future electronic spin-interferometers.

Finally we deepened the study of spin-state transport in edge channels by examining the effect of Coulomb interactions among electrons in chapter 4. An effective 1-dimensional model of interacting edge states based on the Tomonaga-Luttinger model has been presented and its properties were derived by the bosonization technique. By means of non-equilibrium Green's function formalism for quantum transport in interacting regions, adapted to high-energy interacting chiral edge channels through the application and assessment of the non-crossing approximation, a spin-interferometry idealized transport experiment has been discussed. We found that the interactions can have a strong influence on the interferometric pattern.

We conclude the thesis document by attaching a list published articles, pre-prints and works in progress which resulted out of the work during the Ph.D program carried out at CNRS/UJF Institut NEEL, SISSA and Scuola Normale Superiore.

Appendices

Appendix I: Details on the Simulated Hall Bar for the Periodic Poling Technique

By means of the KNIT tight-binding simulation package [57], we can easily build a discrete system of arbitrary geometry. The simulated Hall bar has been designed to allow the edge channels to take advantage or their topological protection against backscattering (they are well decoupled traveling on opposite sides) and by providing sufficient free-propagation zones for allowing selective population and efficient decoupling of the scattering zone from the leads of the system. More precisely, the Hall-bar width has been taken to be 98.57 nm, corresponding to 8.36 magnetic lengths. This width is discretized in $M = 35$ points, such that the lattice spacing is $a = 2.816$ nm, which wells justifies the Peierls' approximation (see Section 3.1).

The complete tight-binding system is obtained by assembling the region with the array of nanomagnets (whose extension is $\lambda N + 2M$, following the notations of Section 3.3) with blocks of $M \times M$ sites in such a way to create a four-terminal device.

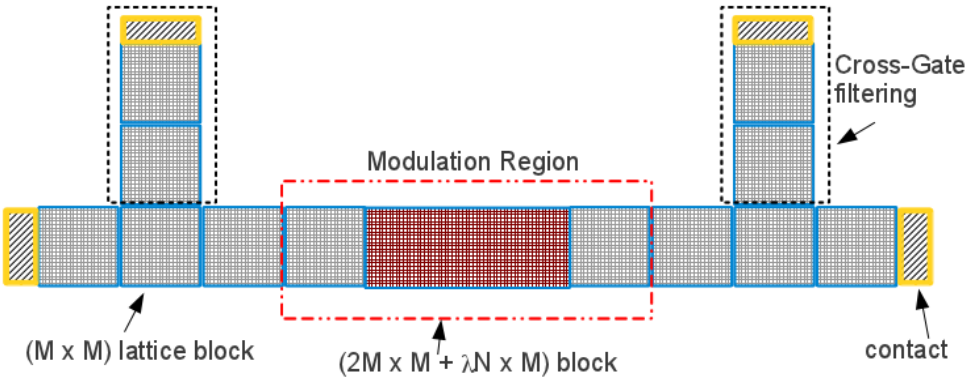

Figure 4.10: Schematics of the simulated Hall Bar, in terms of block of sites. The cross-gate regions are realized raising the onsite energy terms up to allowing only one channel to pass. The modulation region is attached in the center of the transport setup, and has different size for each realized numerical experiment.

Appendix II: Analytical Form of Interacting Green's Function

In this appendix we derive the analytic form of the single-particle Green's function in the space-energy representation, Eq. (4.23). We need to compute the Fourier Transform of the following propagator (see Eq. (4.22)):

$$\mathcal{G}_{\sigma}^{>}(x,t)=\frac{e^{ik_F^{\sigma}x}}{2\pi}\frac{1}{(x-v_+t+ir)^{\frac{1}{2}+\sigma\delta}}\frac{1}{(x-v_-t+ir)^{\frac{1}{2}-\sigma\delta}}\,. \tag{4.57}$$

By exploiting the convolution conventions,[36] Eq. (4.57) after Fourier Transform takes the form:

$$\mathcal{G}_{\sigma}^{>}(x,\omega)=\frac{e^{ik_{\sigma}x}}{2\pi}\int\frac{d\omega'}{2\pi}F_{-}^{\frac{1}{2}-\sigma\delta}\left(x,\omega'+\frac{\omega}{2}\right)F_{+}^{\frac{1}{2}+\sigma\delta}\left(x,\frac{\omega}{2}-\omega'\right)\,, \tag{4.58}$$

where $F_{\pm}^{\alpha}(x,\omega)=v_{\pm}^{-1}\exp(i\omega x v_{\pm}^{-1})\int_{-\infty}^{+\infty}dt(t+ir)^{-\alpha}e^{-iv_{\pm}^{-1}\omega t}$ is an integral which has an analytic form for $\alpha<1$ [66]:

$$\int_{-\infty}^{+\infty}dz\frac{e^{\pm i\frac{\omega}{v}z}}{(z\mp ir)^{\alpha}}=(\pm i)^{\alpha}\,\frac{2\pi}{\Gamma(\alpha)}\Theta(\omega)\left(\frac{\omega}{v}\right)^{\alpha-1}e^{-\frac{r\omega}{v}}\,, \tag{4.59}$$

where $\Gamma(x)$ is the Euler's Gamma function. Convolving these functions leads to the integral form of the Green's function:

$$\mathcal{G}_{\sigma}^{>}(x,\omega)\propto -ie^{ik_F^{\sigma}x}e^{i\frac{\omega}{2}z\rho}\int_{-\omega}^{+\omega}\frac{e^{i\frac{\epsilon}{2}z\tau}}{(\epsilon+\omega)^{\frac{1}{2}+\sigma\delta}(\omega-\epsilon)^{\frac{1}{2}-\sigma\delta}}d\epsilon\,, \tag{4.60}$$

in which we disregarded proportionality factors (that will be absorbed in the correct normalization of the Green's function which depends on the cut-off) and we noted $z=x+ir$, $\rho=v_+^{-1}+v_-^{-1}$ amd $\tau=v_+^{-1}-v_-^{-1}$. By some simple algebraic manipulations we can cast Eq. (4.60) in the form of the integral representation of the Confluent Hypergeometric Function ${}^1F_1$ (or Φ, as we called in the text): $\Phi(a,b,c)\propto\int_0^1 d\xi e^{z\xi}\xi^{a-1}(1-\xi)^{b-a-1}$. Taking the limit $r\to 0$ we arrive at Eq. (4.23):

$$\mathcal{G}_{\sigma}^{>}(x,\omega)\propto -ie^{i\omega\frac{x}{v_-}}\Phi(\frac{1}{2}-\sigma\delta,\,1,\,-ix\tau)\,. \tag{4.61}$$

We note that the $\delta=0$ limit gives the result known in the literature [125] $\mathcal{G}_{\sigma}^{>}(x,\omega;\,\delta=0)\propto e^{i\omega x\rho}J_0\left(\frac{x\omega}{2}\tau\right)$.

[36] $\int dt\, f_1(x,t)\, f_2(x,t)\, e^{i(\omega t-kx)}=\int\frac{d\omega'}{2\pi}\, f_1(x,\omega')\, f_2(x,\omega-\omega')$

Appendix III: Effective Interactions of the TL Model

In this appendix we turn the attention to the effective Coulomb interaction in the TL model. The bosonization procedure that we employed for the Green's functions (Section 4.1.2) is an algebraic shortcut to unveil some remarkable mathematical properties of the TL model that can also be discovered by diagrammatic perturbation analysis on the electron-electron interactions.

In a diagrammatic interacting theory, which will be very quickly reviewed in Section 4.2.3 for an electronic transport problem, the *effective interaction* is the formal "propagator" which connects two Fermionic Green's functions, which is usually indicated in diagrams as a thick wiggled line. The perturbative development given can be arranged for the interaction propagators in recursive relations in the spirit of Dyson's equations, and one striking consequence of linear dispersion relation is that the effective interaction among electrons is *exactly* given by the result given by the diagrammatic Random-Phase-Approximation (RPA) on the interaction lines (see Fig.4.11). Noting the *irreducible polarization bubble* as $\Pi_\sigma = \Pi_\sigma(k,\omega)$ [66], RPA dictates the absence of vertex corrections in the polarization, so that the interaction lines are only renormalized by the irreducible bubbles. In our chiral TL model we can even replace the interacting polarization bubble with the bare ones [87]

$$\begin{aligned}\Pi^0_\sigma(k,\omega) &= -\frac{i}{\hbar}\int\frac{dp}{2\pi}\int\frac{d\epsilon}{2\pi}G^T_{\sigma 0}(k+p,\omega+\epsilon)G^T_{\sigma 0}(p,\epsilon)\\ &= \frac{1}{2\pi\hbar}\frac{(k-k_F^\sigma)}{\omega - v_F^\sigma\left(k-k_F^\sigma\right)+i0^+\mathrm{sign}(\omega)}\ .\end{aligned} \tag{4.62}$$

Figure 4.11: Diagrammatic view of the Dyson's equation for the interaction propagators. Single wiggles represent bare interactions (u for $\sigma=\sigma'$ or w for $\sigma\neq\sigma'$) while double wiggled lines represent full propagators D (4.63)-(4.64). Irreducible polarization bubbles are actually the free ones $\Pi_\sigma = \Pi^0_\sigma$ described in Eq.(4.62).

The "bare" interactions u and w get renormalized and generate the following effective interactions for same ($D_\parallel$) or different spins ($D_\perp$):

$$D_\perp^{\sigma,-\sigma}(k,\omega) = \frac{u+uw\left(\Pi_\sigma-\Pi_{-\sigma}\right)}{\left(1-w\Pi_\sigma\right)\left(1-w\Pi_{-\sigma}\right)-u^2\Pi_\sigma\Pi_{-\sigma}} \tag{4.63}$$

$$D_\parallel^{\sigma,\sigma}(k,\omega) = \frac{w-w^2\Pi_\sigma+u^2\Pi_{-\sigma}}{\left(1-w\Pi_\sigma\right)\left(1-w\Pi_{-\sigma}\right)-u^2\Pi_\sigma\Pi_{-\sigma}} \tag{4.64}$$

In the following sections we will need the effective interactions for $\omega=0$. We note that $\Pi^0_\sigma(k,\omega=0) = -\left(2\pi\hbar v_F^\sigma\right)^{-1}$, which means that the renormalized interactions $\tilde{w}$ and $\tilde{u}$ remain local in space, but are in general weakened with respect to their bare values. To get an idea, for $u=w=v_F/2$ and $\delta v \simeq v_F/5$, at first order in δv we get $\tilde{u}_{\downarrow\uparrow}=\tilde{w}_{\uparrow\uparrow}\simeq 0.45v_F$, $\tilde{u}_{\uparrow\downarrow}=\tilde{w}_{\downarrow\downarrow}=0.42v_F$. For $\delta v\neq 0$, the effective interactions are manifestly spin-dependent.

These results on the effective interactions are important for evaluating the interaction propagator in the elastic limit in the "crossed diagrams" discussed in Section 4.2.4.

List of publications, pre-prints and works in progress

Published Papers

1. **Edge channel mixing induced by potential steps in an integer quantum Hall system**, D. Venturelli, V. Giovannetti, F. Taddei, and R. Fazio, D. Feinberg, G. Usaj and C. A. Balseiro , Phys. Rev. B **83**, 075315 (2011) *[chapter 2 and 3]*

2. **Spatially resolved analysis of edge-channel equilibration in quantum Hall circuits**, N. Paradiso, S. Heun, S. Roddaro, D. Venturelli, F. Taddei, V. Giovannetti, R. Fazio, G. Biasiol, L. Sorba, F. Beltram, Phys. Rev. B **83**, 075315 (2011) *[printed in chapter 3]*

3. **Controlled coupling of spin-resolved quantum Hall edge states**, B. Karmakar, D. Venturelli, L. Chirolli, F. Taddei, V. Giovannetti, R. Fazio, S. Roddaro, G. Biasiol, L. Sorba, V. Pellegrini, F. Beltram, to appear in Phys. Rev. Lett. (2011) *[printed in chapter 3]*

4. **Dissipative spin dynamics near a quantum critical point: Numerical Renormalization Group and Majorana diagrammatics**, S. Florens, A. Freyn, D. Venturelli, R. Narayanan, Phys. Rev. B **84**, 155110 (2011) *[not discussed in the thesis, arXiv:1106.2655]*

Under Preparation

1. **Elastic spin-qubit transport by interacting electrons in integer quantum Hall channels**, D. Venturelli, D. Feinberg *[chapter 4]*

2. **Datta-Das transistor in the Integer Quantum Hall Regime**, L. Chirolli, D. Venturelli, F. Taddei, R. Fazio, and V. Giovannetti *[not discussed in the thesis]*

Acknowledgements

I would like to thank the many people which have been important to me, both professionally and personally, during this four-year period that I spent in Grenoble, Pisa and Trieste.

It has been a great pleasure for me to work with thesis advisors Denis Feinberg, Rosario Fazio, Vittorio Giovannetti and Fabio Taddei. Despite my stubborn personality, they guided me towards learning how to produce a scientifically sound work, and thanks to their informal, but serious, attitude they granted me a great human experience as well.

My experience in Grenoble at NEEL was enriched by the meaningful interaction with a number of collegues, friends and senior collaborators. Among them I want to mention Serge Florens whose approach to science is a constant inspiration for me, and Axel Freyn to whom I owe so many favors that I am sure I will never be able to break-even.

In Pisa, my stay in the QTI group has been delighful. I want to thank particularly the collegues in my room (Amit Agarwal, Davide Rossini and Antonella de Pasquale, and the occasionally present Pietro Silvi), the friend Stefano Pugnetti which is always a reference for me for anything, and my collaborator Luca Chirolli for his patience and teamwork.

I thank the institutions SISSA in Trieste and Centro Balseiro in S.Carlos de Bariloche which hosted my stays for several months. I am very fond of the period spent in Trieste, where I met great scientists, teachers, and future collegues I hope. In Argentina I had the outstanding opportunity to establish my first "overseas" collaboration, and I can truly say that that short stay made a great difference both for my Ph.D and my life.

I am also deeply grateful to the committee that will judge my thesis, and especially the referees Thierry Martin and Pascal Degiovanni which spent their precious time reading the manuscript despite the short notice and the summer time constraints.

Finally my thoughts and thanks go to those who, although not scientists or collegues, have always been close to me in the soft and hard times :) This includes of course my parents and grandparents, which insist on spoiling me as much as they can despite I'm not a child anymore. My everlasting friends from Modena (Giombo, Giacomo, Stanza, Stefania...), my new close friends in Pisa (Lorenzo, Falco, Marta, Angela...) and my virtual and far friends scattered around the world (Maria Adele, Jz, Katie, Sarah, Alice, Raffo, Carmelo...) are all I needed to be happy, and I am grateful of their friendship.

Bibliography

[1] D. K. Ferry, S. M. Goodnick and J. Bird - "Transport in Nanostructures" - Cambridge University Press (2009)

[2] Y. V. Nazarov and Y. M. Blanter - "Quantum Transport: Introduction to Nanoscience" - Cambridge University Press (2009)

[3] Richard E. Prange - Steven M. Girvin - "The Quantum Hall Effect" - Springer-Verlag New York (1986)

[4] G. Montambaux - "Semiclassical quantization of skipping orbits" - Eur. Phys. J. B. Volume 79, Number 2, 215-224 (2011)

[5] M. O. Goerbig - "Quantum Hall Effects" - Lecture notes for the Singapore session "Ultracold Gases and Quantum Information" of Les Houches Summer School, 2009

[6] O. Olendski, L. Mikhailovska - "Curved quantum waveguides in uniform magnetic fields" - Phys. Rev. B **72**, 235314 (2005)

[7] A. Erdely and H. Bateman - "Higher Trascendental Functions" - McGraw Hill (1954)

[8] A.H. MacDonald, P. Streda - "Quantized Hall effect and edge currents" - Phys. Rev. B **29**, 1616 (1984)

[9] J. C. Barbosa, P. N. Butcher - "The behaviour of the propagating and evanescent modes of a 2D quantum wire in a perpendicular magnetic field" - Superlattices and Microstructures, Vol. 22, No. 3, 1997

[10] J. J. Palacios and C. Tejedor - "Mode-matching technique for transmission calculations in electron waveguides at high magnetic fields" - Phys. Rev. B 48, 5386 (1993)

[11] J. J. Palacios and C. Tejedor - "Effects of geometry on edge states in magnetic fields: Adiabatic and nonadiabatic behavior" - Phys. Rev. B 45, 9059 (1992)

[12] Tsai-Yu Huanga, Yu-Ming Chenga, C. -T. Liang, Gil-Ho Kim and J. Y. Leem - "Exchange-enhanced Landé g-factor, effective disorder and collapse of spin-splitting in a two-dimensional GaAs electron system" - Physica E Vol. **12**, 424 (2002)

[13] J. F. Janak - "g Factor of the Two-Dimensional Interacting Electron Gas" - Phys. Rev. 178, 1416 (1968)

[14] T. Ando and Y. Uemura - "Theory of Oscillatory g Factor in an MOS Inversion Layer under Strong Magnetic Fields" - J. Phys. Soc. Jap. 37, 1044 (1974)

[15] R. Landauer, IBM J. Res. Dev. **32**, 306 (1988), and references therein.

[16] M. Di Ventra - "Electrical Transport in Nanoscale Systems" - Cambridge University Press (2008)

[17] I. Bartos, B. Rosenstein - "Landau level gap reduction at abrupt edges" - Modern Physics Letters B **8** 1185 (1994)

[18] L. I. Glazman and M. Jonson - "Global adiabatic regime in quantum ballistic transport" - Phys. Rev. B 41, 10686 (1990)

[19] P. Ramvall, Qinghong Du, Hongqi Xu, L. Samuelson, and P. Omling - "Effects of interchannel coupling in a two-dimensional electron gas at high magnetic fields" - Phys. Rev. B **53**, 1933 (1996)

[20] R. J. F. van Haren, F. A. P. Blom, W. de Lange, and J. H. Wolter - "Separation of edge channels by a macroscopic distance in a half-gated GaAs/AlxGa1-xAs heterostructure" - Phys. Rev. B **47**, 15700 (1993)

[21] S. Komiyama, H. Hirai, M. Ohsawa, and Y. Matsuda, S. Sasa and T. Fujii - "Inter-edge-state scattering and nonlinear effects in a two-dimensional electron gas at high magnetic fields" - Phys. Rev. B **45**, 11085 (1992)

[22] G. Muller, D. Weiss, A. V. Khaetskii, K. von Klitzing, S. Koch, H. Nickel, W. Schlapp, and R. Lösch - "Equilibration length of electrons in spin-polarized edge channels" - Phys. Rev. B **45**, 3932 (1992)

[23] Yang Ji, Yunchul Chung, D. Sprinzak, M. Heiblum, D. Mahalu, Hadas Shtrikman - "An electronic Mach-Zehnder interferometer" - Nature **422**, 415 (2003)

[24] "Interference between two indistinguishable electrons from independent sources" - I. Neder, N. Ofek, Y. Chung, M. Heiblum, D. Mahalu, V. Umansky Nature **448**, 333 (2007)

[25] Preden Roulleau, F. Portier, P. Roche, A. Cavanna, G. Faini, U. Gennser, and D. Mailly - "Direct Measurement of the Coherence Length of Edge States in the Integer Quantum Hall Regime" - Phys. Rev. Lett. 100, 126802 (2008)

[26] Vittorio Giovannetti, Fabio Taddei, Diego Frustaglia, and Rosario Fazio - "Multichannel architecture for electronic quantum Hall interferometry" - Phys. Rev. B 77, 155320 (2008)

[27] I. Neder, M. Heiblum, Y. Levinson, D. Mahalu, and V. Umansky - "Unexpected Behavior in a Two-Path Electron Interferometer" - Phys. Rev. Lett. **96**, 016804 (2006).

[28] Bertoni, A., Bordone, P., Brunetti, R., Jacoboni, C. and Reggiani, S. - "Quantum logic gates based on coherent electron transport in quantum wires" - Phys. Rev. Lett. **84**, 5912 (2001)

[29] Eugene P. Wigner - "The Problem of Measurement" - American Journal of Physics – January 1963 – Volume 31, Issue 1, pp. 6

[30] Radu Ionicioiu and Irene D'Amico, "Mesoscopic Stern-Gerlach device to polarize spin currents", Phys. Rev. B **67**, 041307(R) (2003)

[31] A G Klein and S A Werner - "Neutron Optics" - 1983 Rep. Prog. Phys. **46** 259

[32] P. Simon and D. Feinberg -"Electronic Spin Precession and Interferometry from Spin-Orbital Entanglement in a Double Quantum Dot" - Phys. Rev. Lett. **97**, 247207 (2006)

[33] P. Stano and P. Jacquod - "Spin-dependent tunneling into an empty lateral quantum dot" - Phys. Rev. B 82, 125309 (2010)

[34] T. M. Stace, C. H. W. Barnes, and G. J. Milburn, Phys. Rev. Lett. 93, 126804

[35] J. M. Taylor, H.-A. Engel, W. Dür, A. Yacoby, C. M. Marcus, P. Zoller and M. D. Lukin - "Fault-tolerant architecture for quantum computation using electrically controlled semiconductor spins" - Nature Physics **1**, 177 (2005)

[36] D. Diaconescu, A. Goldschmidt, D. Reuter, and A. D. Wieck -"Quantum Hall effect in long and in mobility adjusted GaAs/Alx Ga1–xAs samples"- Phys. Stat. Sol. (b) **245**, 276 (2008);

[37] R. Haug, A. D. Wieck, K. von Klitzing, and K. Ploog -"Magnetotransport properties of hall-bar with focused-ion-beam written in-plane-gate"- Physica B **184**, 192 (1993).

[38] A. A. Shashkin, V. T. Dolgopolov, E. V. Deviatov, B. Irmer, A. G. C. Haubrich, J. P. Kotthaus, M. Bicher, and W. Wegscheider -"Lateral tunneling through the controlled barrier between edge channels in a two-dimensional electron system"- JETP Lett. **69**, 603 (1999).

[39] C. Riedesel, D. Reuter and A. D. Wieck - "Laterally patterned high mobility two-dimensional electron gases obtained by overgrowth of focused ion beam implanted Al1—xGaxAs" - Physica E Vol. **21**, 592 (2004)

[40] Y. Takagaki and K. H. Ploog - "Tunneling spectroscopy of Landau levels at the edge of a quantum Hall system" - Phys. Rev. B **62**, 3766 (2000)

[41] M. Huber, M. Grayson, M. Rother, W. Biberacher, W. Wegscheider, and G. Abstreiter -"Structure of a Single Sharp Quantum Hall Edge Probed by Momentum-Resolved Tunneling"- Phys. Rev. Lett. **94**, 016805 (2005).

[42] Fejer, M. M., Magel, G. A., Jundt, D. H. and Byer - "Quasi-phase-matched second harmonic generation: tuning and tolerances" - R. L. IEEE J. Quantum Electron. **28**, 2631 (1992).

[43] Kouwenhoven, L. P. and Hekking, F. W. J. and van Wees, B. J. and Harmans, C. J. P. M. and Timmering, C. E. and Foxon, C. T. - "Transport through a finite one-dimensional crystal" - Phys. Rev. Lett. **65**, 361 (1990)

[44] Ulloa, Sergio E. and Castao, Eleuterio and Kirczenow, George - "Ballistic transport in a novel one-dimensional superlattice" - Phys. Rev. B **41**, 12350 (1990)

[45] Leng, M. and Lent, C. S. - "Recovery of quantized ballistic conductance in a periodically modulated channel" - Phys. Rev. Lett. **71**, 137 (1993)

[46] R. Feynman - "The Feynman Lectures on Physics, Vol. 3" - Addison Wesley (1971)

[47] William H. Press, Saul A. Teukolsky, William T. Vetterling, Brian P. Flannery - "Numerical Recipes 3rd Edition: The Art of Scientific Computing" - Cambridge University Press (2007)

[48] Daniel S. Fisher and Patrick A. Lee - "Relation between conductivity and transmission matrix" - Phys. Rev. B **23**, 6851 (1981)

[49] H. U. Baranger and A. D. Stone - "Electrical linear-response theory in an arbitrary magnetic-field - a new fermi-surface formation" - Phys. Rev. B **40**, 8169 (1989).

[50] M. Wimmer - "Quantum transport in nanostructures: From computational concepts to spintronics in graphene and magnetic tunnel junctions" - Ph.D. Thesis Univ. Regensburg

[51] Gonzalo Usaj - Edge states interferometry and spin rotations in zigzag graphene nanoribbons - Phys. Rev. B **80**, 081414(R) (2009)

[52] A. Reynoso, Gonzalo Usaj, M. J. Sánchez, and C. A. Balseiro - "Theory of edge states in systems with Rashba spin-orbit coupling" - Phys. Rev. B **70**, 235344 (2004)

[53] J.-U. Bae , T.-Y. Lin , Y. Yoon , S. J. Kim , J. P. Bird , A. Imre , W. Porod , and J. L. Reno - "Characterization of Nanomagnet Fringing Fields in Hybrid Semiconductor/Ferromagnetic Devices" - IEEE Transactions on Magnetics, Vol. **44**, 4706 (2008)

[54] S. Sanvito, C. J. Lambert, J. H. Jefferson, A. M. Bratkovsky -"General Green's-function formalism for transport calculations with spd Hamiltonians and giant magnetoresistance in Co- and Ni-based magnetic multilayers"- Phys. Rev. B **59**, 11936 (1999)

[55] B.W. Alphenaar, P.L. McEuen, R.G. Wheelera and R.N. Sacksb - "The influence of impurities on inter-Landau-level equilibration" - Physica B **175**, 235 (1991)

[56] A. Würtz, R. Wildfeuer, A. Lorke, E. V. Deviatov, and V. T. Dolgopolov - "Separately contacted edge states: A spectroscopic tool for the investigation of the quantum Hall effect" - Phys. Rev. B **65**, 075303 (2002)

[57] K. Kazymyrenko and X. Waintal - "Knitting algorithm for calculating Green functions in quantum systems" - Phys. Rev. B 77, 115119 (2008)

[58] Nicola Paradiso, Stefan Heun, Stefano Roddaro, Davide Venturelli, Fabio Taddei, Vittorio Giovannetti, Rosario Fazio, Giorgio Biasiol, Lucia Sorba, and Fabio Beltram - "Spatially resolved analysis of edge-channel equilibration in quantum Hall circuits" - Phys. Rev. B **83**, 155305

[59] N. Paradiso, S. Heun, S. Roddaro, L. N. Pfeiffer, K. W. West, L. Sorba, G. Biasol, F. Beltram - "Selective Control of edge-channel trajectories by scanning gate microscopy" - Physica E 42 (2010) 1038 - 1041

[60] E. V. Deviatov and A. Lorke - "Experimental realization of a Fabry-Perot-type interferometer by copropagating edge states in the quantum Hall regime" - Phys. Rev. B 77, 161302(R) (2008)

[61] T. Martin and S. Feng - "Suppression of Scattering in Electron Transport in Mesoscopic Quantum Hall Systems" - Phys. Rev. Lett. 64, 1971 (1990)

[62] J. A. Nixon and J. H. Davies - "Potential fluctuations in heterostructures devices" - Phys. Rev. B, 7929 (1990)

[63] Tohru Kawarabayashia, Yoshiyuki Onoa, Tomi Ohtsukib, Stefan Kettemannc, Alexander Struckd and Bernhard Kramere - "Quantum transport properties of quantum Hall wires in the presence of correlated disorder" - Physica E, Vol. **40**, 1072 (2008)

[64] N. Paradiso, S. Heun, S. Roddaro, L. N. Pfeiffer, K. W. West, L. Sorba, G. Biasiol, and F. Beltram - "Selective control of edge-channel trajectories by scanning gate microscopy" - Physica E **42** 1038 (2010)

[65] H. Bruus, K. Flensberg - "Many-Body Quantum Theory in Condensed Matter Physics" - Oxford University Press (2006)

[66] G. F. Giuliani and G. Vignale - "Quantum Theory of the Electron Liquid" - Cambridge University Press (2005)

[67] A. M. Zagoskin - "Quantum Theory of Many-Body Systems, Techniques and Applications" - Springer-Verlag (1998)

[68] S. Datta - "Electronic Transport in Mesoscopic Systems" - Cambridge University Press (2007)

[69] Yigal Meir, Ned S. Wingreen - " Landauer formula for the current through an interacting electron region"- Phys. Rev. Lett. **68**, 2512–2515

[70] H. Haug and A.-P. Jahuo - "Quantum Kinetics in Transport and Optics of Semiconductors" - Springer, Berlin (1996).

[71] P. A. Mello, Y. Imry and B. Shapiro - "Model for phase breaking in the electronic conduction in mesoscopic systems" - Phys. Rev. B 61, 16570 (2000)

[72] M. Mosko, P. Vagner, P. Markos, T. Schapers - "Decoherence of coherent transport in a disordered one-dimensional wire: Phenomenological model" - cond-mat/0111116v1 (2001)

[73] Y. Imry, O. Entin-Wohlman, A. Aharony - "Landauer transport with inelastic scattering" - Europhys. Lett. **72**, 263 (2005)

[74] S. Feng - "Quantum Transport in the presence of phase-breaking scattering: generalized landauer formula" - Phys. Lett. A 143, 400 (1990)

[75] D. Craik - "Magnetism: Principles and Applications" - Wiley (1997)

[76] J.-U. Bae , T.-Y. Lin , Y. Yoon , S. J. Kim , J. P. Bird , A. Imre , W. Porod , and J. L. Reno - "Characterization of Nanomagnet Fringing Fields in Hybrid Semiconductor/Ferromagnetic Devices" - IEEE TRANSACTIONS ON MAGNETICS, VOL. 44, NO. 12, (2008)

[77] Alain Nogaret J. Phys. - "Electron dynamics in inhomogeneous magnetic fields" - Condens. Matter 22 253201 (2010)

[78] Y. Acremann, T. Heinzel, and K. Ensslin, E. Gini and H. Melchior, M. Holland - "Individual scatterers as microscopic origin of equilibration between spin-polarized edge channels in the quantum Hall regime" - Phys. Rev. B **59**, 2116 (1999)

[79] Roulleau, P. and Portier, F. and Roche, P. and Cavanna, A. and Faini, G. and Gennser, U. and Mailly, D. - "Noise Dephasing in Edge States of the Integer Quantum Hall Regime" - Phys. Rev. Lett. **101**, 186803 (2008)

[80] S. Ihnatsenka and I. V. Zozoulenko - "Spatial spin polarization and suppression of compressible edge channels in the integer quantum Hall regime" - Phys. Rev. B **73**, 155314 (2006)

[81] I. E. Dzyaloshinskii and A. I. Larkin - “Correlation functions for a one-dimensional Fermi system with long-range interaction (Tomonaga model)” - Zh. Eksp. Teor. Fiz. 65, 411-426 (1973)

[82] J. Voit - “One-Dimensional Fermi liquids” - Rep. Prog. Phys. 57 (1994)

[83] H. C. Lee, S. R. E. Yang - “Spin-charge separation in quantum Hall edge liquids” - Phys. Rev. B 56, R15529 (1997)

[84] T. Giamarchi - “Quantum Physics in One Dimension” - Oxford University Press (2006)

[85] M. Abramowitz, I. A. Stegun - “Handbook of Mathematical Functions” - New York: Dover Publications (1972)

[86] J. Solyom - “The Fermi gas model of one-dimensional conductors” - Advances in Physics, vol.28, 201 (1979)

[87] D. Maslov - Lecture notes: "Fundamental Aspects of Electron Correlations and Quantum Transport in One-Dimensional Systems" - LXXI Les Houches Summer School (2004)

[88] Walter Metzner, Claudio Castellani, Carlo Di Castro - “Fermi systems with strong forward scattering” - Advances in Physics, vol. 47, 317 (1998)

[89] U. Zulicke and A. H. MacDonald - ”Plasmon modes and correlation functions in quantum wires and Hall bars“ - Phys. Rev. B **54**, 16813 (1996)

[90] A. H. MacDonald - “Compressible Strips, Chiral Luttinger Liquids, and All That Jazz” - Braz. J. Phys. 26, 43 (1996)

[91] B. I. Halperin - ”Quantized Hall conductance, current-carrying edge states, and the existence of extended states in a two-dimensional disordered potential” - Phys. Rev. B 25, 2185 (1982)

[92] D. B. Chklovskii, B. I. Shklovskii and L. I. Glazman - “Electrostatics of edge channels” - Phys. Rev. B, **46** 4026 (1992)

[93] A. Siddiki - ”The spin–split incompressible edge states within empirical Hartree approximation at intermediately large Hall samples” - Physica E Vol. **40** 1124 (2008)

[94] D. Eksi, E. Cicek, A. I. Mese, S. Aktas, A. Siddiki, and T. Hakioğlu - ”Theoretical investigation of the effect of sample properties on the electron velocity in quantum Hall bars” - Phys. Rev. B **76**, 075334 (2007)

[95] A. Siddiki and Rolf R. Gerhardts - Thomas-Fermi-Poisson theory of screening for laterally confined and unconfined two-dimensional electron systems in strong magnetic fields” - Phys. Rev. B **68**, 125315 (2003)

[96] I. L. Aleiner and L. I. Glazman - ”Novel edge excitations of two-dimensional electron liquid in a magnetic field” -Phys. Rev. Lett. **72**, 2935 (1994)

[97] J. H. Han - ”Green’s-function approach to the edge spectral density” - Phys. Rev. B **56**, 15806 (1997)

[98] S. Conti, G. Vignale -”Collective modes and electronic spectral function in smooth edges of quantum hall systems”- Phys. Rev. B **54**, R14309 (1996)

[99] S. Takei, M. Milletarì, and B. Rosenow - "Nonequilibrium electron spectroscopy of Luttinger liquids" - Phys. Rev. B **82**, 041306(R) (2010)

[100] I. Safi, P. Devillard, and T. Martin -"Partition Noise and Statistics in the Fractional Quantum Hall Effect"- Phys. Rev. Lett. **86**, 4628 (2001)

[101] Jed Dempsey, B. Y. Gelfand, and B. I. Halperin - "Electron-electron interactions and spontaneous spin polarization in quantum Hall edge states" - Phys. Rev. Lett. 70, 3639

[102] V. L. Grigoryan, A. Matos Abiague, and S. M. Badalyan, Phys. Rev. B 80, 165320

[103] C. Neuenhahn and F. Marquardt, "Dephasing by electron-electron interactions in a ballistic Mach-Zehnder interferometer", New Journal of Physics 10, 115018

[104] J. T. Chalker, Yuval Gefen, and M. Y. Veillette - "Decoherence and interactions in an electronic Mach-Zehnder interferometer" - Phys. Rev. B **76**, 085320 (2007)

[105] Ivan P. Levkivskyi and Eugene V. Sukhorukov - "Dephasing in the electronic Mach-Zehnder interferometer at filling factor $\nu = 2$" - Phys. Rev. B **78**, 045322

[106] P. Degiovanni, Ch. Grenier, G. Feve, C. Altimiras, H. le Sueur, and F. Pierre - "Plasmon scattering approach to energy exchange and high-frequency noise in ν=2 quantum Hall edge channels" - Phys. Rev. B **81**, 121302(R)

[107] C. Grenier Ph.D Thesis - "Electronic quantum optics"

[108] D. L. Kovrizhin and J. T. Chalker - "Exactly solved model for an electronic Mach-Zehnder interferometer" - Phys. Rev. B **80**, 161306 (2009)

[109] C. Neuenhahn and F. Marquardt - "Universal dephasing in a chiral 1D interacting fermion system"- Phys. Rev. Lett. **102**, 046806 (2009)

[110] J . H. Han and D. J. Thouless - "Dynamics of compressible edge and bosonization"- Phys. Rev. B **55**, R1926–R1929 (1997)

[111] C. Altimiras, H. le Sueur, U. Gennser, A. Cavanna, D. Mailly, and F. Pierre - "Tuning Energy Relaxation along Quantum Hall Channels" - Phys. Rev. Lett. **105**, 226804 (2010)

[112] G. Feve, A. Mahe, J.-M. Berroir, T. Kontos, B. Plais, D. C. Glattli, A. Cavanna, B. Etienne and Y. Jin - "An On-Demand Coherent Single-Electron Source" - Science 316, 1169

[113] M. Huber, M. Grayson, M. Rother, W. Biberacher, W. Wegscheider, and G. Abstreiter, Phys. Rev. Lett. 94, 016805

[114] F. H. L. Koppens, C. Buizert, K. J. Tielrooij, I. T. Vink, K. C. Nowack, T. Meunier, L. P. Kouwenhoven and L. M. K. Vandersypen, "Driven coherent oscillations of a single electron spin in a quantum dot" - Nature **442**, 766 (2006)

[115] J. M. Elzerman, R. Hanson, L. H. Willems van Beveren, B. Witkamp, L. M. K. Vandersypen & L. P. Kouwenhoven - "Single-shot read-out of an individual electron spin in a quantum dot" - Nature 430, 431 (2004)

[116] R. Hanson, L. H. Willems van Beveren, I. T. Vink, J. M. Elzerman, W. J. M. Naber, F. H. L. Koppens, L. P. Kouwenhoven, and L. M. K. Vandersypen - "Single-Shot Readout of Electron Spin States in a Quantum Dot Using Spin-Dependent Tunnel Rates" - Phys. Rev. Lett. **94**, 196802 (2005)

[117] Sylvain Hermelin, Shintaro Takada, Michihisa Yamamoto, Seigo Tarucha, Andreas D. Wieck, Laurent Saminadayar, Christopher Bäuerle, Tristan Meunier - "Electrons surfing on a sound wave as a platform for quantum optics with flying electrons" - arXiv cond-mat/1107.4759

[118] R. Hanson, B.Witkamp, L.M. K. Vandersypen, L. H.Willems van Beveren, J.M. Elzerman, and L. P. Kouwenhoven, "Zeeman Energy and Spin Relaxation in a One-Electron Quantum Dot", Phys. Rev. Lett **91**, 196802 (2003)

[119] D. Venturelli, V. Giovannetti, F. Taddei, R. Fazio, D. Feinberg, G. Usaj, C. A. Balseiro, Phys. Rev. B 83, 075315

[120] H. Ness, L. K. Dash, and R. W. Godby, "Generalization and applicability of the Landauer formula for nonequilibrium current in the presence of interactions" , Phys. Rev. B **82**, 085426 (2010)

[121] C. Caroli, R. Combescot, P. Nozieres and D. Saint-James, J. Phys. C 5, 21

[122] H.J.W. Haug, A. Jauho, Quantum Kinetics in Transport and Optics of Semiconductors, 2nd Edition, Springer (2008)

[123] Johannes Voit - "Charge-spin separation and the spectral properties of Luttinger liquids" - Phys. Rev. B **47**, 6740 (1993)

[124] M. Fabrizio, A. Parola - "Spin-charge separation in a model of two coupled chains" - Phys. Rev. Lett. **70**, 226–229 (1993)

[125] A. G. Yashenkin, I. V. Gornyi, A. D. Mirlin, and D. G. Polyakov -"Quantum interference and spin-charge separation in a disordered Luttinger liquid"- Phys. Rev. B **78**, 205407

[126] Hugo Aita, Liliana Arrachea, and Carlos Naon - "Four-terminal resistance of an interacting quantum wire with weakly invasive contacts" - Arxiv:cond-mat/1102.1371 (2011)

[127] Biswajit Karmakar, Davide Venturelli, Luca Chirolli, Fabio Taddei, Vittorio Giovannetti, Rosario Fazio, Stefano Roddaro, Giorgio Biasiol, Lucia Sorba, Vittorio Pellegrini, and Fabio Beltram - "Controlled coupling of spin-resolved quantum Hall edge states"- To be published

[128] L. V. Litvin, et al., Phys. Rev. B **75**, 033315 (2007).

[129] P. Roulleau, F. Portier, D. C. Glattli, P. Roche, A. Cavanna, G. Faini, U. Gennser, and D. Mailly, Phys. Rev. B **76**, 161309(R) (2007).

[130] I. Neder et al., Nature Physics **3**, 534 (2007).

[131] I. Neder, et al., Nature **448**, 333 (2007).

[132] E. V. Deviatov, V. T. Dolgopolov and A. Würtz JETP Letters **79**, 504 (2004).

[133] E. V. Deviatov and A. Lorke Phys. Rev. B **77**, 161302(R) (2008).

[134] C. Altimiras, H. le Sueur, U. Gennser, A. Cavanna, D. Mailly, and F. Pierre - "Non-equilibrium edge-channel spectroscopy in the integer quantum Hall regime" - Nature Physics **6**, 34 (2009)

[135] Patrik Recher, Eugene V. Sukhorukov, and Daniel Loss - "Quantum Dot as Spin Filter and Spin Memory" - Phys. Rev. Lett. **85**, 1962 (2000)

[136] N. Paradiso, S. Heun, S. Roddaro, D. Venturelli, F. Taddei, V. Giovannetti, R. Fazio, L. Sorba, G. Biasiol, and F. Beltram, submitted.

[137] I. V. Zozoulenko and M. Evaldsson - "Quantum antidot as a controllable spin injector and spin filter" - Appl. Phys. Lett. **85**, 3136 (2004)

[138] I. A. Larkin and J. H. Davies - "Edge of the two-dimensional electron gas in a gated heterostructure" - Phys. Rev. B **52**, R5525 (1995)

[139] C. L. Kane and Matthew P. A. Fisher - "Shot noise and the transmission of dilute Laughlin quasiparticles" - Phys. Rev. B **67**, 045307 (2003)

[140] A. Komnik et al., "Multiparticle effects in non-equilibrium electron tunneling and field emission", Phys. Rev. B 66 (2002), p. 035407

[141] S. Amasha, K. MacLean, Iuliana P. Radu, D. M. Zumbühl, M. A. Kastner, M. P. Hanson, and A. C. Gossard - "Spin-dependent tunneling of single electrons into an empty quantum dot" - Phys. Rev. B **78**, 041306(R) (2008)

[142] Takashi Kimura, Kazuhiko Kuroki, and Hideo Aoki - "Generation of spin-polarized currents in Zeeman-split Tomonaga-Luttinger models" - Phys. Rev. B **53**, 9572 (1996)

[143] D. V. Averin and Yu. V. Nazarov - "Virtual electron diffusion during quantum tunneling of the electric charge" - Phys. Rev. Lett. **65**, 2446 (1990)

[144] Krzysztof Byczuk - "Spin-charge-separated Luttinger liquid in a magnetic field" - Phys. Rev. B **57**, 3821 (1998)

[145] S. Rabello and Q. Si - "Spectral functions in a magnetic field as a probe of spin-charge separation in a Luttinger liquid" - Europhys. Lett. 60 882 (2002)

[146] Michael T. Woodside, Chris Vale, Paul L. McEuen, C. Kadow, K. D. Maranowski, and A. C. Gossard - "Imaging interedge-state scattering centers in the quantum Hall regime" - Phys. Rev. B **64**, 041310(R) (2001)

[147] Zozoulenko, I. V. Evaldsson, M. - "Quantum antidot as a controllable spin injector and spin filter" - Appl. Phys. Lett **85** 3136 (2004)

[148] Michael A. Nielsen, Isaac L. Chuang - "Quantum Computation and Quantum Information" - Cambridge University Press (2004)

[149] Chuang, I. and Yamamoto, Y. Simple quantum computer. *Phys. Rev. A* **52**, 3489 (1995).

[150] E. Knill, R. Laflamme & G. J. Milburn - "A scheme for efficient quantum computation with linear optics" - Nature 409, **46** (2001)

[151] C. de C. Chamon and X. G. Wen - "Sharp and smooth boundaries of quantum Hall liquids"- Phys. Rev. B **49**, 8227 (1994)

[152] Sourin Das and Sumathi Rao - "Spin-Polarized Scanning-Tunneling Probe for Helical Luttinger Liquids" - Phys. Rev. Lett. **106**, 236403 (2011)

[153] S. Becker, C. Karrasch, T. Mashoff, M. Pratzer, M. Liebmann, V. Meden, and M. Morgenstern - "Probing Electron-Electron Interaction in Quantum Hall Systems with Scanning Tunneling Spectroscopy" - Phys. Rev. Lett. **106**, 156805 (2011)

[154] C. Neuenhahn and F. Marquardt - "Dephasing by electron-electron interactions in a ballistic Mach-Zehnder interferometer"- New Journal of Physics **10**, 115018 (2008)

[155] Charles Grenier, Rémy Hervé, Gwendal Fève, Pascal Degiovanni - "Electron quantum optics in quantum Hall edge channels" - arXiv:1102.0466

[156] Veronica Cerletti, W. A. Coish, Oliver Gywat and Daniel Loss - "Recipes for spin-based quantum computing" - Nanotechnology **16**, R27 (2005)

[157] Fabrizio Dolcini - "Full electrical control of charge and spin conductance through interferometry of edge states in topological insulators" - Phys. Rev. B **83**, 165304 (2011)

[158] Stefano Pugnetti, Fabrizio Dolcini, Dario Bercioux, and Hermann Grabert - "Electron tunneling into a quantum wire in the Fabry-Pérot regime" - Phys. Rev. B **79**, 035121 (2009)